

Measurement of the relative fraction of $t\bar{t}$ events produced
via gluon-fusion in $p\bar{p}$ collision at $\sqrt{s} = 1.96$ TeV at CDF

by Jared Yamaoka

A dissertation submitted to the
Graduate School—New Brunswick
Rutgers, The State University of New Jersey
in partial fulfillment of the requirements
for the degree of
Doctor of Philosophy
Graduate Program in Physics and Astronomy

Written under the direction of
Professor Sunil Somalwar
and approved by

New Brunswick, New Jersey

October, 2007

ABSTRACT OF THE DISSERTATION

Measurement of the relative fraction of $t\bar{t}$ events produced via gluon-fusion in $p\bar{p}$ collision at $\sqrt{s} = 1.96$ TeV at CDF

by Jared Yamaoka

Dissertation Director: Professor Sunil Somalwar

In this thesis we present a measurement of the relative fraction of $t\bar{t}$ events produced via gluon-fusion to the total number of $t\bar{t}$ events. Using the kinematics of the production and decay of the top and antitop quark pair, we trained a Neural Network to discriminate the gluon-fusion events. The Neural Network was then used as a template to fit for the gluon-fusion fraction in data. Using a total integrated luminosity of 955 pb^{-1} we find $\frac{\sigma(gg \rightarrow t\bar{t})}{\sigma(p\bar{p} \rightarrow t\bar{t})} < 0.33$ at 68% confidence level and $\frac{\sigma(gg \rightarrow t\bar{t})}{\sigma(p\bar{p} \rightarrow t\bar{t})} < 0.61$ at 95% confidence level.

Acknowledgements

I would like to thank my advisor, Sunil Somalwar. His knowledge of the field of particle physics has guided me through all different aspects of surviving at a large experiment like CDF. I would also like to thank Eva Halkiadakis and Ricardo Eusebi, without whom this analysis would have never been completed.

I would like to thank the entire Rutgers CDF group: Tom Devlin, Terry Watts, Amit Lath, Anton Anastassov, Dongwook Jang, Daryl Hare, and Sourabh Dube, who provided great friendship and support.

Others that should be mentioned. Steve Worm, thanks for getting me started at CDF. Tom Wright, thanks for the occasional distraction that everyone needs during the day, and making sure my bibliography looks great. Paul DiTuro and John Zhou, thank you for your friendship, I wish you the best wherever you are now.

Dedication

For my family, blood relation or not.

Table of Contents

Abstract	ii
Acknowledgements	iii
Dedication	iv
List of Tables	vii
List of Figures	viii
1. The Top Quark and the Standard Model	1
1.1. Collider Experiment Primer	1
1.2. Standard Model	2
1.3. Top Properties	5
1.4. Top Production	9
1.4.1. Parton Distribution Functions	10
1.5. Analysis Method	12
2. Experimental Apparatus	15
2.1. Tevatron	15
2.1.1. Proton Source	15
2.1.2. Main Injector	17
2.1.3. Antiproton Source	17
2.1.4. High Energy Collisions	18
2.2. Collider Detector at Fermilab (CDF II)	19
2.2.1. Detector Coordinates	19
2.2.2. Charged Particle Tracking	21
Silicon Detector	22

Central Outer Tracker	24
2.2.3. Energy Measurement	26
2.2.4. Muon Detector	29
2.2.5. Trigger and Data Acquisition	32
3. Event Selection	35
3.1. Trigger	35
3.2. Particle Identification	35
3.2.1. Lepton Identification	36
3.2.2. Hadronic Jets	36
3.2.3. b -jet Identification using Secondary Vertexing	36
3.2.4. Neutrino Identification: \cancel{E}_T	37
3.3. Selected Events	39
3.4. Backgrounds Estimation	39
3.4.1. $W + 4jets$	39
3.4.2. Other Backgrounds	40
4. Analysis Method	41
4.1. Measurement Strategy	41
4.2. Simulated Events	42
4.3. Event Reconstruction	43
4.3.1. Kinematic Fitter	43
4.3.2. Kinematic Variables	43
4.4. Building the templates	46
4.4.1. Neural Network description	46
4.4.2. Templates	46
4.4.3. Likelihood	46
5. The Feldman-Cousins Method	57
5.1. The Method	57

5.2. Pseudo-experiments	58
5.2.1. Acceptance	58
5.2.2. Generating the Pseudo-experiments	60
6. Systematic Uncertainties	62
6.1. Jet Energy Scale	63
6.1.1. Background Shape and Composition	65
6.1.2. Gluon Radiation	69
Initial State Radiation	69
Final State Radiation	71
6.1.3. Parton Distribution Functions	75
6.1.4. Next to Leading Order Corrections	75
6.1.5. Summary of Systematic Uncertainties	77
7. Results	78
7.1. Results	78
7.2. Conclusions	78
Appendix A. Overview of Neural Networks	81
Appendix B. Top Mass Dependence	84
Appendix C. Neural Network Variables in Data	86
References	96
Curriculum Vita	101

List of Tables

1.1. Quark and leptons in the Standard Model	4
1.2. Bosons in the Standard Model	4
1.3. Branching ratios (BR) for $t\bar{t}$ events	8
2.1. Tevatron Run II performance.	19
2.2. The specifications for the calorimeters at CDF.	30
3.1. Number of events observed in data (N_{data}) and b-tag fraction for events with one and two or more tagged jets.	39
3.2. Estimated signal fraction (\bar{C}_s), b-tag fraction and number of events ob- served in data (N_{data}) and estimated background (N_{bkg}) for events with one and two or more b-tags.	40
4.1. Summary of Monte Carlo data sets used to model signal and background.	43
5.1. Acceptance for $t\bar{t}^{gg}$ and $t\bar{t}^{qq}$ events for the 1 and 2-tag samples.	60
5.2. Nominal number of events to be used for the throwing of pseudo-experiments.	61
6.1. Example of the background systematic due to sample composition and Q^2 energy scale	68
6.2. Overview of Systematics	77

List of Figures

1.1. Next to Leading Order corrections to the W mass	5
1.2. Higgs bound from indirect searches	6
1.3. Higgs exclusion from direct searches	7
1.4. <i>Lepton + Jets</i> decay channel: Defined as one W decaying <i>leptonically</i> ($W \rightarrow l + \nu$) and the other W decaying <i>hadronically</i> ($W \rightarrow u + d$). . .	7
1.5. <i>Single</i> top production: While theoretically possible, the production of a single top is a factor of ~ 0.4 [1] smaller than pair produced tops. . . .	9
1.6. Top pair production: Leading order diagrams for $t\bar{t}$ production.	10
1.7. Lepton proton interaction: Experiments like ZEUS at the DESY labo- ratory in Germany probe the structure of the proton using the HERA electron-proton collider. The data from ZEUS and others is used to pro- vide the Parton Distribution Functions (PDF) which are important to hadron colliders like the Tevatron	11
1.8. Parton distribution functions for $Q = 2$ GeV and $Q = 100$ GeV [2]. The different lines represent the constituents of the proton. For any value of x , you can determine relative fraction of each type of parton. Example: For $Q = 2$ GeV you are four times more likely to find a gluon with $x = 0.1$ than a u quark.	12

1.9. Parton luminosities for the Tevatron (Run I) and LHC [3]. The lines show the differential lumiosity as a function of the parton interaction energy $\sqrt{\hat{s}}$. The top set of lines labeled 14 TeV is for the LHC, and the lower set labeled 1.8 TeV is for the Tevatron. The vertical dotted lines are just to guide the eye. The left one is at 350 GeV, the threshold for $t\bar{t}$ production. This plot was calculated for the Tevatron Run I energy of 1.8 TeV, however at 1.96 TeV the curves are expected to be similar. Also this plot is shown just as an illustration.	13
2.1. Schematic of the Fermilab accelerator chain.	16
2.2. An elevation view of half of the CDF II detector.	20
2.3. Open cutaway of the CDF II detector.	20
2.4. One quadrant of the CDF II tracking volume projected in the y-z plane.	22
2.5. Silicon Endview (As if looking down the beam pipe): The silicon detector chips are arranged cylindrically supported by a composite strut system.	23
2.6. Cartoon rendering of a single sided silicon strip detector.	24
2.7. Intermediate Silicon Layer (ISL): The outer most silicon layer designed to extend the silicon tracking in η beyond the edge of the wire drift chamber (COT).	25
2.8. COT Superlayers: 1/6 of the east plate. Notice the cells are tilted with respect to the radial direction. This is to account for the charge drift due to the presence of a strong magnetic field. The cells are arranged into 8 <i>superlayers</i>	27
2.9. Schematic of the COT cells. The arrow show the radial direction. Notice that the cells are tilted 35° with respect to the radial direction.	28
2.10. Muon coverage in η and ϕ	31
2.11. Schematic of the CDF data acquisition system.	33

3.1. Illustration of a displaced vertex: L_{xy} is the distance from the primary vertex to the secondary vertex along the projection of the candidate jet onto the $x-y$ plane. The value L_{xy} is the variable of merit when assigning a secondary vertex tag, what we call a b-tag.	38
4.1. Off-diagonal Spin Basis	44
4.2. Differential cross section for $t\bar{t}$ production	45
4.3. Distribution of $\cos\theta^*$ for $t\bar{t}^{gg}$ (blue, solid) and $t\bar{t}^{qq}$ (red, dashed) and background (black, dotted) for 1-tag (top) and ≥ 2 -tags events (bottom).	47
4.4. Distribution of β for $t\bar{t}^{gg}$ (blue, solid) and $t\bar{t}^{qq}$ (red, dashed) and background (black, dotted) for 1-tag (top) and ≥ 2 -tags events (bottom).	48
4.5. Distribution of $\cos\theta_{Wlep}$ for $t\bar{t}^{gg}$ (blue, solid) and $t\bar{t}^{qq}$ (red, dashed) and background (black, dotted) for 1-tag (top) and ≥ 2 -tags events (bottom).	49
4.6. Distribution of $\cos\theta_{lep}$ for $t\bar{t}^{gg}$ (blue, solid) and $t\bar{t}^{qq}$ (red, dashed) and background (black, dotted) for 1-tag (top) and ≥ 2 -tags events (bottom).	50
4.7. Distribution of $\cos\theta_\nu$ for $t\bar{t}^{gg}$ (blue, solid) and $t\bar{t}^{qq}$ (red, dashed) and background (black, dotted) for 1-tag (top) and ≥ 2 -tags events (bottom).	51
4.8. Distribution of $\cos\theta_{W had}$ for $t\bar{t}^{gg}$ (blue, solid) and $t\bar{t}^{qq}$ (red, dashed) and background (black, dotted) for 1-tag (top) and ≥ 2 -tags events (bottom).	52
4.9. Distribution of $\cos\theta_{up}$ for $t\bar{t}^{gg}$ (blue, solid) and $t\bar{t}^{qq}$ (red, dashed) and background (black, dotted) for 1-tag (top) and ≥ 2 -tags events (bottom).	53
4.10. Distribution of $\cos\theta_{down}$ for $t\bar{t}^{gg}$ (blue, solid) and $t\bar{t}^{qq}$ (red, dashed) and background (black, dotted) for 1-tag (top) and ≥ 2 -tags events (bottom).	54
4.11. Neural Network distributions that we use as templates for 1-tag (top) and 2-tag (bottom) events for $t\bar{t}^{qq}$ (red), $t\bar{t}^{gg}$ (blue) and background (black).	55
5.1. Sample Feldman-Cousins confidence band at 68% confidence level.	59
5.2. Example set of pseudo-experiments.	61
6.1. Comparison of pseudo-experiments used to derive systematic errors.	63
6.2. Jet energy correction and uncertainty.	64
6.3. Neural Network shapes for Jet Energy Scale systematic	66

6.4. Feldman-Cousins 68% C.L. with JES systematic. The blue band shows the statistical uncertainty, with the red band showing the statistical plus systematic uncertainty. The top plot shows $+1\sigma$ JES correction, while the bottom plot shows the -1σ JES correction	67
6.5. Example pseudo-experiments used to calculate the background systematic due to sample composition and Q^2 energy scale	68
6.6. Feldman-Cousins 68% C.L. with the background shape and composition systematic uncertainty.	69
6.7. Lepton + Jets with Initial and Final State Radiation	70
6.8. Z Dilepton with Initial State Radiation	70
6.9. Neural Network shapes for the Initial State Radiation (ISR) systematic	71
6.10. Feldman-Cousins 68% C.L. with ISR systematic. The blue band shows the statistical uncertainty, with the red band showing the statistical plus systematic uncertainty. The top plot shows FC made with $t\bar{t}$ event with more ISR, while the bottom plot shows FC made with $t\bar{t}$ event with less ISR.	72
6.11. Neural Network shapes for the Final State Radiation (FSR) systematic .	73
6.12. Feldman-Cousins 68% C.L. with FSR systematic. The blue band shows the statistical uncertainty, with the red band showing the statistical plus systematic uncertainty. The top plot shows FC made with $t\bar{t}$ event with more FSR, while the bottom plot shows FC made with $t\bar{t}$ event with less FSR.	74
6.13. Neural Network shapes for the Parton Distribution Function (PDF) systematic	76
6.14. Feldman-Cousins 68% C.L. with next to leading order (NLO) systematic	76
6.15. Feldman-Cousin plot at 68% C.L.	77
7.1. Negative Log Likelihood for the Data	79
7.2. FC with all systematic errors compared to FC with only statistical error for a confidence level of 68%.	79

7.3.	Final systematic error from all sources using the Feldman-Cousins method.	79
7.4.	Neural network templates fit to the Data (Left 1 tag, Right 2 tag). . . .	80
A.1.	Generic diagram of a typical feed-forward neural network. Input on the left and output on the right.	82
B.1.	FC for $m_t = 170$ GeV with statistical error only.	85
B.2.	FC for $m_t = 180$ GeV with statistical error only.	85
C.1.	Neural network templates fit to the Data (top 1 tag, bottom 2 tag). . .	87
C.2.	β fractions set to the neural network fit to the Data (top 1 tag, bottom 2 tag).	88
C.3.	$\cos\theta^*$ fractions set to the neural network fit to the Data (top 1 tag, bottom 2 tag).	89
C.4.	$\cos\theta_{Wlep}$ fractions set to the neural network fit to the Data (top 1 tag, bottom 2 tag).	90
C.5.	$\cos\theta_{lep}$ fractions set to the neural network fit to the Data (top 1 tag, bottom 2 tag).	91
C.6.	$\cos\theta_\nu$ fractions set to the neural network fit to the Data (top 1 tag, bottom 2 tag).	92
C.7.	$\cos\theta_{Whad}$ fractions set to the neural network fit to the Data (top 1 tag, bottom 2 tag).	93
C.8.	$\cos\theta_{up}$ fractions set to the neural network fit to the Data (top 1 tag, bottom 2 tag).	94
C.9.	$\cos\theta_{down}$ fractions set to the neural network fit to the Data (top 1 tag, bottom 2 tag).	95

Chapter 1

The Top Quark and the Standard Model

The last two decades of the twentieth century have witnessed many new discoveries in the field of high energy physics. In the 1980's CERN discovered the W and Z [4, 5], while later in the 1990's the top quark was observed at Fermilab [6, 7]. Aside from the Higgs, these particles complete what is expected from the Standard Model.

With the particles of the Standard Model in place, we can begin to explore their properties. With a mass of about 180 times the mass of the proton, the top quark is the most massive of all the discovered fundamental particles. Because of its mass, the top is particularly interesting. In Section 1.3, we discuss some of implications the top mass has on the Higgs mass, and other phenomenology exclusive to the top because of its large mass.

In this thesis we are measuring the relative rate of the different processes that produce top quarks, specifically top and antitop ($t\bar{t}$) pairs. In general, the total production rate of a given physical process is measured by counting the number of events. However, the contribution from different production processes to the total rate is very hard to measure. We use some of the unique properties of the top quark to differentiate the two main processes that produce $t\bar{t}$.

1.1 Collider Experiment Primer

Particle physics, like most topics in science, has several layers of jargon. In this section it is necessary to cover some of the basic terminology and scientific concepts to avoid confusion later on.

The total production rate, or *cross section* (σ), of a given physical process can be measured by simply counting the number of produced events, N .

$$N = \sigma \int \mathcal{L} dt \quad (1.1)$$

Here \mathcal{L} stands for *luminosity*, which describes the rate of interactions produced at our experiment, thus the integrated luminosity is the total number of interactions over an amount of time. Often the events we are looking for have many ways of decaying. For example W bosons can decay to leptons or it can decay to quarks. The rate of each type of decay, or *channel*, is its *branching ratio* (BR). Of course the final complication is that there is always some detection (in)efficiency, what we refer to as *acceptance* (A), that reduces the number of observed events. Finally, for any given channel, the number of events is given by:

$$N = \sigma \cdot A \cdot BR \int \mathcal{L} dt \quad (1.2)$$

The unit of measure for σ is *barns* (b) equal to 10^{-28} m^2 , most process of interest at the Tevatron energy have a cross section of $\sim 10 \text{ pb}$.¹ It is convenient to then measure luminosity in terms of $\text{b}^{-1}\text{s}^{-1}$ or $\text{pb}^{-1}\text{s}^{-1}$, with the integrated luminosity simply b^{-1} or pb^{-1} .

1.2 Standard Model

The Standard Model of particle physics is a field theory developed in the early 1970's. Consistent with both quantum mechanics and special relativity, its goal is to unify three of the fundamental forces found in nature: the strong nuclear force, the weak nuclear force, and the electromagnetic force. (The gravitational force is not incorporated into the Standard Model.) The Standard Model is represented by the gauge group G :

$$G = SU(3)_C \times SU(2)_L \times U(1)_Y \quad (1.3)$$

where the model is a combination of two previous theories:

¹Here pb means picobarns (10^{-12} b).

- The theory of quantum chromodynamics (QCD) [8, 9] describes the strong nuclear force and is represented by the $SU(3)_C$ gauge group. Here C stands for *color*, where color can have one of the three values *red*, *green*, and *blue*. Antiquarks carry anticolor and all hadrons are required to be color singlets.
- The Glashow-Salam-Weinberg (GSW) theory of electroweak interaction [10, 11, 12] is a unification of the electromagnetic force and the weak nuclear force represented by a $SU(2)_L \times U(1)_Y$ gauge group. Here L stands for left-handed, because when mediated by the W , parity is violated thus there are only left-hand neutrinos. In $U(1)_Y$, the Y is hypercharge, with $Y = Q - I_3$, where Q is the electric charge and I_3 is the third component of weak isospin.

The Standard Model requires a hierarchy of fundamental particles, many of which were predicted by the theory before they were eventually found experimentally. The Standard Model predicts, and experiments have found, three generations of particles with spin $\frac{1}{2}$, called fermions. Each generation has two leptons that interact via the electroweak force, and two quarks that interact via the electroweak force and the strong nuclear force. Each fermion has a corresponding antiparticle that differs only by having the opposite electrical charge. Another class of particles required by the Standard Model are *bosons*, which have spin 1 and mediate the forces. The electromagnetic force is mediated by the photon (γ), the weak nuclear force is mediated by the W^\pm and Z^0 , and the strong nuclear force is mediated by the gluon (g). See Tables 1.1 and 1.2.

The Standard Model, as described so far, has been very successful at describing what we actually see in experiments. There are outstanding issues with the Standard Model. In order to preserve the symmetry of the gauge group, the fermions and the W^\pm and Z^0 have to be massless, but we know this is not true. The particles are bestowed with their mass through a process known as Electroweak Symmetry Breaking (EWSB). EWSB is accomplished by introducing a scalar field, known as the Higgs Field [13, 14]. In effect, the interaction of the fermions and bosons with this field is how they acquire their mass. The Higgs Field has an associated massive Higgs boson, that is the last piece of the Standard Model.

Generation	First		Second		Third	
Quarks (spin = 1/2)						
Name	up	down	charm	strange	top	bottom
Charge	+2/3	-1/3	+2/3	-1/3	+2/3	-1/3
Mass (MeV/c ²) <i>approx</i>	4	8	1350	130	171000	4400
Interaction	EM, Weak, Strong					
Leptons (spin = 1/2)						
Name	ν_e	e^-	ν_μ	μ^-	ν_τ	τ^-
Charge	0	-1	0	-1	0	-1
Mass (MeV/c ²) <i>approx</i>	$< 3 \times 10^{-6}$	0.5	< 0.2	100	< 18	1780
Interaction	Weak	EM, Weak	Weak	EM, Weak	Weak	EM, Weak

Table 1.1: Quark and leptons in the Standard Model. Each particle has an antiparticle, which has equal mass and identical physical properties but opposite charge. *In the units above, the charge of the proton is 1.*

Boson	Charge	Mass (GeV/c ²)	Force
γ	0	0	EM
W^\pm	± 1	80.4	Weak
Z	0	90.2	Weak
g	0	0	Strong

Table 1.2: Bosons in the Standard Model: These particles, with spin 1, mediate the forces in the Standard Model. *In the units above, the charge of the proton is 1.*

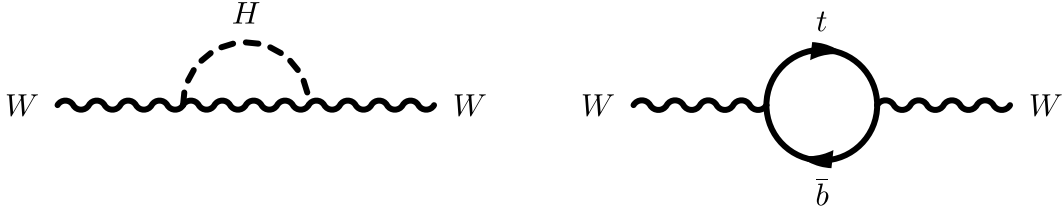


Figure 1.1: Next to Leading Order (NLO) corrections to the W mass. Left: A Higgs boson loop which contributes a correction. Right: A fermion loop involving top and bottom quarks. The large top quark mass dominates this correction. By knowing the W mass and the top mass, some constraints can be put on the Higgs boson mass.

The Higgs boson has yet to be found experimentally, and thus remains one of the most important questions in Physics. The mass of the Higgs boson is not predicted in the Standard Model, but indirect bounds on its value can be derived from next to leading order (NLO) effects, like those shown in Figure 1.1. Using CERN's Large Electron Positron (LEP) collider data, Stanford Linear Collider Large Detector (SLD) data, and Tevatron data, the precision measurements of the W mass ($m_W = 80413 \pm 48 \text{ MeV}/c^2$ [15]) and top mass ($m_{top} = 170.9 \pm 1.8 \text{ GeV}/c^2$ [16]) provide a bound on the Higgs mass, Figure 1.2. Currently the best direct Higgs search is from LEP and has set a lower bound on the Higgs mass of $m_H > 114.4 \text{ GeV}/c^2$ at the 95% confidence level [17], Figure 1.3.

1.3 Top Properties

In the Standard Model, the top quark decays through the weak interaction and is expected to decay almost entirely to a W boson and a b quark. Decays to $W + s$ and $W + d$ are allowed in the Standard Model, but these are heavily suppressed because of quark flavor mixing [19]. For this analysis we assume top quarks decay 100% to $W + b$.

The final state particles are determined by the decays of the W bosons produced by the top pair. The W can decay into a lepton and a neutrino (what we call a *leptonic decay*) or into an up-type and down-type quark (what we call a *hadronic decay*). The case with both W 's decaying to quarks is the most probable. This decay channel is problematic experimentally because at the Tevatron we have a large multi-jet

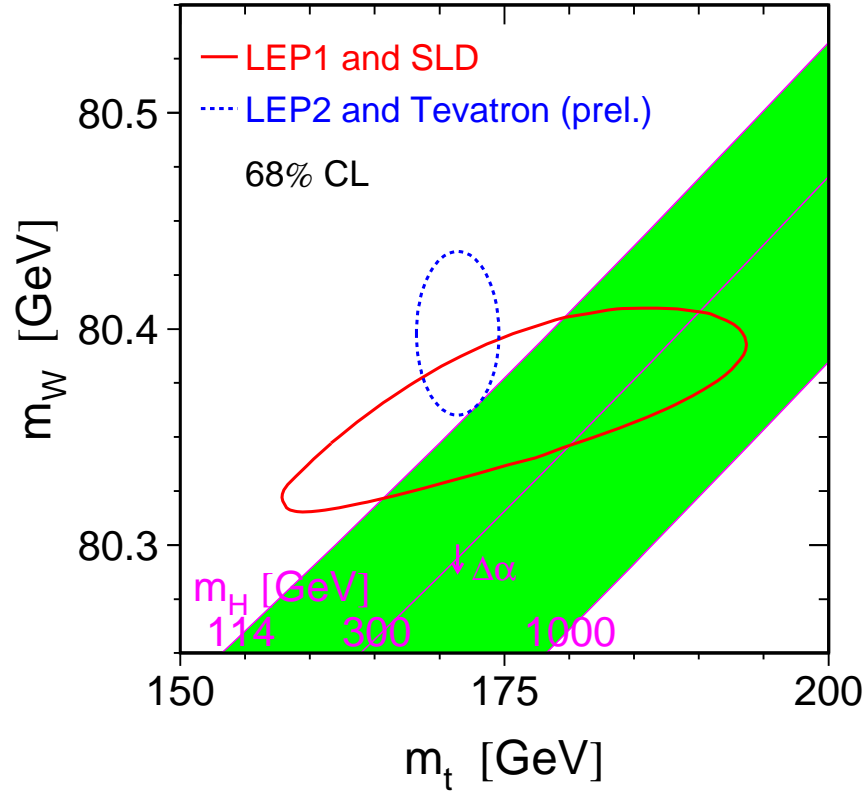


Figure 1.2: Higgs bound from indirect searches: The green band is the allowed parameter region in the $m_t - m_W$ plane for a SM Higgs mass 114 – 1000 GeV/c². The red ellipse is the region constrained by the LEP and SLD using indirect measurements of m_W and m_t . The green region contained within the red ellipse are the allowed values of the Higgs mass. Similarly the blue ellipse is the constraint using LEP2 results and direct measurements of m_W and m_t from the Tevatron Run II results as of March 2007.

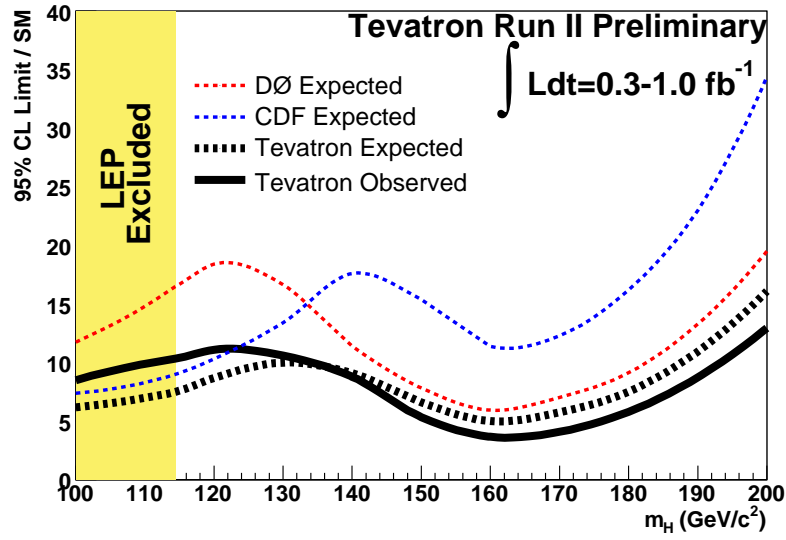


Figure 1.3: Higgs exclusion from direct searches: The figure shows the excluded region as a function of Higgs mass, with the vertical axis showing the excluded cross section at 95% C.L. relative to the Standard Model prediction. The best result come from LEP [17], with a m_H up to 114.4 GeV/ c^2 excluded at 95% confidence level. The Tevatron (CDF/DØ) results [18] are weaker limits, but extend to a higher mass range. Expected limits are derived from simulation assuming no Higgs. Fluctuations in the data can cause a discrepancy between the observed and expected limit.

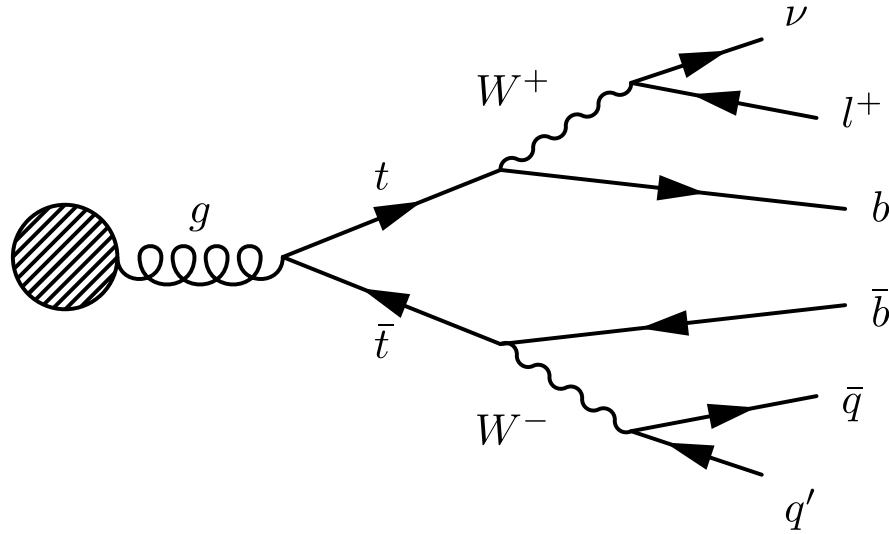


Figure 1.4: *Lepton + Jets* decay channel: Defined as one W decaying *leptonically* ($W \rightarrow l + \nu$) and the other W decaying *hadronically* ($W \rightarrow u + d$).

Decay Mode	BR	Channel
$t\bar{t} \rightarrow (q\bar{q}'b)(qq'\bar{b})$	36/81	Full-Hadronic
$t\bar{t} \rightarrow (q\bar{q}'b)(e\nu\bar{b})$	12/81	Lepton + Jets
$t\bar{t} \rightarrow (q\bar{q}'b)(\mu\nu\bar{b})$	12/81	Lepton + Jets
$t\bar{t} \rightarrow (q\bar{q}'b)(\tau\nu\bar{b})$	12/81	Lepton + Jets (τ)
$t\bar{t} \rightarrow (e\nu b)(\mu\nu\bar{b})$	2/81	Dilepton
$t\bar{t} \rightarrow (e\nu b)(\tau\nu\bar{b})$	2/81	Dilepton (τ)
$t\bar{t} \rightarrow (\mu\nu b)(\tau\nu\bar{b})$	2/81	Dilepton (τ)
$t\bar{t} \rightarrow (e\nu b)(e\nu\bar{b})$	1/81	Dilepton
$t\bar{t} \rightarrow (\mu\nu b)(\mu\nu\bar{b})$	1/81	Dilepton
$t\bar{t} \rightarrow (\tau\nu b)(\tau\nu\bar{b})$	1/81	Dilepton (τ)

Table 1.3: Branching ratios (BR) for $t\bar{t}$ events. We use Lepton + Jets channel because it offers a high signal to background. However we don't include events with τ 's because they are very difficult to reconstruct.

background from QCD that is difficult to differentiate from the $t\bar{t}$ events. The case with both W 's decaying to leptons is also difficult because the neutrinos do not leave a signature in the detector, and with two unknowns from the neutrinos we can not fully reconstruct the kinematics of the event. In this analysis, we use events with one W decaying leptonically and one W decaying hadronically. We call this the *lepton + jets* channel, Figure 1.4. In the detector τ signatures are difficult to reconstruct, so we only use events with e or μ . These represent $\sim 30\%$ of all $t\bar{t}$ events. A full breakdown of all the decay channels can be found in Table 1.3.

The top quark is the most massive particle in the Standard Model we have discovered, and is likely to be heavier than the Higgs. At roughly 40 times the mass of the b quark, the top has a unique feature that we exploit in this analysis. The decay rate of the top quark is given by Equation 1.4 [20].

$$\Gamma(t \rightarrow Wb) = \frac{G_f m_t^3}{8\sqrt{2}\pi} |V_{tb}|^2 \sim 175 \text{ MeV} \left(\frac{m_t}{m_W} \right)^3 \quad (1.4)$$

The top quark, with a mass of about 175 GeV, has an expected lifetime (Equation 1.5) of approx 10^{-24} seconds, which is an order of magnitude smaller than the typical life of a resonance.

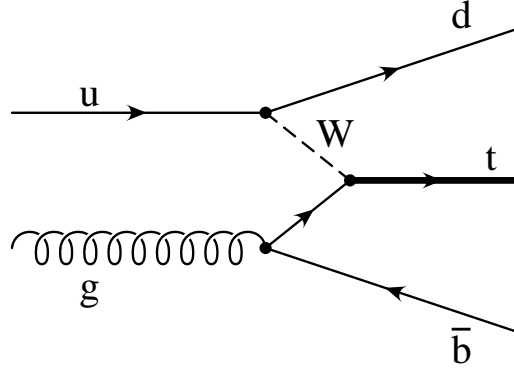


Figure 1.5: *Single* top production: While theoretically possible, the production of a single top is a factor of ~ 0.4 [1] smaller than pair produced tops.

$$\tau_t = \frac{1}{\Gamma_t} \sim 10^{-24} s \quad (1.5)$$

As a consequence, the spin information carried by the top quark is preserved in the decay products, allowing the different production processes to retain their kinematic characteristics in the final state.

1.4 Top Production

At hadron colliders like the Tevatron, top quarks are almost exclusively produced in pairs via the strong interaction. The process of producing one top quark, often referred to as *single* top, Figure 1.5, is allowed in the Standard Model through the electroweak interaction. However, the rate for *single* top is approximately an order of magnitude smaller, and has not been observed. The production mechanism for $t\bar{t}$ is either gluon-fusion or quark-annihilation, Figure 1.6. The total leading order cross sections for $gg \rightarrow t\bar{t}$ and $q\bar{q} \rightarrow t\bar{t}$ are well known [21, 22]. The dominant terms are:

$$\sigma_{gg}(\hat{s}) = \frac{4\pi\alpha_s^2}{12\hat{s}} \left[\left(1 + \rho + \frac{\rho^2}{16}\right) \ln \frac{1+\beta}{1-\beta} - \beta \left(\frac{7}{4} + \frac{31}{16}\rho\right) \right] \quad (1.6)$$

$$\sigma_{q\bar{q}}(\hat{s}) = \frac{8\pi\alpha_s^2}{27\hat{s}} \beta \left[1 + \frac{\rho}{2} \right] \quad (1.7)$$

where

$$\rho = \frac{4m_t}{\hat{s}} \quad (1.8)$$

$$\beta = \sqrt{1 - \rho} \quad (1.9)$$

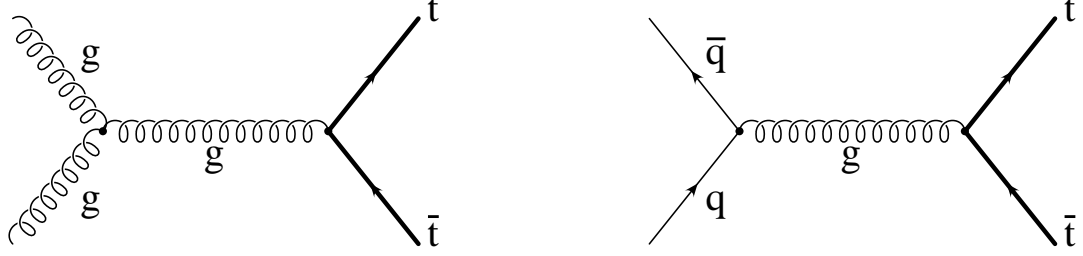


Figure 1.6: Top pair production: Leading order diagrams for $t\bar{t}$ production. Left: $t\bar{t}$ produced from gluon-fusion, which account for $\sim 15\%$ of all $t\bar{t}$ events. Right: $t\bar{t}$ produced from $q\bar{q}$ -annihilation, which account for $\sim 85\%$ of all $t\bar{t}$ events.

Thus, β is the velocity of the top quarks in the center of mass frame with invariant energy $\sqrt{\hat{s}}$.

At the threshold for $t\bar{t}$ production Equation 1.6 and Equation 1.7 are reduced to:

$$\sigma_{gg}(\hat{s}) \approx \frac{7}{48} \frac{\pi \alpha_s^2}{\hat{s}} \beta \quad (1.10)$$

$$\sigma_{q\bar{q}}(\hat{s}) \approx \frac{4}{9} \frac{\pi \alpha_s^2}{\hat{s}} \beta \quad (1.11)$$

Here, we have approximately a factor of three difference between the leading order gluon-fusion cross section and the $q\bar{q}$ annihilation cross section.

1.4.1 Parton Distribution Functions

The Tevatron is a hadron collider so the partonic structure of the proton/antiproton also has a role in the observed production fraction. Perturbative QCD (pQCD) is used to model the structure of the proton. pQCD evolved from the Quark Parton Model. Consider the interaction shown in Figure 1.7. This model treats the quarks in the nucleon as point-like particles. We define Q^2 (Equation 1.13) as the energy scale of the interaction and x (Equation 1.13) as the fraction of momentum of each parton in the nucleon.

$$Q^2 = -q^2 = (k - k') \quad (1.12)$$

$$x = \frac{Q^2}{2(p \cdot q)} \quad (1.13)$$

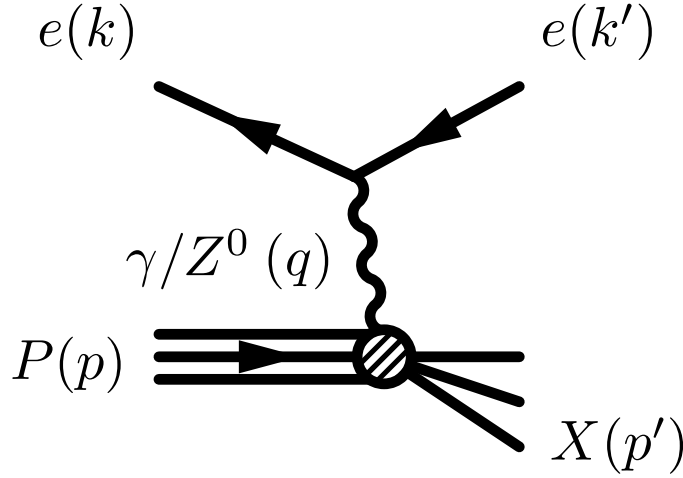


Figure 1.7: Lepton proton interaction: Experiments like ZEUS at the DESY laboratory in Germany probe the structure of the proton using the HERA electron-proton collider. The data from ZEUS and others is used to provide the Parton Distribution Functions (PDF) which are important to hadron colliders like the Tevatron

If the nucleon is composed of point-like particles, then the model should be independent of the energy scale [23]. Because of this invariance, a parton distribution function (PDF), $f_i(x)$, can be constructed, one for each parton in the nucleon. Here $f_i(x)dx$ represents the probability of finding parton i with a momentum fraction between x and $x + dx$. The sum over all partons and over all values of x should equal one (Equation 1.14).

$$\int_0^1 dx \, x \sum_i f_i(x) = 1 \quad (1.14)$$

It was shown experimentally that this value is only 0.5 [24], so the quarks carry only half of the total momentum of the nucleon! Clearly there are other particles within the nucleon, what we now know as gluons. This development led to QCD replacing the Quark Parton Model.

A quark inside the nucleon can radiate gluons and the gluons can in turn radiate more gluons or quarks. The PDF's are no longer invariant to the energy scale (Q^2) because at higher values of Q^2 one begins to probe the gluon radiation rather than the quarks. An example of the parton distribution functions for the proton can be seen in Figure 1.8. Notice the dependence on Q , and that gluons dominate at higher values of Q .

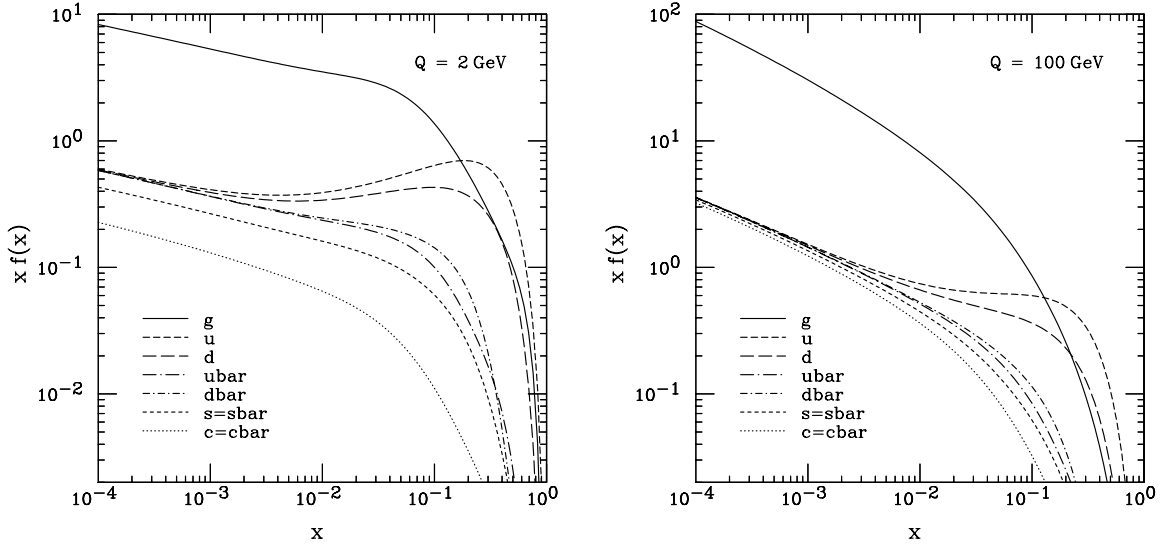


Figure 1.8: Parton distribution functions for $Q = 2 \text{ GeV}$ and $Q = 100 \text{ GeV}$ [2]. The different lines represent the constituents of the proton. For any value of x , you can determine relative fraction of each type of parton. Example: For $Q = 2 \text{ GeV}$ you are four times more likely to find a gluon with $x = 0.1$ than a u quark.

At the Tevatron energy, the relative $gg:q\bar{q}$ luminosities are $\sim 3 : 5$ at the $t\bar{t}$ threshold. Figure 1.9 shows the parton luminosities for the Tevatron and the LHC. At the leading order, the gluon-fusion process accounts for about 20% of all $t\bar{t}$ events. A rigorous theoretical calculation [25, 26] constrains the gluon-fusion fraction to 10%-20% at the Tevatron. It is interesting to note that at the LHC the gluon-fusion fraction becomes $\sim 90\%$.

1.5 Analysis Method

The strategy of the measurement is based on the different kinematic properties of gluon-fusion events and $q\bar{q}$ -annihilation events. One of characteristic we use is the spin of the $t\bar{t}$ system strongly depends on the production process. Because the top quark decays before losing its spin information, we can use this to differentiate the two processes. We also use other production kinematics. The variables we use will be explained in greater detail in Section 4.3. Using simulations of the different production methods we fit for the fraction of gluon-fusion events in our data.

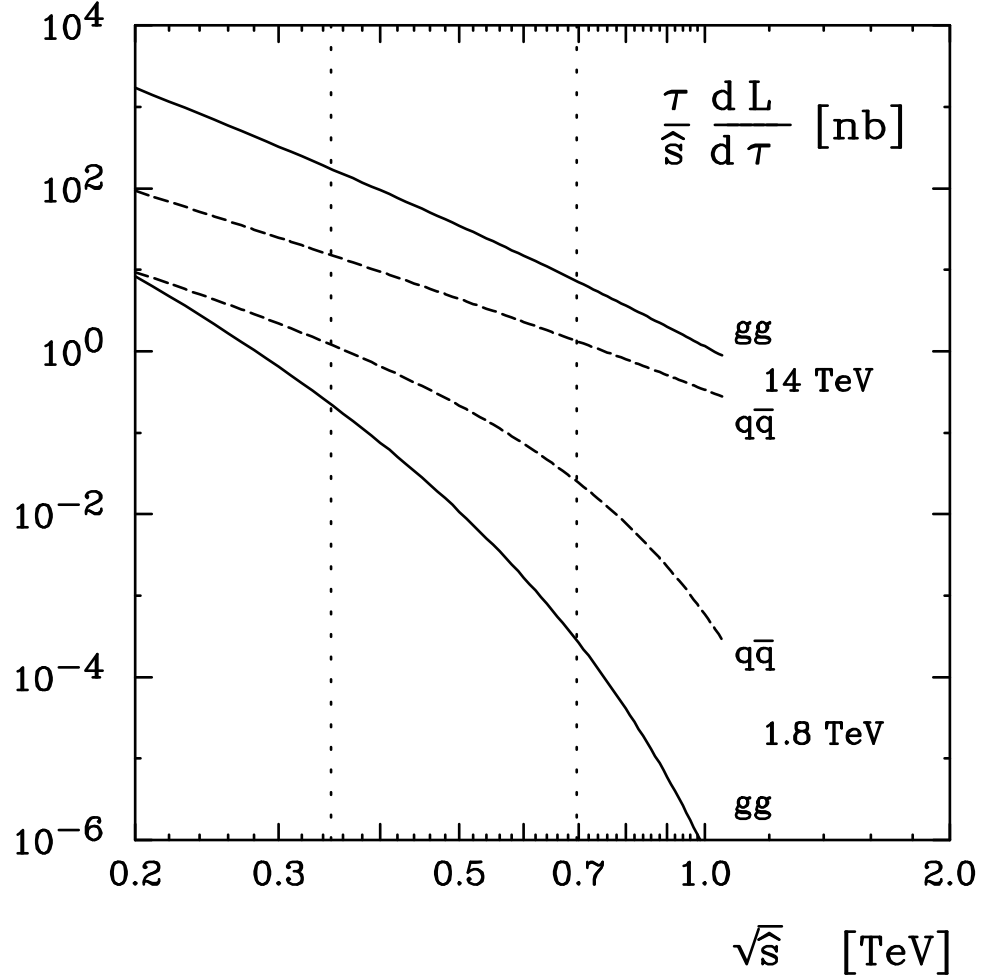


Figure 1.9: Parton luminosities for the Tevatron (Run I) and LHC [3]. The lines show the differential luminosity as a function of the parton interaction energy $\sqrt{\hat{s}}$. The top set of lines labeled 14 TeV is for the LHC, and the lower set labeled 1.8 TeV is for the Tevatron. The vertical dotted lines are just to guide the eye. The left one is at 350 GeV, the threshold for $t\bar{t}$ production. This plot was calculated for the Tevatron Run I energy of 1.8 TeV, however at 1.96 TeV the curves are expected to be similar. Also this plot is shown just as an illustration.

It is possible to measure the gluon-fusion fraction another (indirect) way. Gluons are more likely to radiate low p_t gluons than quarks, and these radiated gluons leave charged tracks in the detector. Here the charged track multiplicity is used to discriminate gluon-fusion $t\bar{t}$ events (more tracks) from quark-annihilation events (few tracks). This has been done at CDF [27]. There are some drawbacks to this method. The method depends on the interpretation of the number of track, whether any difference is truly due to the production method (gluon-fusion) or some other issue. Our method is direct and more robust in nature as we rely strictly on the properties of the top quark.

In the next chapter we will give a brief overview of the CDF Run II detector, followed by a detailed description of our analysis.

Chapter 2

Experimental Apparatus

To study the $t\bar{t}$ production mechanism, we must first produce and then detect $t\bar{t}$ events. At Fermilab, the first part is done with the Tevatron. The Tevatron collides protons and antiproton with sufficient energy to produce $t\bar{t}$ pairs. We then use the CDF II detector to detect the final state particles that allow us to reconstruct the products of the initial interaction. This chapter describes the Tevatron and CDF II as they pertain to this analysis.

2.1 Tevatron

The Tevatron is currently the world's most powerful particle collider, colliding protons and antiprotons at a center of mass energy (\sqrt{s}) of 1.96 TeV. However, the Tevatron is only the final part of the Fermilab accelerator chain, shown in Figure 2.1. There are several steps that take place to prepare the protons and antiprotons before injection into the Tevatron.

2.1.1 Proton Source

The process to produce the protons starts with hydrogen gas, H . A Cockroft-Walton [28] chamber produces H^- ions that are accelerated, using an electrostatic field, to 750 KeV. The beam is then fed through a magnetic transfer line that delivers the H^- ions to the Linac. The Linac [29] is divided into two parts. The first half uses drift tubes to accelerate the H^- beam to 116 MeV. The second half uses side-coupled cavities to further accelerate the beam to 400 MeV.

The Linac feeds the H^- beam into a synchrotron about 150 meters in diameter, the Booster [30]. As the ions are injected into the Booster, they pass through a carbon

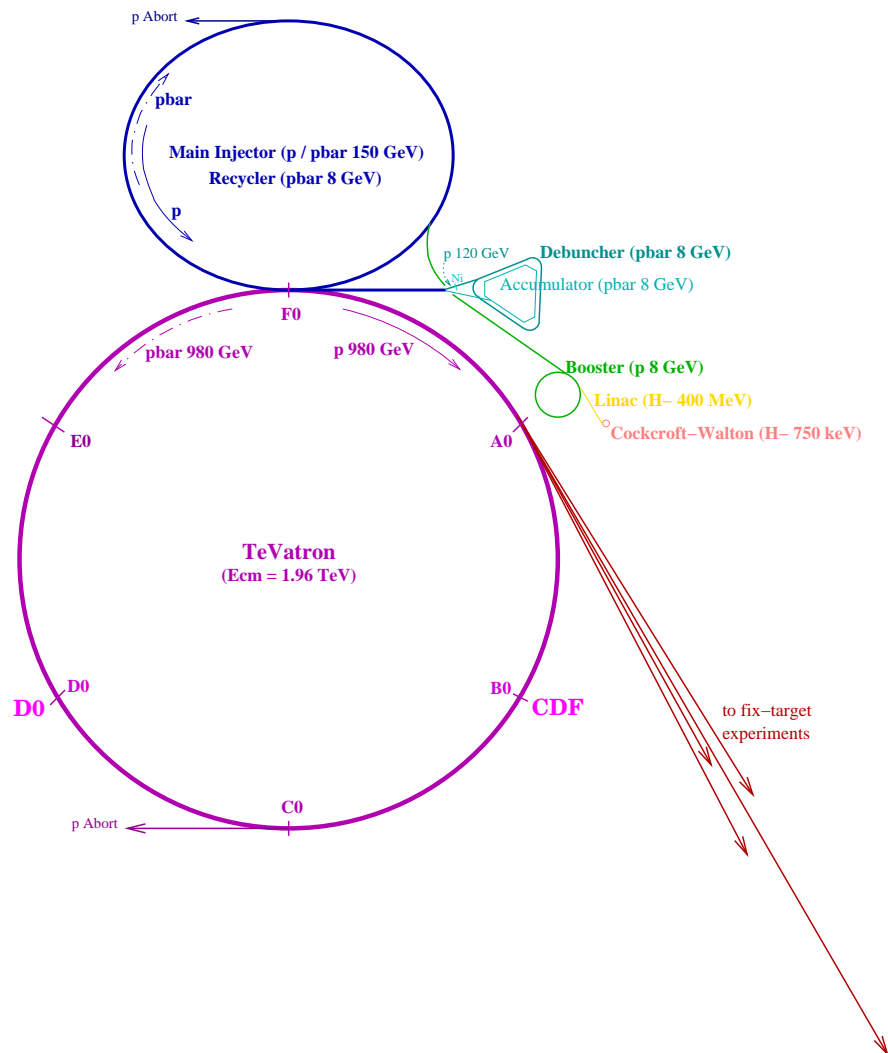


Figure 2.1: Schematic of the Fermilab accelerator chain.

foil that strips away the electrons leaving just the protons. The Booster is designed to receive multiple injections from the Linac to increase the intensity of the proton beam. After the protons are loaded, they are accelerated to 8 GeV.

2.1.2 Main Injector

The Main Injector [31] is a synchrotron about 950 meters in diameter, that has several uses. It accepts protons from the Booster, and accelerates them to 150 GeV for injection to the Tevatron. The Main Injector also accelerates protons to 120 GeV for use in production of the antiproton. Finally, it provides 120 GeV protons to fixed target experiments, which can be done in conjunction with antiproton production.

2.1.3 Antiproton Source

Antiprotons are difficult to produce, and this is the largest limiting factor to the number of collisions we can produce at Fermilab. To maximize the antiproton efficiency, one wants to reduce the lateral momentum, or *cool*, the antiprotons to confine the particles to as small a phase space as possible, much like a lens focusing a beam of light. This reduces antiproton losses during acceleration and transfer between systems of the accelerator chain.

The Main Injector accepts protons from the Booster, and accelerates them to 120 GeV. These protons are directed to a nickel target. When the beam strikes the target a shower of secondary particles is produced. The spray of particles is collimated using a lithium lens [32], which is cylindrical piece of lithium through which a current is run. A dipole magnet is then used to select all negatively charged particles with a momentum of 8 GeV. Approximately 100,000 protons are needed to produce 1 antiproton.

The antiprotons are then injected into the Debuncher [32], a triangular synchrotron with a mean radius of about 90 meters. The antiprotons coming off the target have a momentum spread. The Debuncher reduces the beam size and momentum spread. Before more beam can be sent to the target, the antiprotons in the Debuncher are injected to the Accumulator [32], which is housed in the same tunnel as the Debuncher.

As the name suggests, the Accumulator accumulates the antiprotons in preparation for high energy physics collisions. More cooling of the antiprotons happens while they are stored in the Accumulator.

Because antiprotons are so precious, the Recycler [33] was built to collect the antiprotons from the Tevatron after a *store*, the time the Tevatron is colliding beams. The Recycler is housed in the same tunnel as the Main Injector and constructed of permanent magnets and designed to store the antiprotons at 8 GeV. In practice, the Recycler has never been used to collect antiprotons from a previous store. However, it is very useful and important to help the Tevatron generate high luminosity. At 3 km in circumference, it is much larger than the Accumulator. This enables us to store and cool the antiprotons more efficiently. The Accumulator has an approximate storage limit of 10×10^{10} antiprotons. The Recycler, with electron cooling [34], regularly stores $200 - 300 \times 10^{10}$ antiprotons with a design goal of 600×10^{10} antiprotons.

2.1.4 High Energy Collisions

Now that we have protons and antiprotons, the Main Injector is first used to accelerate the protons to 150 GeV and inject them into the Tevatron. Then the Main Injector accepts antiprotons from either the Accumulator or Recycler, before accelerating the antiprotons to 150 GeV and injecting them into the Tevatron.

The Tevatron [35] is a synchrotron 2 km in diameter composed of superconducting magnets. It is the world's highest energy collider operating at a center of mass energy of 1.96 TeV. The beam in the Tevatron is structured such that the protons (and antiprotons) form three trains separated by 2621 ns. This 2621 ns *abort gap* is important for the safety of the detectors (CDF and D0) as well as the Tevatron infrastructure. The spacing allows the abort system to charge the *kicker* magnet that is used to divert the beam out of the Tevatron. This reduces the chance of beam being sprayed into sensitive areas of the detectors. The train are further structured into 12 bunches separated by 396 ns. Table 2.1.4 summarizes the current performance of Run II accelerator.

After the protons and antiprotons are injected to the Tevatron they are accelerated to 980 GeV. In the regions surrounded by the CDF and D0 detectors, quadrupole

Center of mass energy	1.96 TeV
Number of bunches	36×36
Bunch length	0.37 m
Bunch spacing	396 ns
Collision frequency	1.7 Mhz
Protons per bunch	$\sim 300 \times 10^9$
Antiprotons per bunch	$\sim 30 \times 10^9$
Proton beam width (at collision)	$\sim 25 \mu\text{m}$

Table 2.1: Tevatron Run II performance.

magnets are used to reduce the beam size to increase the luminosity. The instantaneous luminosity is defined in Equation 2.1:

$$\mathcal{L} = \frac{f N_B N_p N_{\bar{p}}}{2\pi(\sigma_p^2 + \sigma_{\bar{p}}^2)} \quad (2.1)$$

where N_B is the number of bunches, $N_p(N_{\bar{p}})$ is the number of protons (antiprotons) per bunch, f is the bunch crossing rate, and σ_p ($\sigma_{\bar{p}}$) is the effective width of the proton(antiproton) beam.

2.2 Collider Detector at Fermilab (CDF II)

The Collider Detector at Fermilab (CDF II) is a general purpose detector positioned at one of the interaction points of the Tevatron. The layout of the detector follows the standard design features for collider experiments, essentially a cylinder centered around the collision interaction point. The detector subsystems are: (from the inside out) the tracking system, solenoid magnet, electromagnetic calorimetry, hadronic calorimetry, and muon detectors. Schematics of CDF II are shown in Figures 2.2 and Figures 2.3. All these systems will be discussed in detail in this section. Henceforth we will refer to CDF II merely as CDF.

2.2.1 Detector Coordinates

It is now important to define the coordinate systems that we use at CDF. Not only will this be useful while describing the detector, it will also be important when describing

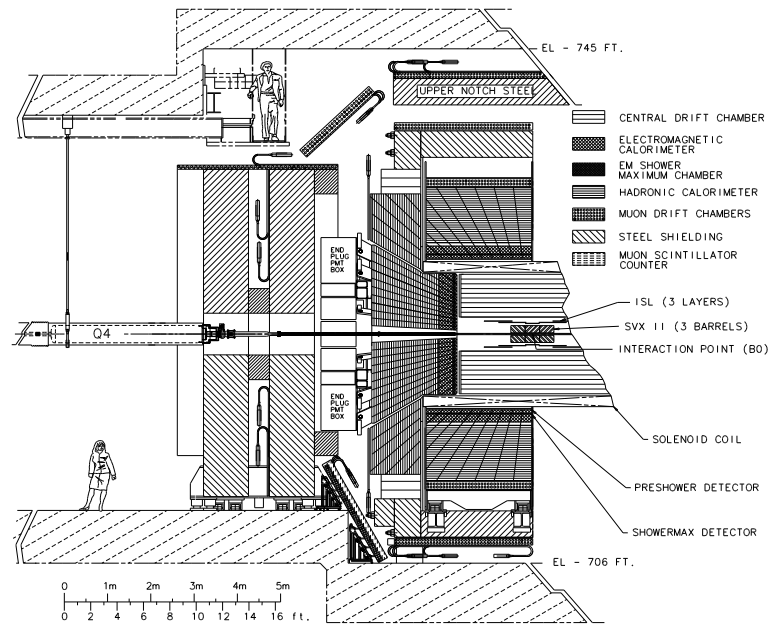


Figure 2.2: An elevation view of half of the CDF II detector.

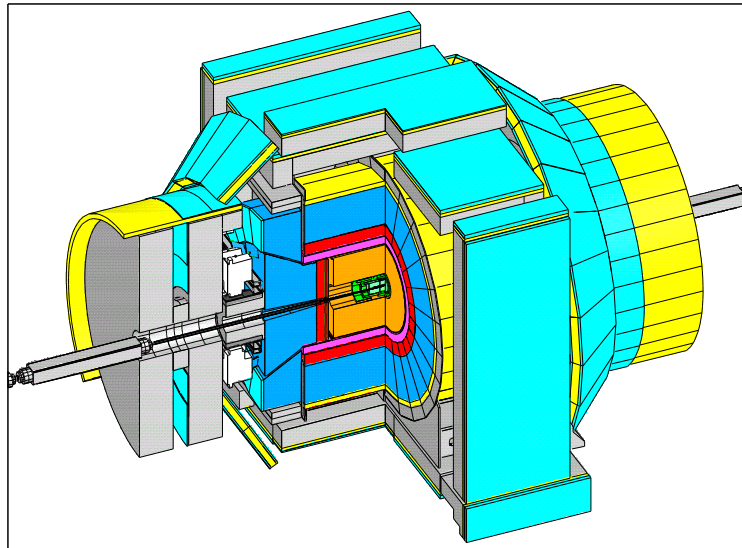


Figure 2.3: Open cutaway of the CDF II detector.

the analysis. CDF used a standard right handed coordinate system with the z axis along the direction of the proton beam, the x axis radially out from the plane of the Tevatron, and the y axis pointing to the roof of the detector. The origin is defined by the detector's geometric center

It is usually more convenient to use a polar coordinate system (r, θ, ϕ) defined by Equations 2.2-2.4.

$$r = \sqrt{x^2 + y^2 + z^2} \quad (2.2)$$

$$\phi = \tan^{-1}\left(\frac{y}{x}\right) \quad (2.3)$$

$$\theta = \cos^{-1}\left(\frac{z}{r}\right) \quad (2.4)$$

Defining our coordinates this way is fine for non-relativistic experiments. However θ is not invariant under relativistic boost. Since the collisions are actually interactions of the partons in the proton and antiproton a difference in longitudinal momentum can lead to the interaction being boosted along the z axis. The rapidity, Equation 2.5, is invariant under this boost.

$$\zeta \equiv \frac{1}{2} \log \frac{E + p_z}{E - p_z} \quad (2.5)$$

In the relativistic case, $p \gg m$, the rapidity can be expressed as Equation 2.6,

$$\eta \equiv \frac{1}{2} \log \frac{p + p_z}{p - p_z} = -\log \tan \frac{\theta}{2} \quad (2.6)$$

where ζ is reduced to the geometric quantity, pseudo-rapidity (η).

Since η is invariant under boost, the coordinate system of (r, η, ϕ) is used throughout the following sections.

2.2.2 Charged Particle Tracking

The inner most part of CDF is used for the spatial tracking and momentum measurement of charged particles. The tracking detectors are located within a superconducting solenoid 5 meters long, 3.2 meters diameter which generates a 1.4 T magnetic field parallel to the z axis. Electrically charged particles within the field will follow a helical path. The charge and momentum of a particle can be determined by the curvature of its trajectory. The tracking system is composed of two types of detectors: silicon

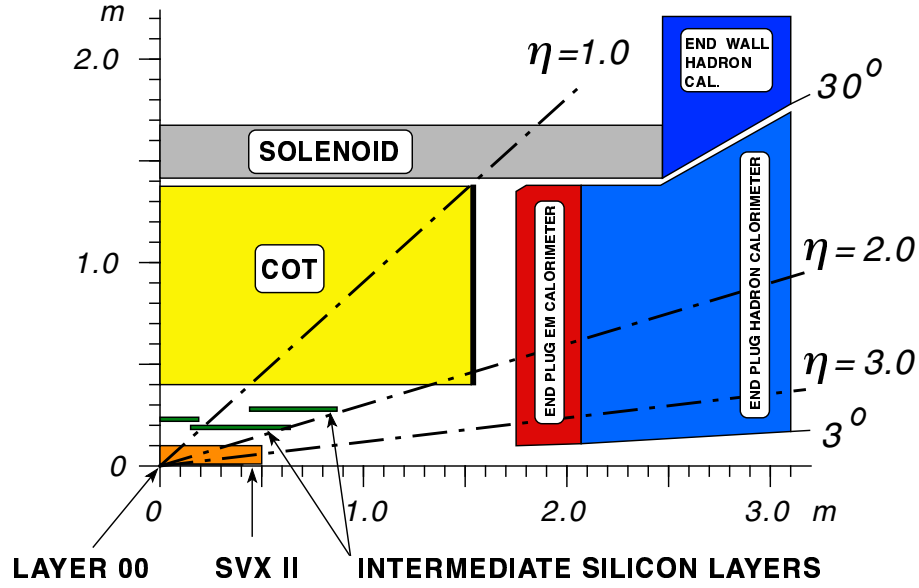


Figure 2.4: One quadrant of the CDF II tracking volume projected in the y - z plane.

micro strip detectors and open-cell drift chambers. Both of these types of detectors reconstruct the charged particle's path from ionization caused by the particle interacting with matter (silicon or gas). A view of the tracking system can be shown in Figure 2.4.

Silicon Detector

The silicon micro strip detectors have closely spaced strips (60-140 μm) of p -type silicon implanted in a lightly doped n -type silicon substrate. CDF uses both one sided and two sided silicon detectors. The one sided detectors have the opposite side covered with a thin layer of strongly doped n -type silicon (Figure 2.6), while the double sided detectors have closely spaced strips of strongly doped n -type silicon separated with strips of p -type silicon. Voltage is applied across the chip to deplete the bulk n -type of free electrons. The voltage also creates an electric field so when a charged particle traverses the chip the ionization travels through the bulk to be detected by the strips. The single sided chips have strips to measure r - ϕ or *axial* component, while the double sided chips have axial strips on one side and orthogonal strips or small angle strips on the other measure r - z or *stereo* component.

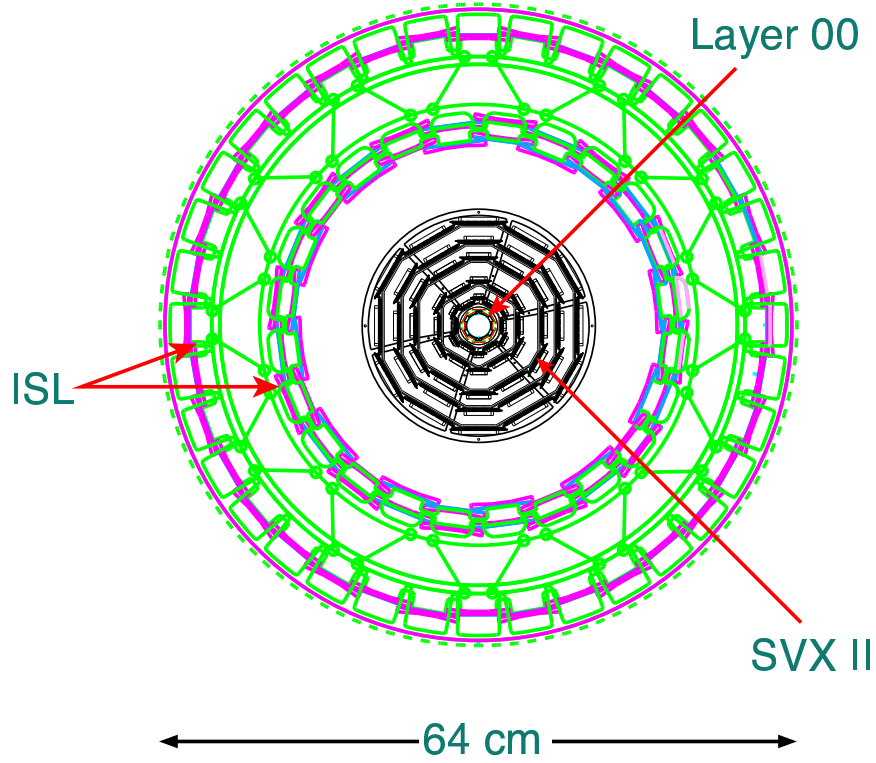


Figure 2.5: Silicon Endview (As if looking down the beam pipe): The silicon detector chips are arranged cylindrically supported by a composite strut system.

The silicon micro strip detectors are arranged into three structures (from inside to outside): Layer 00, the Silicon Vertex Detector, and the Intermediate Silicon Layer, a transverse view is shown in Figure 2.5.

Layer 00 [36] (L00) is composed of single-sided radiation-hard detectors with a readout pitch of $50 \mu\text{m}$. These are mounted to a carbon fiber structure affixed directly around the beam pipe.

The Silicon Vertex Detector [37] (SVX) is the main silicon tracker. SVX is constructed of three barrels each 29 cm long. Each barrel supports five layers of double sided silicon. Layer 0, the inner most layer, sits at a radius of 2.5 cm, while Layer 4, the outer most layer, sits at a radius of 10.6 cm. Layers 0, 1, and 3 measure $r - \phi$ with one side and $r - z$ on the other using orthogonal strips. Layers 2 and 4 measure $r - \phi$ with one side and $r - z$ on the other using small angle strips (1.2° and -1.2° respectively).

The Intermediate Silicon Layer [38] (ISL) is composed of double side detectors at a

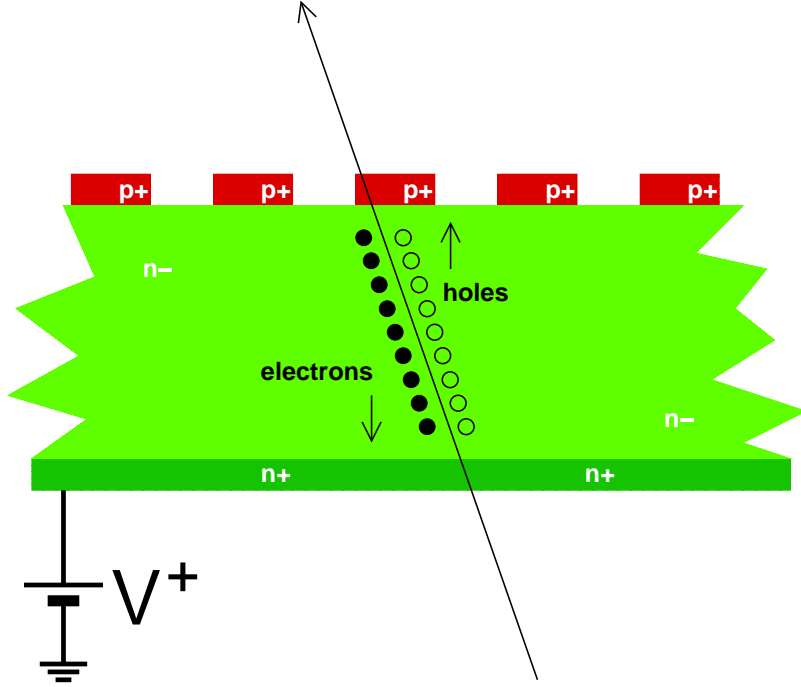


Figure 2.6: Cartoon rendering of a single sided silicon strip detector.

radius of 19 cm to 30 cm, Figure 2.7. The primary use of the ISL is to match tracks in the SVX to tracks in the outer tracker.

Currently the impact parameter resolution of SVX, in combination with ISL, is about $40 \mu\text{m}$ which includes a $30 \mu\text{m}$ contribution from the beam width. The resolution for the z of the primary interaction (z_0) is about $70 \mu\text{m}$. With this level of precision it is possible to distinguish the primary vertex from the $p\bar{p}$ collision, from a secondary vertex (Section 3.2.3) from the decay of B hadron or other long-lived particle.

Central Outer Tracker

The Central Outer Tracker [39] (COT), situated within the solenoid but outside the silicon, is also designed to measure trajectories of charged particles in three dimensions. An multi-wire open-cell drift chamber, it extends from 44 cm to 132 cm in radius and $|z| < 155 \text{ cm}$, with an angular coverage of $|\eta| < 1$ Figure 2.4.

The open-cells are constructed of field panels and potential wires that create an

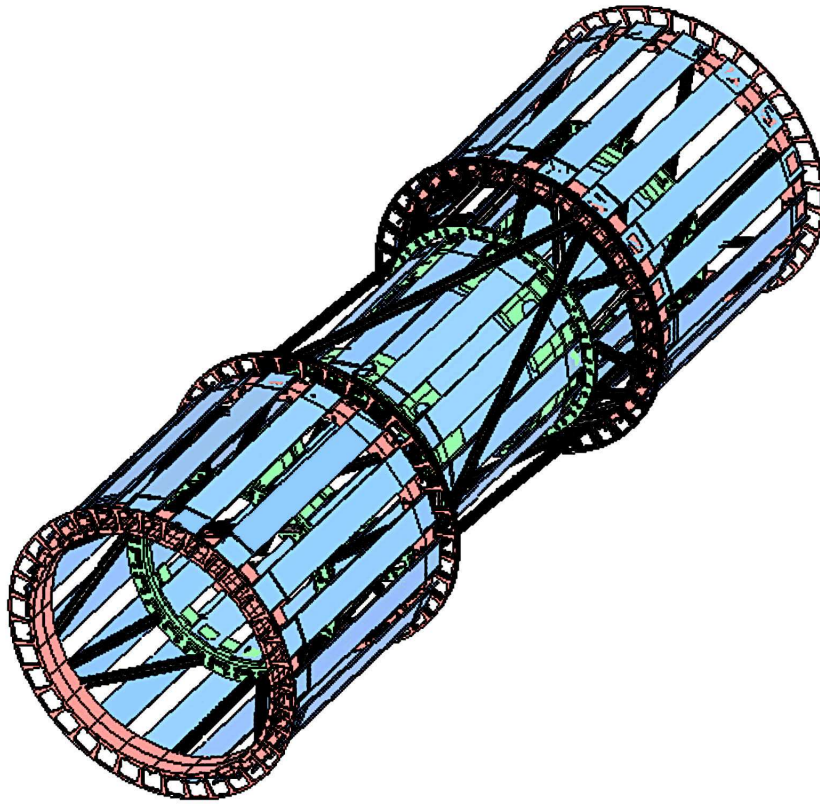


Figure 2.7: Intermediate Silicon Layer (ISL): The outer most silicon layer designed to extend the silicon tracking in η beyond the edge of the wire drift chamber (COT).

electric field and sense wires which read-out the ionization left by charged particles. Because of the magnetic field of the solenoid, the ionization does not drift in the direction of electric field. The optimal angle for the drift chambers is 35° from the radial (Figure 2.9). This insures that the ionization drifts perpendicular to high energy charged particle.

The cells are arranged in 8 superlayers Figure 2.8 and filled with a mixture of argon, ethane, and isopropyl alcohol gas in the ratio of 500:500:173. Every other superlayer has their wires tilted by 3° relative to the magnetic field, so the COT can measure $r - z$ as well as $r - \phi$.

The momentum resolution for tracks with only COT information is $\delta p_T/p_T \simeq 0.3\% \frac{p_T}{(\text{GeV}/c)}$ but when combined with the SVX this drops to $\delta p_T/p_T \simeq 0.1\% \frac{p_T}{(\text{GeV}/c)}$.

2.2.3 Energy Measurement

CDF uses a system of calorimeters to measure the energy of the final state particles. The calorimeters are made of lead or iron alternated with scintillator that detects the shower of particles from interactions with the dense materials. CDF utilizes both electromagnetic and hadronic calorimeters.

The electromagnetic calorimeters, composed of lead, measure electrons and photons by detecting showers from bremsstrahlung. As the electron traverses the material, it radiates a photon, which creates an e^+e^- pair. Photons from the primary interaction can also create e^+e^- pairs. Each particle of the pair in turn radiates photons. This electromagnetic (EM) showering process continues until the energy loss due to ionization exceeds the threshold of the pair production mechanism. To characterize this we use the radiation length X_0 , which is the mean distance for the e^\pm to lose all but $\frac{1}{e}$ of its energy by bremsstrahlung. The EM shower is collected by photo-multiplier tubes and used to determine the energy of the original electron or photon.

The hadronic calorimeters, composed of iron, measure hadrons by detecting the hadronic shower due to strong interaction with bulk metal material. The mean free path of a particle before undergoing a strong interaction is called the interaction length, λ . Charged particles in the shower scintillate photons that are collected by photo-multiplier

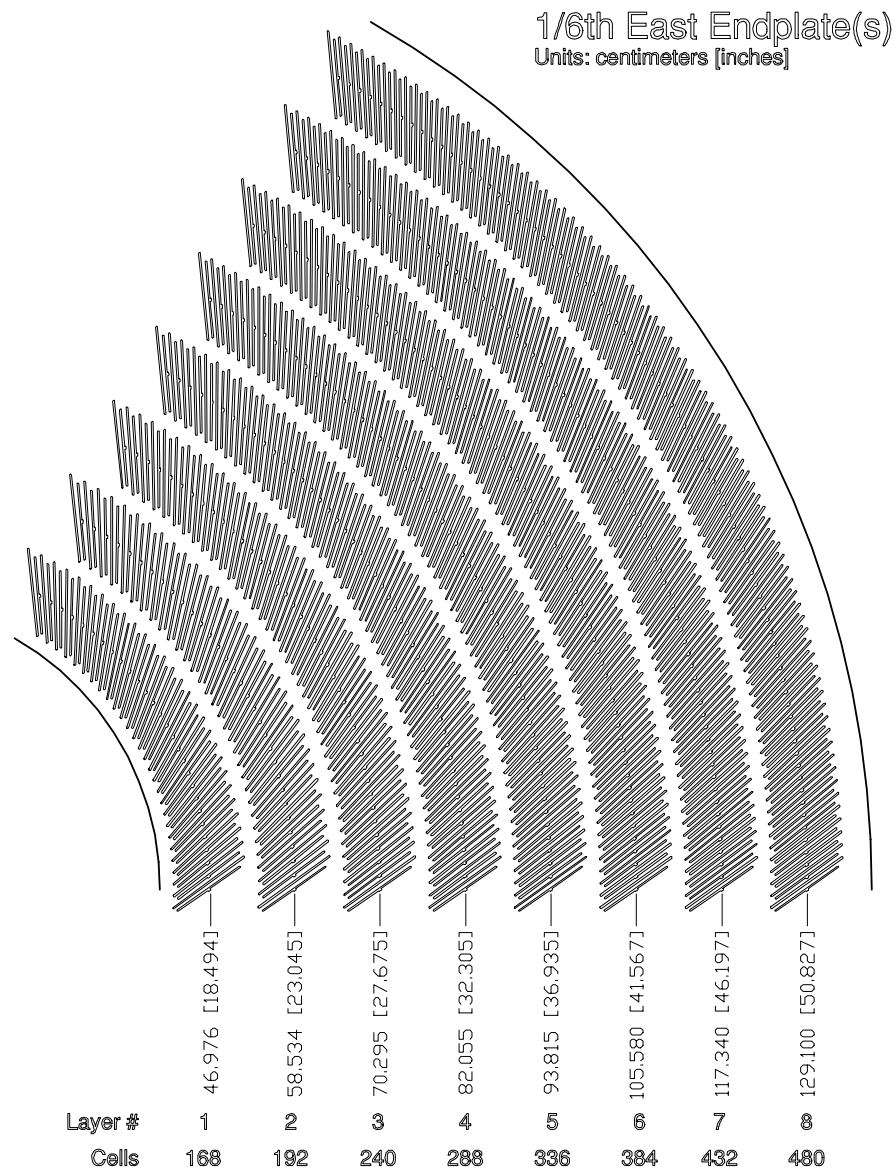


Figure 2.8: COT Superlayers: 1/6 of the east plate. Notice the cells are tilted with respect to the radial direction. This is to account for the charge drift due to the presence of a strong magnetic field. The cells are arranged into 8 *superlayers*.

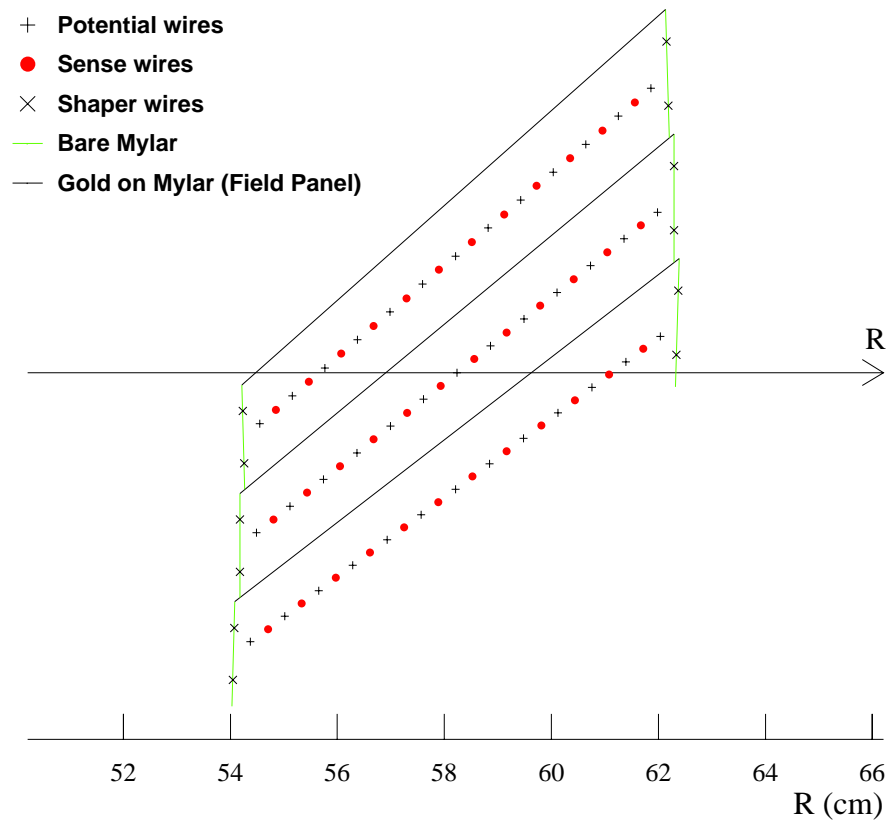


Figure 2.9: Schematic of the COT cells. The arrow show the radial direction. Notice that the cells are tilted 35° with respect to the radial direction.

tubes.

Matched hadronic and electromagnetic calorimeters insure good coverage for all types of particles. The calorimetry is divided into three regions that combine to provide coverage of 2π in azimuth and up to $|\eta| = 3.6$. The components of the calorimetry are: the Central Electromagnetic, the Central Hadronic, the Wall Hadronic, the Plug Electromagnetic, and the Plug Hadronic.

Extending out to an $|\eta| < 1.1$, the Central Electromagnetic Calorimeter (CEM) is segmented into wedges, 15° in ϕ with each wedge divided into towers spaced 0.1 in $|\eta|$. The CEM is 18 radiation lengths. Embedded 6 X_0 in the CEM is the Shower Maximum Detector (CES). The CES provides position information about the shower. Radially behind the CEM is the Central Hadronic Calorimeter (CHA). The CHA is 4.7 interaction lengths, and extends out to $|\eta| < 0.9$. More information about the central calorimeters can be found here [40, 41].

The Plug Electromagnetic Calorimeter (PEM) is segmented into wedges 7.5° in ϕ with each wedge divided into towers 0.1 in $|\eta|$ over $1.1 \lesssim |\eta| \lesssim 1.8$. In the far forward region, $2.1 \lesssim |\eta| \lesssim 3.6$, the towers are spaced 0.2 in $|\eta|$. The PEM also contains the Plug Shower Maximum Detector (PES). Similar to the CES, the PES provides position measurement of the EM shower. The Plug Hadronic Calorimeter (PHA), has as a similar tower structure to PEM. More information about the plug calorimeters can be found here [40, 42].

The Endwall Hadronic Calorimeters [40] (WHA) covers the small region around $0.7 \lesssim |\eta| \lesssim 1.2$. The WHA is similar in construction to the CHA, and serves to cover the gap between the central region and the plug region.

Table 2.2.3 shows the specifications for the calorimeters at CDF.

2.2.4 Muon Detector

Muons pose a special problem (and opportunity) for a high energy physics experiment. Muons, which are 200 times more massive than electrons, do not lose large amounts of energy through bremsstrahlung. This means they are not detectable with our EM calorimetry. CDF uses a dedicated system to detect muons that is located outside

	Central and Endwall	Plug
EM		
Thickness	$19X_0, 1\lambda$	$21X_0, 1\lambda$
Sample(Pb)	$0.6X_0$	$0.8X_0$
Sample(scintillator)	5 mm	4.5 mm
Sampling resolution	$11.6\%/\sqrt{E_T}$	$14.0\%/\sqrt{E_T}$
Stochastic resolution	$14.0\%/\sqrt{E_T}$	$16.0\%/\sqrt{E_T}$
HAD		
Thickness	4.5λ	1λ
Sample(Pb)	1 inch (central) 2 inch (endwall)	2 inch
Sample(scintillator)	10 mm	6 mm
energy resolution	$75\%/\sqrt{E_T}$	$80\%/\sqrt{E_T}$

Table 2.2: The specifications for the calorimeters at CDF.

the calorimetry. A layer of steel shielding is located between the muon system and the calorimetry. This shield serves to block charged hadrons that may traverse the calorimetry and be misinterpreted as muons.

Much like the calorimetry, the muon system is subdivided into regions. However, unlike the calorimetry the muon system does not give full coverage in ϕ . The muon system consists of the Central Muon Detector (CMU), Central Muon Extension (CMX), the Central Muon Upgrade (CMP), and the Intermediate Muon Detector (IMU). The coverage of the muon system is shown in Figure 2.10.

Located directly behind the CHA and a layer of steel is the Central Muon Detector (CMU). Constructed of a stacked array of drift tubes with rectangular cells, the CMU can detect muons with $p_t > 1.4$ GeV/ c in the region $|\eta| < 0.6$. Also covering the range $|\eta| < 0.6$, the Central Muon Upgrade (CMP) is located outside the CMU behind an additional layer of steel shielding. CMP detects muons with $p_t > 2.2$ GeV/ c . The Central Muon Extension (CMX) and Intermediate Muon Detector (IMU), combine to extend the total muon coverage out to $|\eta| < 2.0$. More information about the muon system can be found here [40, 43]

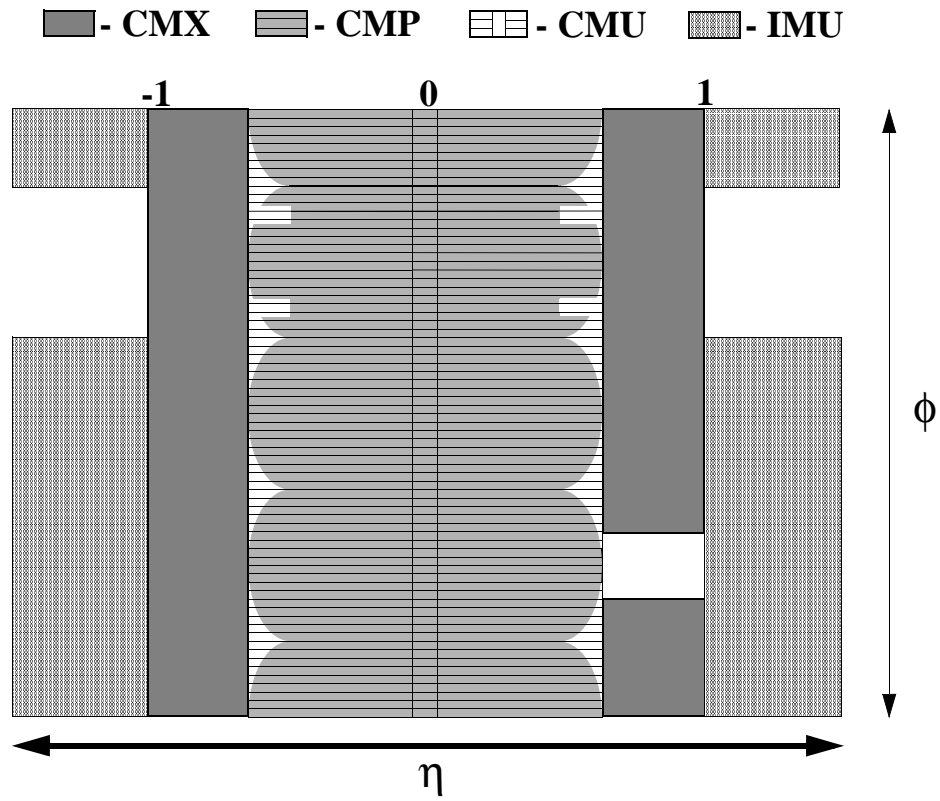


Figure 2.10: Muon coverage in η and ϕ . The hole in the IMU and CMX are due to mechanical requirements (cabling, cooling, etc).

2.2.5 Trigger and Data Acquisition

The Tevatron has one beam crossing, or *event*, every 396 ns. Of these events, only a fraction are of physics interest. CDF utilizes a selection system, or *trigger*, to select the interesting events before they are recorded. This keeps us from having to record every event, which would be difficult both because of the limitations of storage as well as the limitations of the electronics used to read out the data. Our trigger is composed of three levels that sequentially reduce the data rate. A schematic of the trigger system is shown in Figure 2.11.

Designed to quickly select events, the first level of the trigger, Level 1 (L1), looks at simple physics quantities within the event. L1 has three synchronous streams: one for data from the calorimetry, one for data from the COT and one for data from the muon system. The calorimetry stream decision can be based not only the energy deposited in the calorimeter, but also the calculated magnitude of unbalanced, or *missing*, transverse energy. Missing transverse energy can be a signature for neutrinos. The tracking decision is made by the Extremely Fast Tracker [44] (XFT). Using dedicated custom electronics, the XFT uses information from the COT to quickly reconstruct 2 dimensional tracks in the event. The track information can be used by itself to trigger on quantities like p_t . The information can also be combined with EM calorimetry or the muon detectors to trigger on electrons or muons. L1 also has a buffer where it can store up to 42 events, and has a decision time of 5.5 μ s. L1 reduces the data rate from ~ 2 MHz to less than 20 kHz, the maximum accept rate for L1.

The events accepted by L1 are passed to the second level of the trigger, conveniently named Level 2 (L2). L2 is a programmable processor that can do a simple reconstruction of the event. L2 clusters the towers of the calorimetry adding more detailed information enabling us to tighten the L1 requirement. L2 also utilizes SVX information to tighten track selection criteria. L2 can buffer up to 4 events, and has a decision time of 20 μ s. L2 has a maximum data rate of 300 Hz.

Level 3 (L3) consists of two components: the event builder (EVB) and a processing farm. The EVB collects and formats all the data for events passing L2. The EVB then

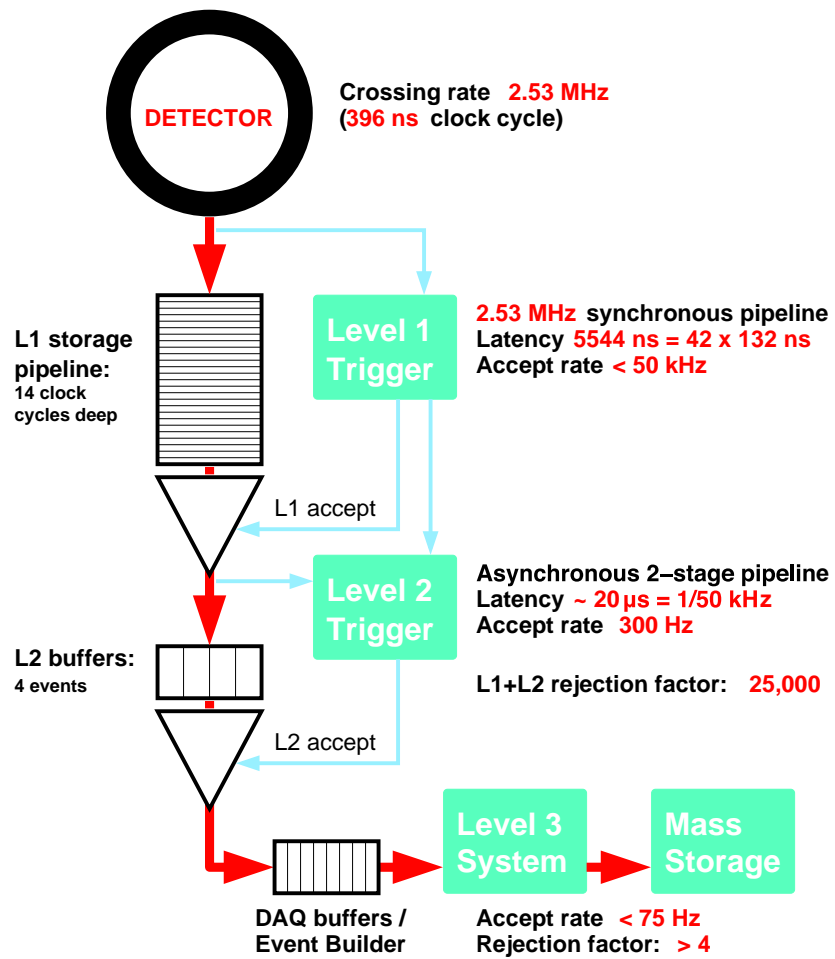


Figure 2.11: Schematic of the CDF data acquisition system.

passes the formatted event to a PC farm with approximately 300 CPU's. A node in the PC farm then reconstructs the events using essentially the same algorithms used in our final analysis. The maximum data rate of L3 is 75 Hz. Event passing L3 are then passed to a data handling system and stored to tape.

Chapter 3

Event Selection

The events of interest in this analysis are the lepton+jets $t\bar{t}$ channel described in Section 1.3. Recall that in the Standard Model top quarks decay $\sim 100\%$ of the time to $W + b$, and that in the lepton+jets $t\bar{t}$ channel one W decays to quarks, and the other W decays to $e\nu_e$ or $\mu\nu_\mu$.

The event selection is based on the CDF $t\bar{t}$ cross section measurement, and is described in detail here [45]. We summarize the event selection in this section.

3.1 Trigger

As discussed in Section 2.2.5, CDF uses a triggering system to select interesting events that will be recorded for later analysis. For this analysis, we use triggers that select events with a high momentum electron or muon candidate.

Electron candidates require an XFT track with $p_T > 8$ GeV/c pointing to a cluster in the EM calorimeter with $E_T > 16$ GeV. Muon candidates require an XFT track with $p_T > 8$ GeV/c pointing to hits in the CMUP or CMX.

3.2 Particle Identification

Events selected by the trigger are then processed to reconstruct all the objects in the event. Once the events are reconstructed, we select those events that are consistent with the lepton+jets signature.

3.2.1 Lepton Identification

Electrons are identified by a track with $p_T > 10$ GeV/c that is matched to an energy cluster in the EM calorimeter with $E_T > 20$ GeV/c. To reduce rate that photons or hadrons are misidentified as electrons, we require the ratio of cluster energy to track momentum and the ratio of electromagnetic energy to hadronic energy to be consistent with those for electrons.

Muons are identified by a track with $p_T > 20$ GeV/c, that is matched to hits in the muon detectors. The calorimeter tower that matches the track must have energy consistent with a minimum-ionizing particle. Cosmic ray muons are removed by requiring that the track originate at the origin of the detector and is within the timing of the beam crossing. A complete description of the lepton selection can be found here [45]. We require either one identified electron or one identified muon.

3.2.2 Hadronic Jets

The final state quarks from the initial interaction hadronize, then shower into charged and neutral particles. We call this shower a *jet*. Jets are identified by looking for clusters of energy in the calorimeter that are constrained within a cone of radius $\Delta R = 0.4$, where:

$$\Delta R = \sqrt{\Delta\phi^2 + \Delta\eta^2} \quad (3.1)$$

Towers in the calorimeter are assigned such that no tower contributes to more than one jet. More info about jet clustering can be found here [46]. We correct the energy for known effects and inefficiencies. A complete description of the correction procedure can be found here [47]. We require at least four jets with $E_T > 15$ GeV and $|\eta| < 2$.

3.2.3 b -jet Identification using Secondary Vertexing

The identification of b quarks is important for this analysis. Most of the backgrounds for $t\bar{t}$ events are W +jets which come from non- $t\bar{t}$ processes that do not contain any heavy flavor (b or c). Requiring at least one b quark greatly reduces the background.

Of course, b quarks are identified after hadronization. The mean lifetime of b -hadrons is ~ 2 ps [48], at Tevatron energies. Because of this long lifetime, b -hadrons traverse a relatively large distance before they decay further. This distance is ~ 1 mm. The b -hadron will decay into several charged particles. The tracks left in the detector by these particles can be used to construct a displaced secondary vertex. Recall the impact parameter resolution of the silicon is $\sim 40 \mu\text{m}$, Section 2.2.2. The process of identifying a jet with secondary vertex is called SECVTX b -tagging or b -tagging.

The primary event vertex is determined by fitting all prompt tracks to a common point constrained by the interaction region. Jets with at least two high quality tracks within the jet cone ($\Delta R = 0.4$), are checked for b -tags. If a secondary vertex can be constructed, the distance between the primary vertex and secondary vertex along the jet direction is calculated as the projection in the xy plane. This distance, L_{xy} , along with its uncertainty, σL_{xy} , are calculated. If $L_{xy}/\sigma L_{xy} > 7.5$, the jet is considered as being tagged. We require at least one of the jets to be tagged.

An illustration of tagging is shown in figure 3.1. A complete description of the b -tagging can be found here [45].

3.2.4 Neutrino Identification: \cancel{E}_T

Neutrinos can not be directly detected. However, we are able to infer their presence when there is a large asymmetry of energy in the calorimeter. The missing E_T (\cancel{E}_T) is calculated:

$$\cancel{E}_T = - \sum_i E_T^i \mathbf{n}_i \quad (3.2)$$

where E_T^i is the magnitude of transverse energy in calorimeter tower i , and \mathbf{n}_i is a unit vector in the transverse plane that points to the tower. If an isolated muon is found in the event, the \cancel{E}_T is corrected by replacing the energy in the calorimeter attributed to the muon with p_T of the muon track. We require $|\cancel{E}_T| > 20 \text{ GeV}$.

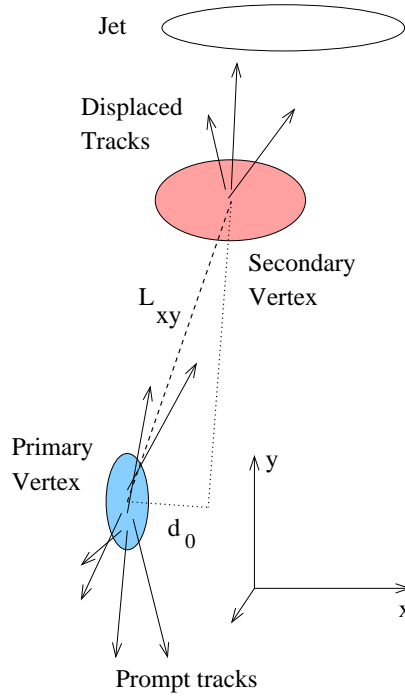


Figure 3.1: Illustration of a displaced vertex: L_{xy} is the distance from the primary vertex to the secondary vertex along the projection of the candidate jet onto the $x-y$ plane. The value L_{xy} is the variable of merit when assigning a secondary vertex tag, what we call a b-tag.

Sample	b-tag Fraction	N_{data}
1-tag	0.720	167
2-tag	0.280	65

Table 3.1: Number of events observed in data (N_{data}) and b-tag fraction for events with one and two or more tagged jets.

3.3 Selected Events

This analysis uses data corresponding to a total integrated luminosity of 955 pb^{-1} collected from March 2002 to February 2006. In this data we find 232 events satisfying the ≥ 1 -tag selection criteria, 167 events with exactly one tagged jet (1-tag) and 65 events with two or more tagged jets (2-tag). Table 3.1 shows the b-tag fraction and the number of events observed in data (N_{data}) for 1-tag and 2-tag events.

3.4 Backgrounds Estimation

The *lepton + jets* selection provides a data sample that has a high $t\bar{t}$ purity. The requirement of at least one b-tag further enhances this purity. However there are still events that pass all the selection criteria that are not $t\bar{t}$. These *backgrounds* depend strongly on the number of jets with b-tags. The dominant background is $W + 4jets$. These event contain either real heavy flavor quarks (c, b) or light flavor quarks that are mistagged. Other processes that contribute are non- W (QCD) events, diboson WW , WZ , or ZZ events, and the single top.

These backgrounds were well studied in the CDF top cross-section analysis [49]. We do not expect the background composition to change for our dataset, so we scale the background prediction by the increase in luminosity. An overview of the method to determine the background is presented below.

3.4.1 $W + 4jets$

The $W + 4jets$ background is composed of several processes. The largest is W produced in conjunction with heavy flavor quarks (b and c). However, there is also a contribution

Sample	Signal Fraction (\bar{C}_s)	b-tag Fraction	N_{data}	N_{bkg}
1-tag	0.837 ± 0.020	0.720	167	27.3 ± 3.4
≥ 2 -tags	0.960 ± 0.010	0.280	65	2.6 ± 0.7

Table 3.2: Estimated signal fraction (\bar{C}_s), b-tag fraction and number of events observed in data (N_{data}) and estimated background (N_{bkg}) for events with one and two or more b-tags.

from W produced with light flavor quarks. These events enter our sample when one of the light flavor quarks is b-tagged. Monte Carlo is used to model these processes. ALPGEN is used for generation and HERWIG is used to shower the particles. Because of the uncertainty due to the Q^2 scale and next-to-leading order effects, the normalization is obtained from the data. To do this, we use the events without requiring any tags. After subtracting expected contribution from $t\bar{t}$ and non- W , a fit is done for the number of $W + 4jets$ events.

3.4.2 Other Backgrounds

There are several smaller background non- W (QCD multijet) events, diboson WW , WZ , or ZZ events, and the single top. For the non- W (QCD multijet) background, the sideband region of lepton isolation vs. missing E_T is used after subtracting for the $t\bar{t}$ and $W + 4jets$. Diboson and single top are taken from Monte Carlo. Table 3.2 shows the total background for each tag sample.

Chapter 4

Analysis Method

4.1 Measurement Strategy

The measurement is performed over a set of events selected according to the lepton+jets selection criteria defined in Chapter 3. This sample is composed mainly of three processes: $t\bar{t}$ produced via gluon-fusion ($t\bar{t}^{gg}$), $t\bar{t}$ produced via quark annihilation ($t\bar{t}^{qq}$), and background from $W + 4jets$ (WJ).

The strategy of the measurement is based on the different kinematic properties of these three processes. These properties are characterized by variables defined in Section 4.3. These variables are then fed into a Neural Network (NN) which is trained to distinguish gluon-produced $t\bar{t}$ events from quark-produced $t\bar{t}$ events (see section 4.4.1). This NN is then used to make three templates (T^{gg} , T^{qq} , T^{WJ}) utilizing simulated events. The generation of the simulated events, or what we call *Monte Carlo* (MC), is described in Section 4.2.

A likelihood, as a function of the gluon content C_f , is constructed based on the templates. This likelihood function is used to determine the most probable value of C_f (C_f^{fit}) and its error. Because of the small size of the sample, it is possible to get unphysical (negative) values from the fitting procedure. To deal with possible negative values of the C_f^{fit} the Feldman-Cousins (FC) [50] statistical approach is used. This approach returns values of C_f^{true} constrained between 0 and 1 for all values of C_f^{fit} . The FC approach also allows for a natural transition from one-sided to two-sided confidence level limits. The application of FC statistics to this analysis is discussed in Chapter 5.

4.2 Simulated Events

This analysis uses simulated events, usually referred to as *Monte Carlo*, to model our signal events, $t\bar{t}$, and our background events, $W + 4jets$. These events are used in two ways. First they are used to construct the templates that we use to fit for the amount of each component in our data, and second, they are used to generate the pseudo-experiments used to determine the uncertainty for any particular value measured in the data. These two procedures will be described in more detail in Section 4.4 and Chapter 5.

The signal $t\bar{t}$ events are generated with **HERWIG** [51]. The **HERWIG** generator uses leading-order matrix elements to generate the hard scattering interaction, and then hadronizes and showers the resulting particles. **HERWIG** includes the $t\bar{t}$ spin correlations which are important in this analysis since we want to use the spin information to distinguish gluon-fusion events ($t\bar{t}^{gg}$) from quark-annihilation events ($t\bar{t}^{qq}$). We generate one sample of $t\bar{t}^{qq}$ events and one sample of $t\bar{t}^{gg}$ events each with a top mass of $175 \text{ GeV}/c^2$.

The background for our lepton+jets sample is dominated by $W + 4jets$. To generate these events, we use **ALPGEN** [52]. **ALPGEN** is a leading-order matrix element generator that is very good at handling events with a large number of jets. The events generated with **ALPGEN** are then passed to **HERWIG** for showering. We assume the background composition comes entirely from $W + 4jets$, where the jets can come from either heavy flavor (c or b) or light flavor (u, d, s). We make an assumption that the shapes of the all other backgrounds are very similar to W plus light flavor jets. We address this assumption later in our estimate of the systematic uncertainties, Chapter 6. The specific Monte Carlo datasets we use are summarized in Table 4.1.

After generation, all Monte Carlo is passed through a detailed simulation of the CDF detector. The simulation of the generated particles in the detector produces an event format that is identical to the real (data) events.

Process	Generator	Size
$t\bar{t}$:		
$m_t = 175 \text{ GeV } (t\bar{t}^{gg})$	HERWIG	$\sim 2\text{M}$ events
$m_t = 175 \text{ GeV } (t\bar{t}^{qq})$	HERWIG	$\sim 2\text{M}$ events
backgrounds:		
$W + 4p$	ALPGEN+HERWIG	$\sim 1.4\text{M}$ events
$Wbb + 2p$	ALPGEN+HERWIG	$\sim 1\text{M}$ events
$Wcc + 2p$	ALPGEN+HERWIG	$\sim 1\text{M}$ events
$Wc + 3p$	ALPGEN+HERWIG	$\sim 1\text{M}$ events

Table 4.1: Summary of Monte Carlo data sets used to model signal and background.

4.3 Event Reconstruction

4.3.1 Kinematic Fitter

An advantage of the lepton+jets selection is that it is possible to fully reconstruct the top quarks. To do this we use the kinematic fitter developed for the CDF top mass analysis [53]. We assume all events are $t\bar{t}$. The four jets with the largest transverse energy are assumed to be the four quarks from the top and W decays. Before employing the fitter, the jet and lepton energies are corrected for known effects. We constrain the top mass to be $175 \text{ GeV}/c^2$, and the energy scale of the jets are allowed to fluctuate within their uncertainty. All permutations of jets to partons matches that are consistent with the b-tag information are tried and the permutation that yields the lowest χ^2 , despite its value, for the hypothesis is assumed to yield the correct reconstruction of the event. A full description of the fitter can be found here [53].

4.3.2 Kinematic Variables

Once we have a full reconstruction from the fitter we can select the variables used to differentiate $t\bar{t}^{gg}$ from $t\bar{t}^{qq}$. We use a total of 8 variables, two of which describe the production and six of which describe the decay of the $t\bar{t}$ event.

The choice of basis is important in maximizing the discriminating power of each of the variables. As suggested by Mahlon and Parke in [54], we choose the so-called *off-diagonal* basis [55]. The off-diagonal basis is defined on an event by event case,

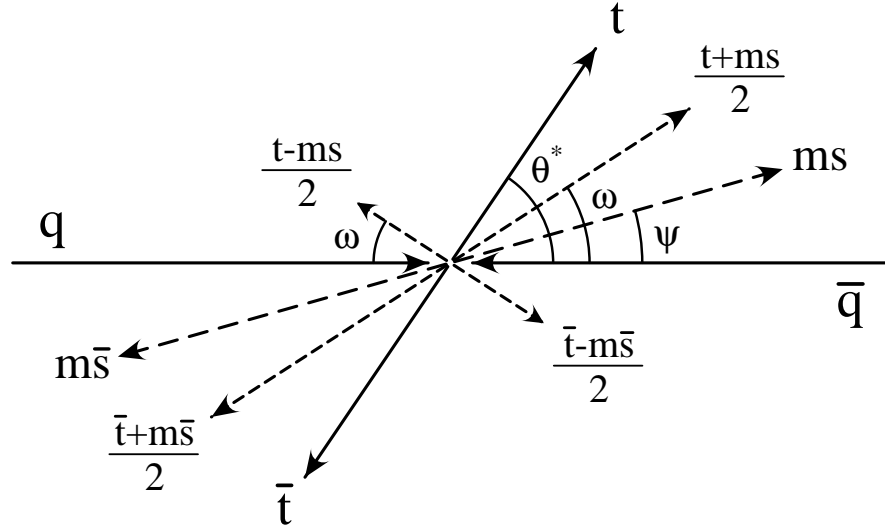


Figure 4.1: These are the relevant angles in the zero momentum frame of the initial interaction for the off-diagonal basis described in [55]. The top quark is produced at an angle θ^* with respect to the beam axis shown by q and \bar{q} . The spin vector s makes an angle ψ with respect to the beam axis. The vectors $\frac{t \pm ms}{2}$, here m is the top mass, indicate the preferred emission directions for the charged lepton or down-type quark from the decaying W^+ . The vectors describing the antitop are back-to-back with the corresponding top quark vectors.

where ψ gives the angle between the basis and incoming partons in the zero momentum frame.

$$\tan \psi = \frac{\beta^2 \cos \theta^* \sin \theta^*}{1 - \beta^2 \sin^2 \theta^*} \quad (4.1)$$

Here:

- $\cos \theta^*$: the angle between the top quark and the right incoming parton.
- β : the top quark velocity relative to c .

This basis is particularly powerful because the $q\bar{q}$ -annihilation events are produced with unlike spin 100% of the time, while gluon-fusion events are produced primarily with like spin at the $t\bar{t}$ threshold [54], Figure 4.2. Because of the the short lifetime of the top we can exploit this difference. The preferred direction of the charged lepton or down quark from the W decay is given by [55]:

$$\sin \omega = \beta \sin \theta^* \quad (4.2)$$

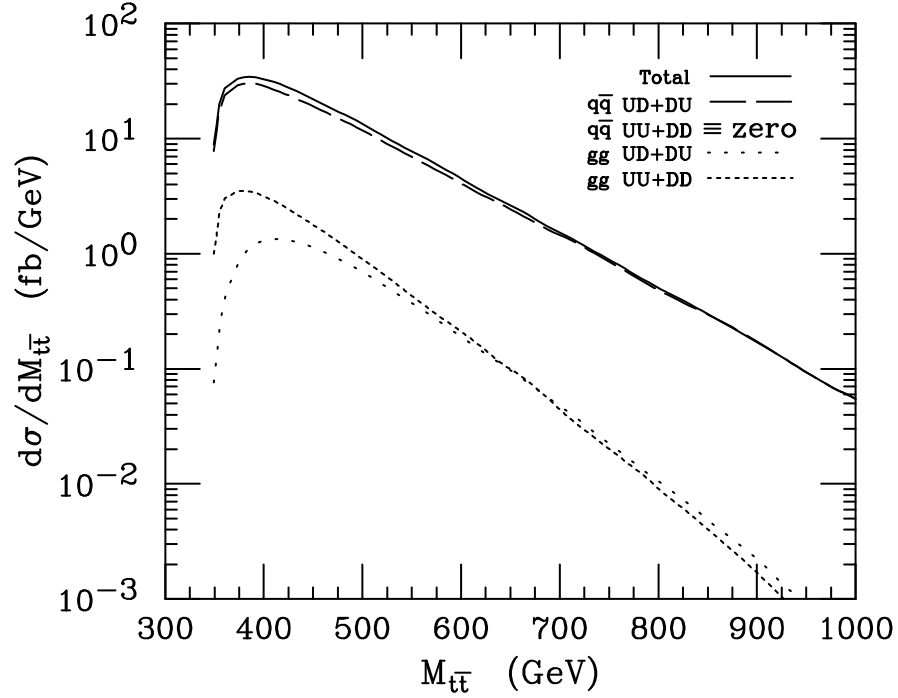


Figure 4.2: Differential cross section for $t\bar{t}$ production as a function of invariant mass of $t\bar{t}$ for the Tevatron with center of mass energy of 2.0 TeV. $q\bar{q}$ -annihilation events are always produced with un-like spin of up-down (UD) or down-up (DU). At the threshold for $t\bar{t}$ (~ 350 GeV), gluon-fusion events are produced primarily with like spins of up-up (UU) or down-down (DD) [55].

As depicted in Figure 4.1, $\sin \omega = \frac{t+ms}{2}$ where m is the top mass. For example, in an UD event we expect the quark (lepton) along the vector $\frac{t+ms}{2}$ and the lepton (quark) along the vector $\frac{\bar{t}+m\bar{s}}{2}$, while for an UU event we expect the quark (lepton) along the vector $\frac{t+ms}{2}$ and the lepton (quark) along the vector $\frac{\bar{t}-m\bar{s}}{2}$.

For this analysis we use the production variables $\cos \theta^*$ and β and the decay variables as follows:

- $\cos \theta_{Wlep}$: angle between leptonically decaying W in the off-diagonal basis.
- $\cos \theta_{lep}$: angle between lepton in the off-diagonal basis.
- $\cos \theta_\nu$: angle between neutrino in the off-diagonal basis.
- $\cos \theta_{Whad}$: angle between hadronically decaying W in the off-diagonal basis.
- $\cos \theta_{up}$: angle between up quark in the off-diagonal basis.

- $\cos\theta_{down}$: angle between down quark in the off-diagonal basis.

For the decay variables, the angles are measured in the top (or antitop) rest frame, while the production variables are evaluated in the $t\bar{t}$ rest frame.

These distributions are shown in Figures 4.3- 4.10 for $t\bar{t}^{gg}$ and $t\bar{t}^{qq}$ events and compared to the background for the 1-tag and ≥ 2 -tags events. They are normalized to unit area.

4.4 Building the templates

4.4.1 Neural Network description

The Neural Network we use is `TMultiLayerPerceptron` [56] which is inherent to `ROOT` [57]. We give it eight input variables, the ones described in Section 4.3.2. We train the NN to distinguish between $t\bar{t}^{gg}$ and $t\bar{t}^{qq}$ events. Two NN were trained, one for the 1-tag events and one for the 2-tag events. We use 2 hidden layers (10 and 5 nodes) and train only on a subsample of our total $t\bar{t}$ event sample. When selecting the number of hidden layers and nodes per layer, we tried a variety of different options, reducing/increasing the numbers of layers and nodes and found that this did not significantly change our discriminating power. A brief description of neural networks can be found in Appendix A.

4.4.2 Templates

We make templates of the *probability* of the event to be $t\bar{t}^{gg}$; this probability is the output of the NN. The distributions of our templates for 1-tag and 2-tag events for $t\bar{t}^{gg}$, $t\bar{t}^{qq}$, and the background are shown in Figure 4.11.

4.4.3 Likelihood

A likelihood as a function of C_f can be obtained for any given sample of events. For the time being, consider C_f to represent the $t\bar{t}^{gg}$ fraction. The event sample is first decomposed into two exclusive samples with 1 and 2 or more b-tagged events. The likelihood of the full sample of events is then simply calculated as the product of the

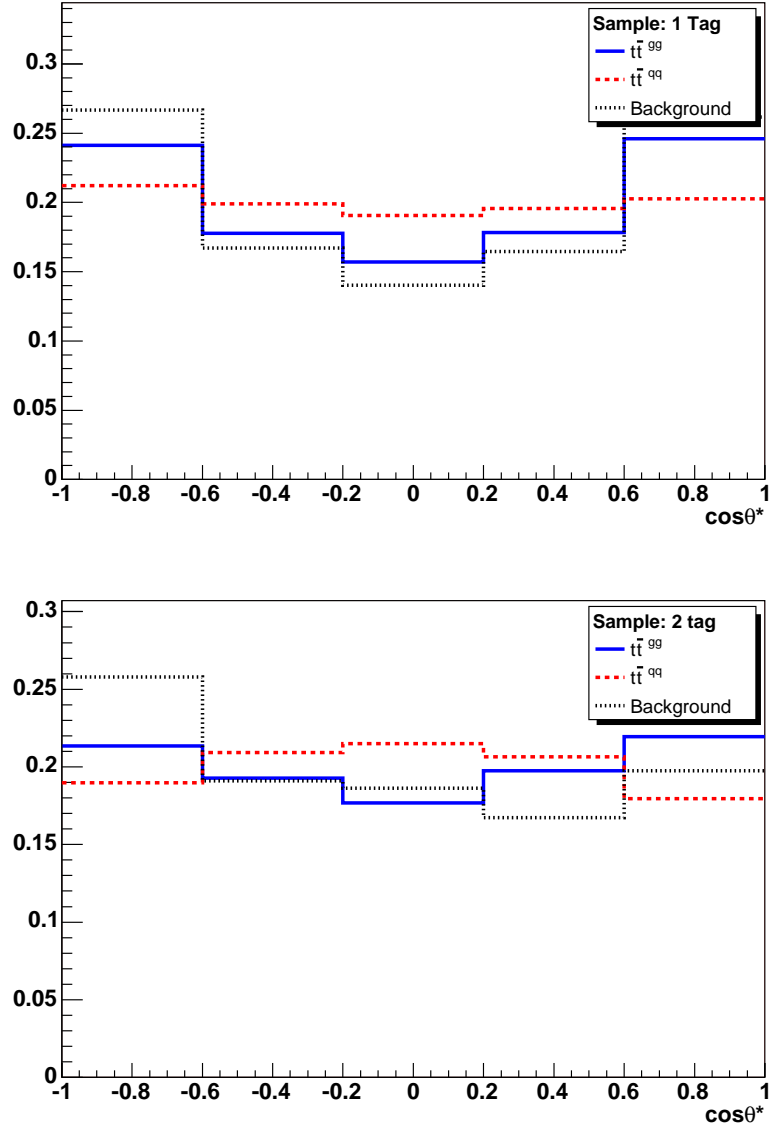


Figure 4.3: Distribution of $\cos\theta^*$ for $t\bar{t}^{gg}$ (blue, solid) and $t\bar{t}^{qq}$ (red, dashed) and background (black, dotted) for 1-tag (top) and ≥ 2 -tags events (bottom).

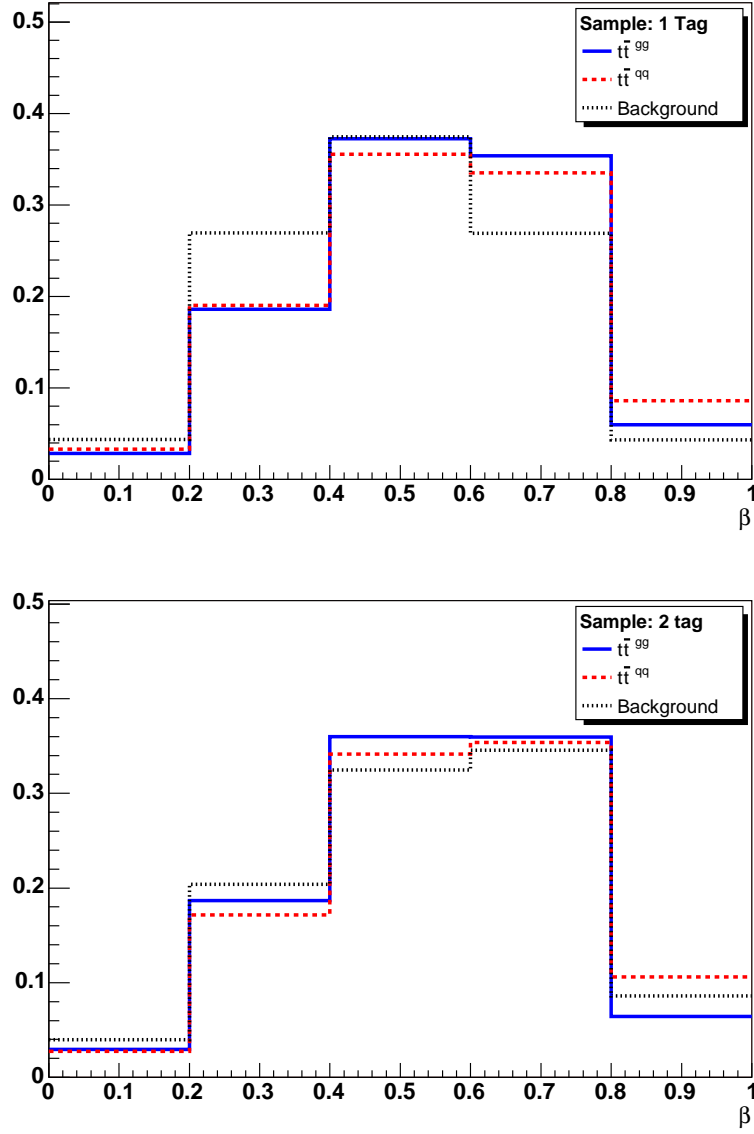


Figure 4.4: Distribution of β for $t\bar{t}^{gg}$ (blue, solid) and $t\bar{t}^{qq}$ (red, dashed) and background (black, dotted) for 1-tag (top) and ≥ 2 -tags events (bottom).

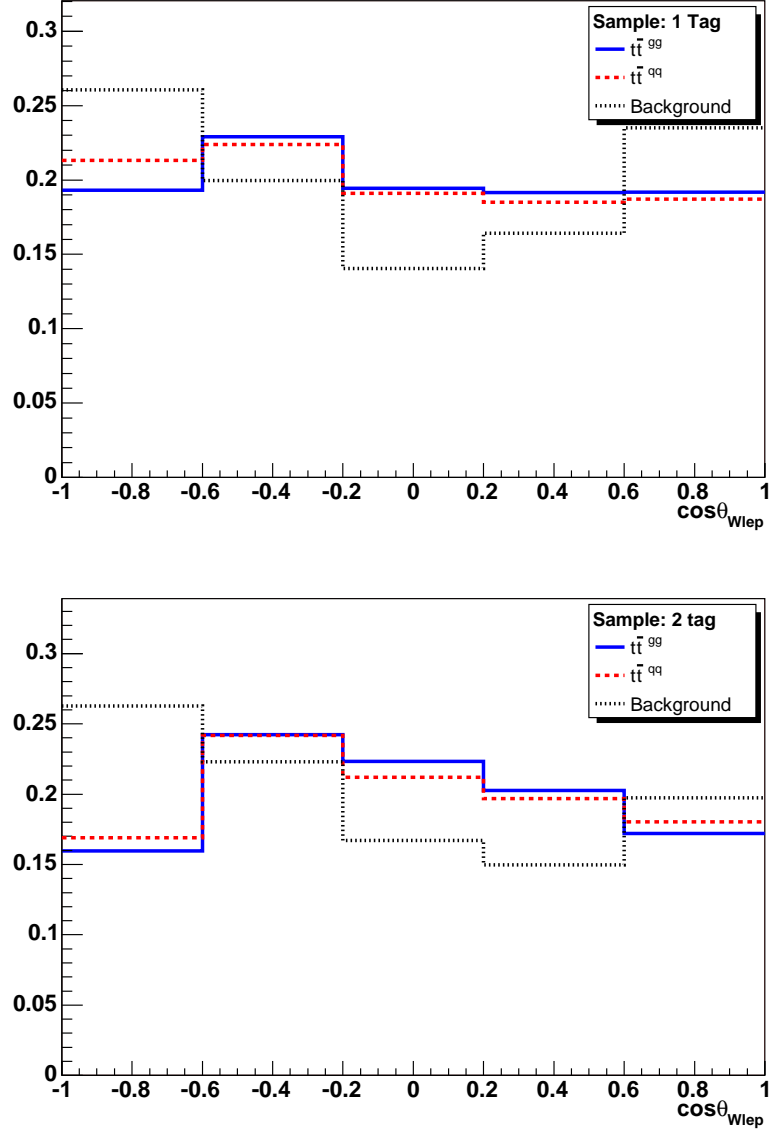


Figure 4.5: Distribution of $\cos\theta_{Wlep}$ for $t\bar{t}^{gg}$ (blue, solid) and $t\bar{t}^{qq}$ (red, dashed) and background (black, dotted) for 1-tag (top) and ≥ 2 -tags events (bottom).

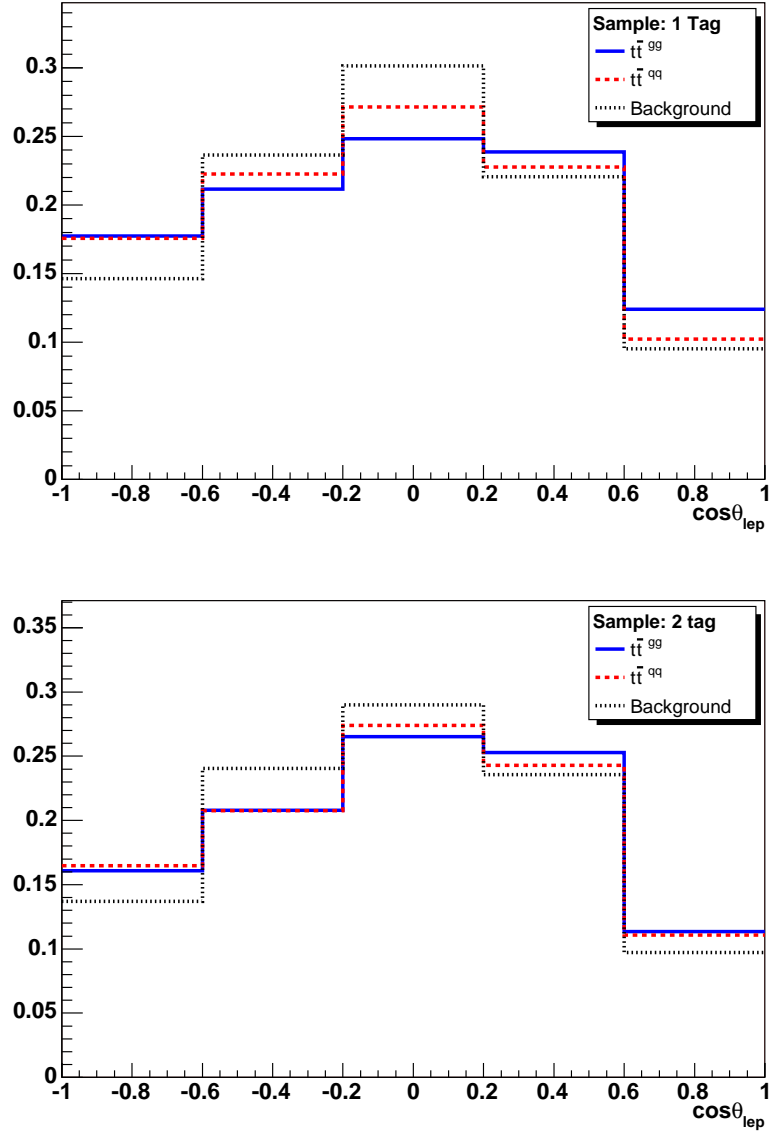


Figure 4.6: Distribution of $\cos\theta_{lep}$ for $t\bar{t}^{gg}$ (blue, solid) and $t\bar{t}^{qq}$ (red, dashed) and background (black, dotted) for 1-tag (top) and ≥ 2 -tags events (bottom).

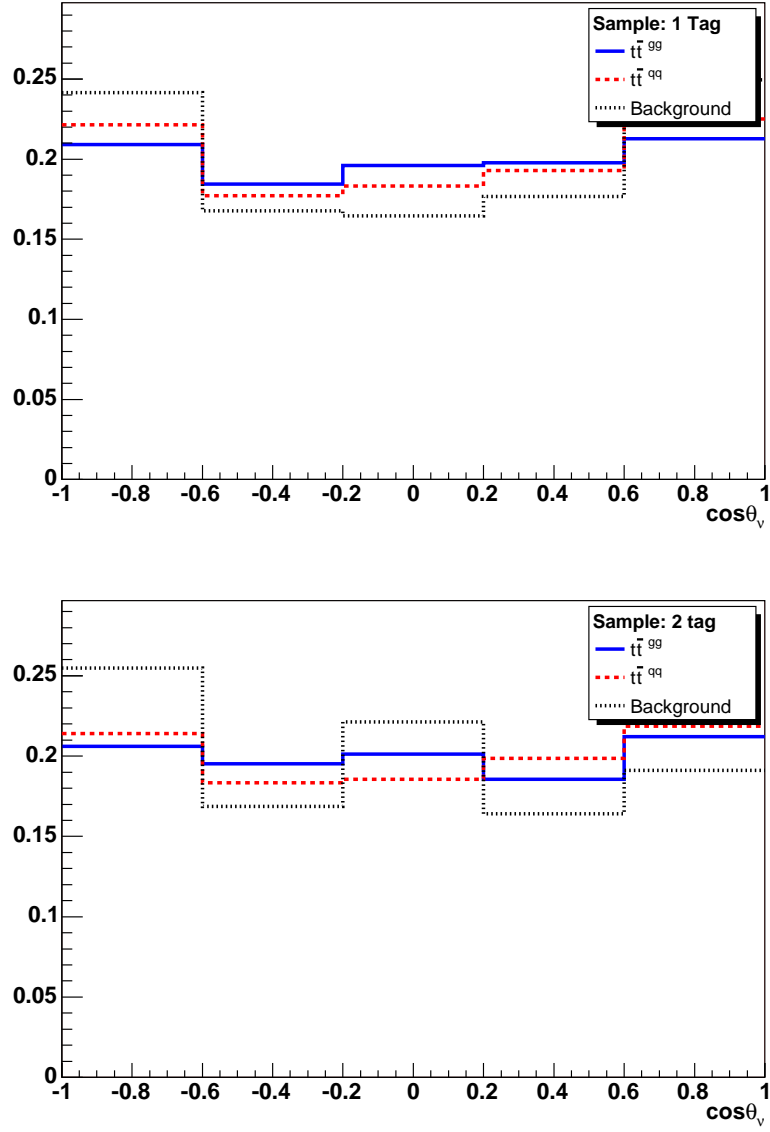


Figure 4.7: Distribution of $\cos\theta_\nu$ for $t\bar{t}^{gg}$ (blue, solid) and $t\bar{t}^{qq}$ (red, dashed) and background (black, dotted) for 1-tag (top) and ≥ 2 -tags events (bottom).

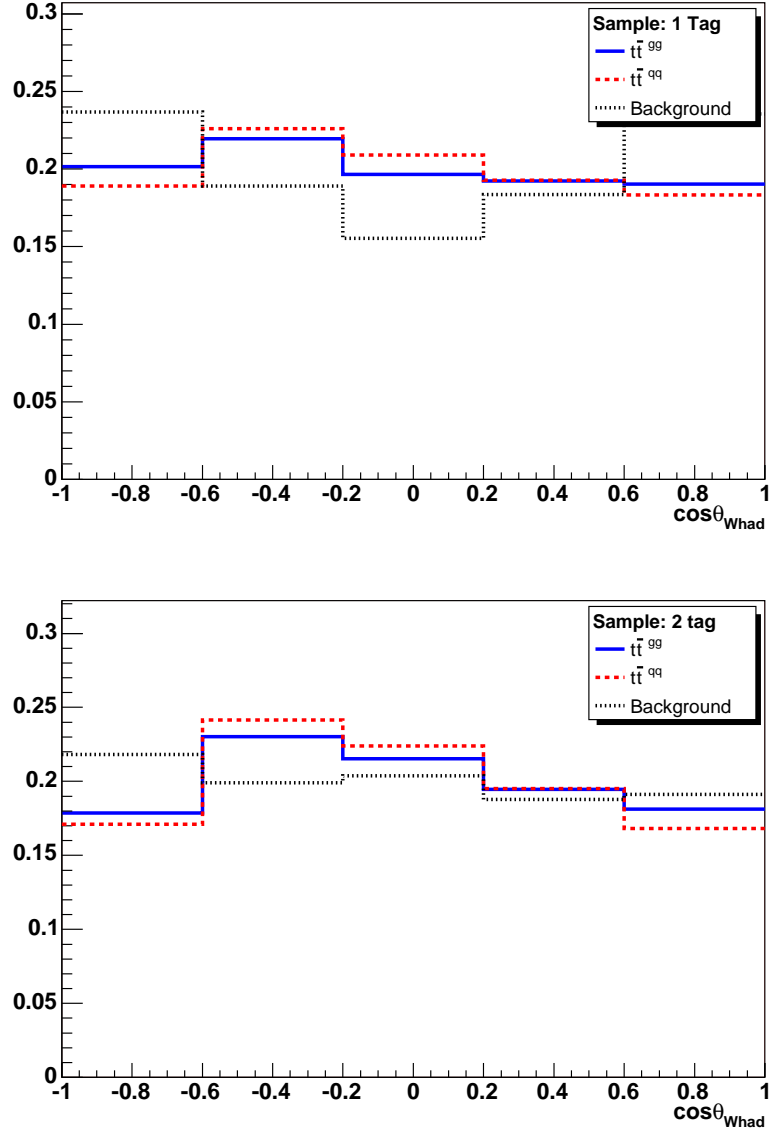


Figure 4.8: Distribution of $\cos\theta_{Whad}$ for $t\bar{t}^{gg}$ (blue, solid) and $t\bar{t}^{qq}$ (red, dashed) and background (black, dotted) for 1-tag (top) and ≥ 2 -tags events (bottom).

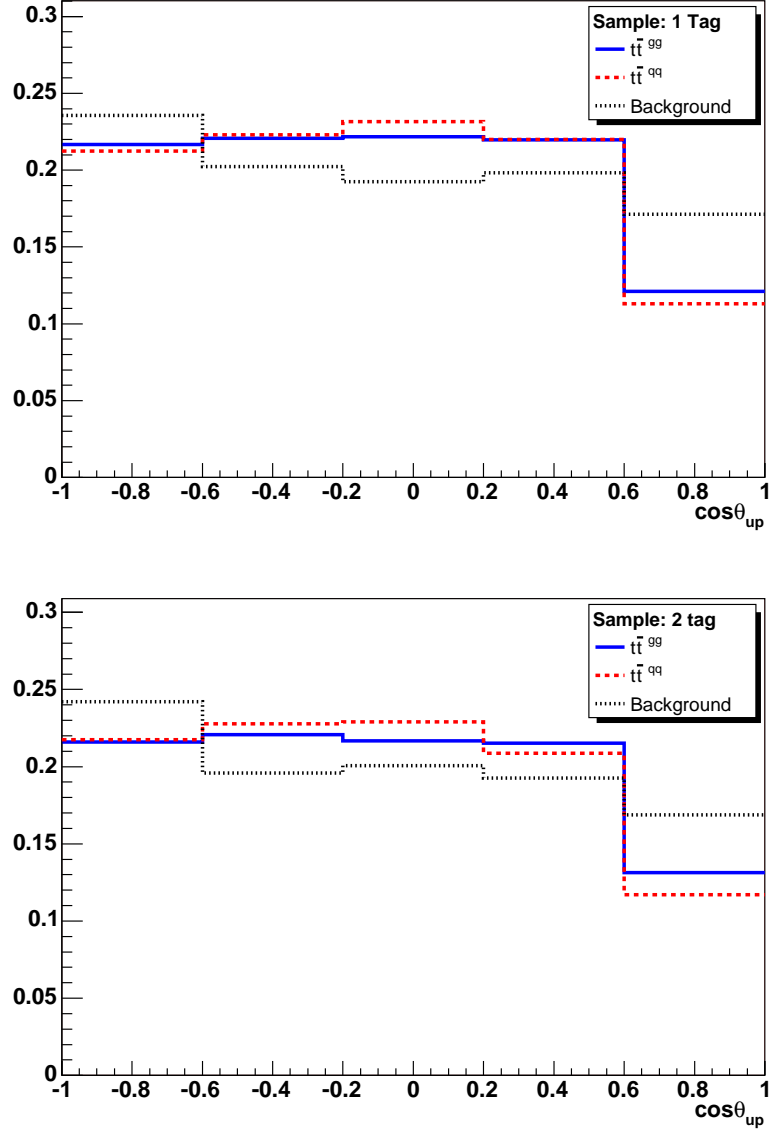


Figure 4.9: Distribution of $\cos\theta_{up}$ for $t\bar{t}^{gg}$ (blue, solid) and $t\bar{t}^{qq}$ (red, dashed) and background (black, dotted) for 1-tag (top) and ≥ 2 -tags events (bottom).

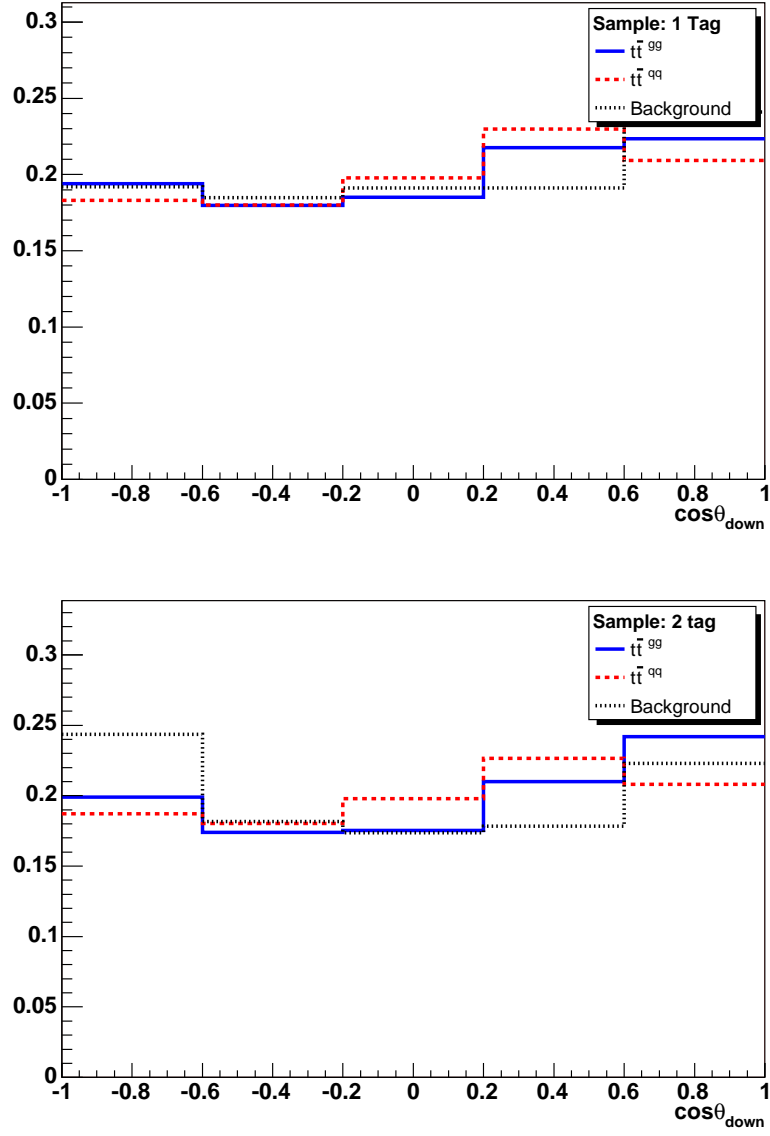


Figure 4.10: Distribution of $\cos\theta_{\text{down}}$ for $t\bar{t}^{gg}$ (blue, solid) and $t\bar{t}^{qq}$ (red, dashed) and background (black, dotted) for 1-tag (top) and ≥ 2 -tags events (bottom).

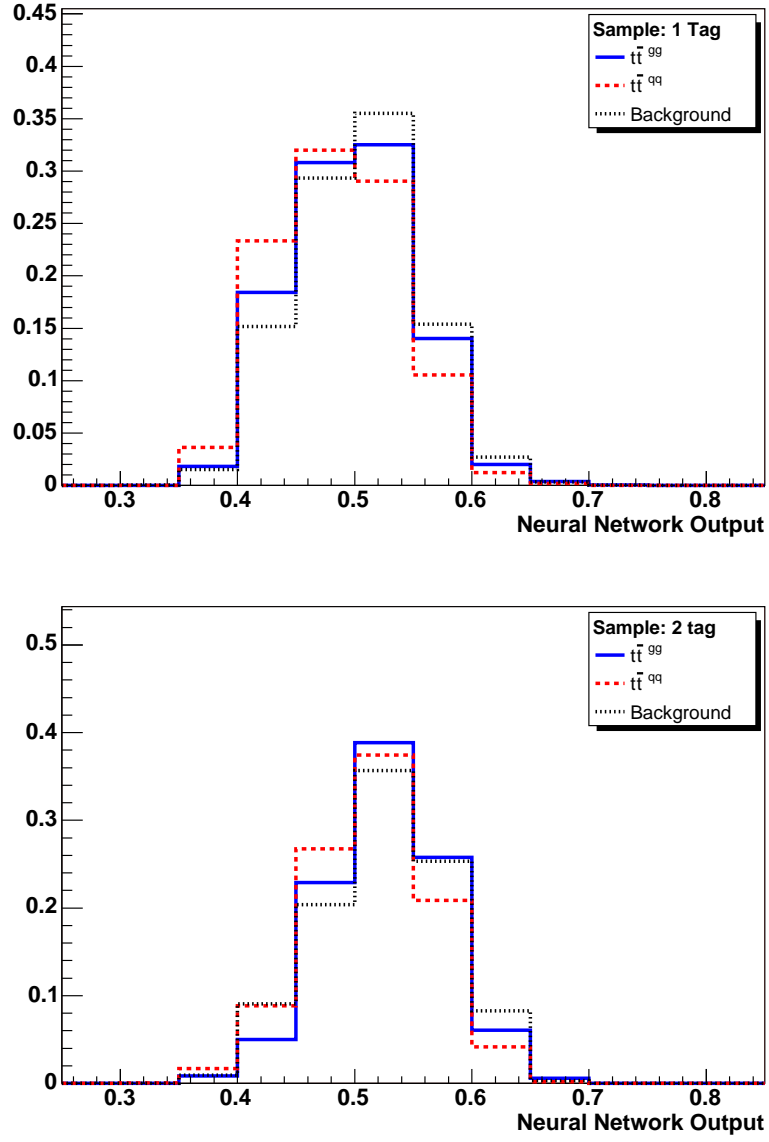


Figure 4.11: Neural Network distributions that we use as templates for 1-tag (top) and 2-tag (bottom) events for $t\bar{t}^{qq}$ (red), $t\bar{t}^{gg}$ (blue) and background (black).

likelihoods of the two exclusive samples:

$$\mathcal{L}(C_f) = \mathcal{L}^{1T}(C_f, C_s^{1T}) * \mathcal{L}^{2T}(C_f, C_s^{2T}) \quad (4.3)$$

where $\mathcal{L}^{\mathcal{N}T}(C_f)$ represent the likelihood for the subsample of events with \mathcal{N} b-tags and $C_s^{\mathcal{N}T}$, or signal fraction, is the relative fraction of $t\bar{t}$ events (both $t\bar{t}^{gg}$ and $t\bar{t}^{qq}$) to the total number of events for the given b-tag subsample.

The b-tag sub-sample likelihoods are defined as:

$$\mathcal{L}^{\mathcal{N}T}(C_f, C_s^{\mathcal{N}T}) = e^{\frac{-(C_s^{\mathcal{N}T} - \bar{C}_s^{\mathcal{N}T})^2}{2.0 * \sigma_{C_s^{\mathcal{N}T}}^2}} \prod \{C_s^{\mathcal{N}T} [C_f T_{\mathcal{N}T}^{gg} + (1 - C_f) T_{\mathcal{N}T}^{qq}] + (1 - C_s^{\mathcal{N}T}) T_{\mathcal{N}T}^{WJ}\}$$

where the product is over the events with \mathcal{N} b-tags, and $T_{\mathcal{N}T}^{gg}$, $T_{\mathcal{N}T}^{qq}$ and $T_{\mathcal{N}T}^{WJ}$ represent the template probability for the given event assuming it is gluon-produced $t\bar{t}$, quark-produced $t\bar{t}$ or $W + 4jets$ background respectively. The values of $\bar{C}_s^{\mathcal{N}T}$ are taken from Table 3.2 and $\sigma_{C_s^{\mathcal{N}T}}$ are set to 0.1.

To evaluate the likelihood we scan over values of C_f between -1 and 2. For each value of C_f the likelihood is maximized by fitting the three fractions $C_s^{\mathcal{N}T}$ using the Minuit maximization package. In a given sample the C_f value for which the likelihood is maximum is called C_f^{fit} .

Chapter 5

The Feldman-Cousins Method

The likelihood defined in Section 4.4.3 does not constrain the gluon-fusion fraction to a physically allowable range. However, the final result must have a value in closed interval from 0.0 to 1.0. We use the Feldman-Cousins Method (FC) [50] to ensure a physical result.

5.1 The Method

The Feldman-Cousins method has several properties that make it especially useful. By providing a one-to-one mapping between the fit result and the physically allowed values, FC ensures a result in the physically allowable region and gives proper coverage for all true values. It also provides a consistent way to quote either a measured value or an upper or lower limit.

FC presents a specific method called the likelihood ordering principle. In general:

$$R(\mathcal{R}_{meas}) = \frac{P(\mathcal{R}_{meas}|\mathcal{R}_{true})}{P(\mathcal{R}_{meas}|\mathcal{R}_{best})} \quad (5.1)$$

where

$$P(X|Y) = \textit{Probability of } X \textit{ given } Y \quad (5.2)$$

$$\mathcal{R}_{meas} = \textit{Measured value} \quad (5.3)$$

$$\mathcal{R}_{true} = \textit{True value} \quad (5.4)$$

$$\mathcal{R}_{best} = \textit{The most likely value.} \quad (5.5)$$

Must be in the physically allowed region.

For each value of \mathcal{R}_{true} , we find values x_1 and x_2 such that

$$R(x_1) = R(x_2) \quad (5.6)$$

and

$$\int_{x_1}^{x_2} P(x|\mathcal{R}_{true})dx = C.L. \quad (5.7)$$

where C.L. is the confidence level to be calculated.

To model the statistical resolution of our analysis, a large number of pseudo-experiments were created from the Monte Carlo described in Section 4.2. A set of pseudo-experiments is thrown for each value of C_f^{true} , ranging from 0.0 to 1.0 in steps of 0.025 (a total of 41 values).

At each step of C_f^{true} 10000 pseudo-experiments, each with 232 events (167 in the 1-tag and 65 in the ≥ 2 tag-bin) are thrown as detailed in Section 5.2. A Gaussian distribution is fit to these pseudo-experiments, and these fits are used for $P(\mathcal{R}_{meas}|\mathcal{R}_{true})$ as described above.

A typical plot produced by the FC Method is shown in Figure 5.1. The most likely value \mathcal{R}_{best} is calculated for each set of pseudo-experiments and fitted to a line, shown in Figure 5.1 as the “Best Value”. For any particular value of C_f^{fit} , the true value and its error can be read off the vertical axis. See Figure 5.1 for examples of how to correctly read the FC plot.

5.2 Pseudo-experiments

To construct the FC bands we generate a large number of *pseudo-experiments* using Monte Carlo. The throwing of pseudo-experiments is done independently for each tag bin. In a given tag bin the pseudo-experiments are thrown for a given value of C_f^{true} and C_s , and the number of events in each pseudo-experiment is fixed to the number observed in data (N_{data}) for that tag bin.

5.2.1 Acceptance

A complication is that there is a difference between the acceptance for $t\bar{t}^{gg}$ and $t\bar{t}^{q\bar{q}}$ events as shown in Table 5.1. The variable C_f^{true} represents the true fraction of $t\bar{t}^{gg}$ events with respect to the total number of generated $t\bar{t}$ events. Because the acceptances for gluon-fusion and $q\bar{q}$ -annihilation events are different, the true fraction is not the

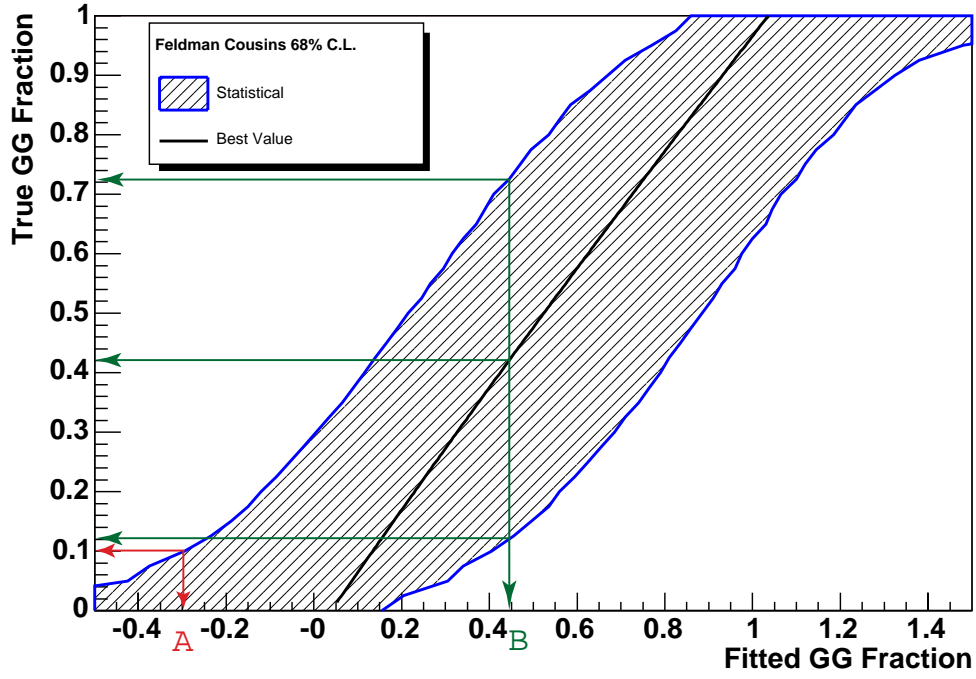


Figure 5.1: Sample Feldman-Cousins confidence band at 68% confidence level (*Statistical Error Only*): For any Fitted GG Fraction (C_f^{fit}) measured in data, the True GG Fraction (C_f^{true}) can be read off the vertical axis. Example A (red) shows a C_f^{fit} that yields a limit of < 0.1 at a 68% confidence level. Example B (green) shows a C_f^{fit} that yields a measured value of 0.42 ± 0.3 . The measured value is the value of the line “Best Value” at C_f^{fit} .

Sample	Acceptance(%)	Acceptance(%)
	1-tag	\geq 2-tag
$t\bar{t}^{gg}$	2.36 ± 0.01	1.05 ± 0.01
$t\bar{t}^{qq}$	1.83 ± 0.01	0.84 ± 0.01

Table 5.1: Acceptance for $t\bar{t}^{gg}$ and $t\bar{t}^{qq}$ events for the 1 and 2-tag samples.

fraction accepted in the reconstructed data sample (C_f^{sample}). The relation between these two is simply:

$$C_f^{sample} = \frac{C_f^{true}}{C_f^{true} + (1 - C_f^{true}) \frac{A_Q}{A_G}} \quad (5.8)$$

where A_Q and A_G are the acceptances of $t\bar{t}^{qq}$ and $t\bar{t}^{gg}$ events respectively, whose values are given in Table 5.1.

5.2.2 Generating the Pseudo-experiments

In a given pseudo-experiment the events to be used are obtained as follows. For each source-sample a random number of events, obtained by Poisson-fluctuating the nominal number of events determined in Table 5.2, is drawn from the proper source-sample. If the total sum of these selected events is less than the number of events seen in data, N_{data} , the events are discarded and the procedure repeated until the sum of these random events equals or exceeds N_{data} . If the total number exceeds N_{data} , then we further randomly select N_{data} events out of the selected events.

The events in each pseudo-experiment come from three dataset sources: $t\bar{t}^{gg}$, $t\bar{t}^{qq}$, and background events. The nominal number of events to be used from each dataset source is obtained from C_f^{sample} and C_s as shown in Table 5.2. An example of the pseudo-experiments can be seen in Figure 5.2.

For each tag bin the values of the signal fraction, C_s , are determined in Table 3.2, and the values of C_f^{sample} are obtained from C_f^{true} according to Equation 5.8 where the acceptances are taken from Table 5.1. Now with all the pseudo-experiments we construct the Feldman-Cousins bands.

Event source	Nominal number of events
$t\bar{t}^{gg}$ events	$C_f^{sample} * C_s * N_{data}$
$t\bar{t}^{qq}$ events	$(1-C_f^{sample}) * C_s * N_{data}$
background events	$(1-C_s) * N_{data}$
Total	$1.0 * N_{data}$

Table 5.2: Nominal number of events to be used for the throwing of pseudo-experiments.

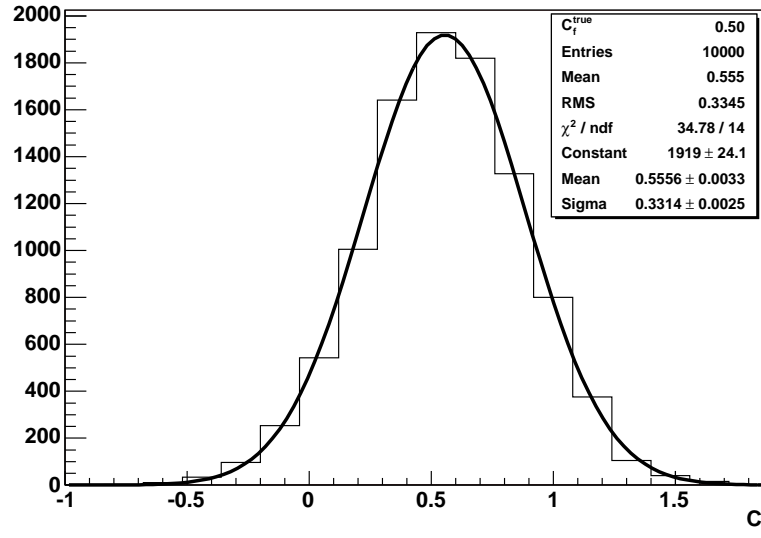


Figure 5.2: Example of a set of pseudo-experiments for $C_f^{true} = 0.50$, shown fit with a gaussian.

Chapter 6

Systematic Uncertainties

Apart from the statistical uncertainty on the measurement, which arises due to the finite size of the data sample, the systematic uncertainties associated with the measurement of C_f^{true} must also be considered. The systematic uncertainty is determined for each bin of C_f^{true} in the FC plot by constructing pseudo-experiments from signal and/or background samples affected by the systematic source under study but fit using the default method (NN templates and likelihood) described above.

For a given bin of C_f^{true} the resulting shifts in the means of pseudo-experiments distribution (δ_{sys}) are used to quantify the systematic uncertainty for each source considered. Because we are only concerned with the means of the distributions, we use 500 event and 1000 pseudo-experiments to generate the systematic distributions. To obtain a total systematic uncertainty we compare the distribution of values of C_f from the pseudo-experiments for each of the systematic samples and compare the distribution with the same for the default sample. We add these differences (taking the largest difference for each systematic source considered) in quadrature to the variances coming from the default pseudo-experiments. This broadens the distribution of C_f values from the pseudo-experiments giving the systematic variance, σ_{sys} . We then construct the new FC bands which will now contain both the statistical and systematic uncertainties. For any number, i , of systematics:

$$\delta_{sys_i} = mean_{default} - mean_{sys_i} \quad (6.1)$$

$$\sigma_{sys} = \sqrt{\sigma^2 + \delta_{sys_1}^2 + \delta_{sys_2}^2 + \dots + \delta_{sys_i}^2} \quad (6.2)$$

This technique was also used in [58]. See the example in Figure 6.1.

The following sources of systematic uncertainties are considered:

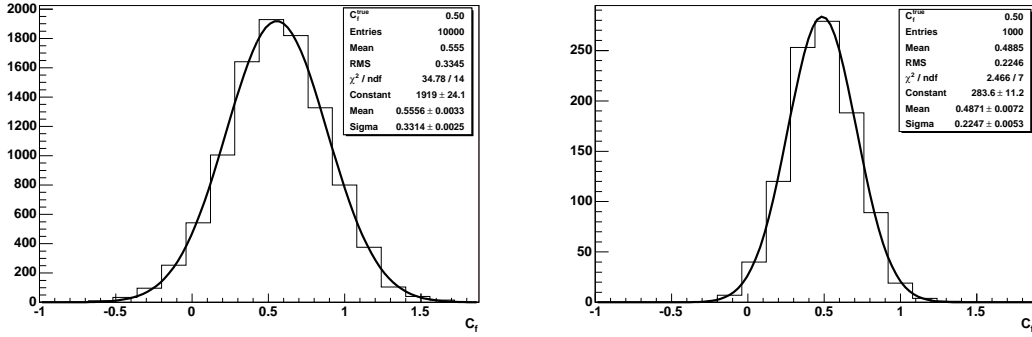


Figure 6.1: Comparison of pseudo-experiments used to derive systematic errors. The two distributions above are for $C_f^{true} = 0.50$. Right plot shows our default set of pseudo-experiments. Left plot shows one of our systematically varied sets of pseudo-experiments. If this were the only systematic, then $\delta_{sys} = 0.07$ and $\sigma_{sys} = \sqrt{0.33^2 + 0.07^2}$

- Jet Energy Scale
- Background Shape and Composition
- Initial State Radiation
- Final State Radiation
- Parton Distribution Functions
- Next to Leading Order Corrections

We do not take variations in the top mass as a systematic. Instead, we choose to present this as a result assuming $m_t = 175 \text{ GeV}/c^2$. A brief discussion of our dependence on the top mass is covered in Appendix B.

The systematics listed above are each discussed in more detail in the following sections.

6.1 Jet Energy Scale

The measured energy of the jets is corrected back to the parton as described in Section 3.2.2. However, due to hadronization and limited statistics there is an uncertainty to this correction.

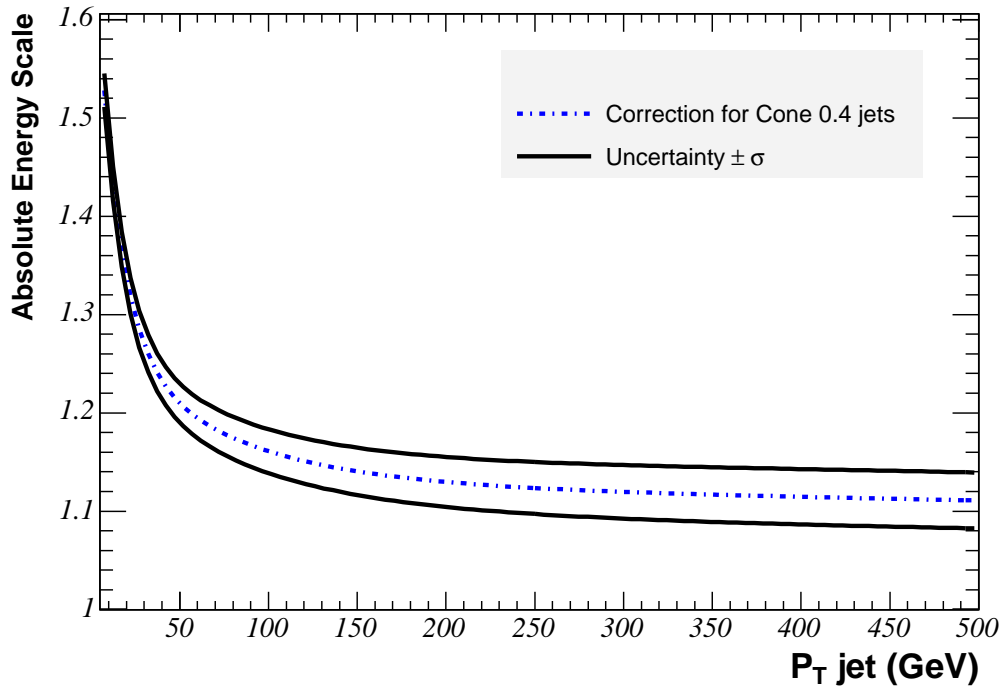


Figure 6.2: Jet energy correction and uncertainty. This plot shows the energy correction we use in this analysis as a function of transverse momentum (P_t). The “Cone 0.4 jet” refers to jet definition given in Section 3.2.2. In black you see the 1σ uncertainty on the correction that we use as the jet energy systematic [47].

We vary the Jet Energy Scale (JES) by $\pm 1\sigma$, as shown in Figure 6.2, in both the signal and background events and the variation in the $t\bar{t}^{gg}$, $t\bar{t}^{qq}$ and background templates are shown in Figure 6.3. The resulting FC curves with the $\pm 1\sigma$ JES variations are shown in Figure 6.4 and appears to result in a very small systematic uncertainty.

6.1.1 Background Shape and Composition

In this analysis it is assumed that the background is properly described by a single shape in the NN template. This shape was obtained from the background Monte Carlo events described in Section 4.2. The systematic deviations from the NN shape needs to be assessed. Such deviations can come mainly from two mechanisms:

- The different background processes that compose our background sample have different shapes and are mixed in different fractions than the real data.
- The shape obtained from MC for a given process is different than for data, for example due to Q^2 effects.

Both these effects can result in a systematic error associated with the background shape.

To address the issue of the background composition, we generated pseudo-experiments in which the combined background sample has been replaced with a sample of a single background process. For each sample the mean of the distribution of pseudo-experiments is then compared to the mean of the standard sample and the difference computed.

As discussed in Section 1.4.1 the shape of the parton distributions depends on Q^2 energy scale. We vary this when generating the background Monte Carlo to quantify the effect it has on our result. We use two samples, one where the Q^2 is increased ($Q^2 = 4m_W^2$), and one where the Q^2 is decreased ($Q^2 = m_W^2/4$).

The samples considered, and the differences in the mean of the distributions with respect to the default, for $C_f^{true} = 0.5$, are shown in Figure 6.5 and summarized in Table 6.1. We take the largest difference among all these as the systematic due to background composition and Q^2 energy scale. The final effect of the different shape and composition systematics on our Feldman-Cousins limits can be seen in Figure 6.6.

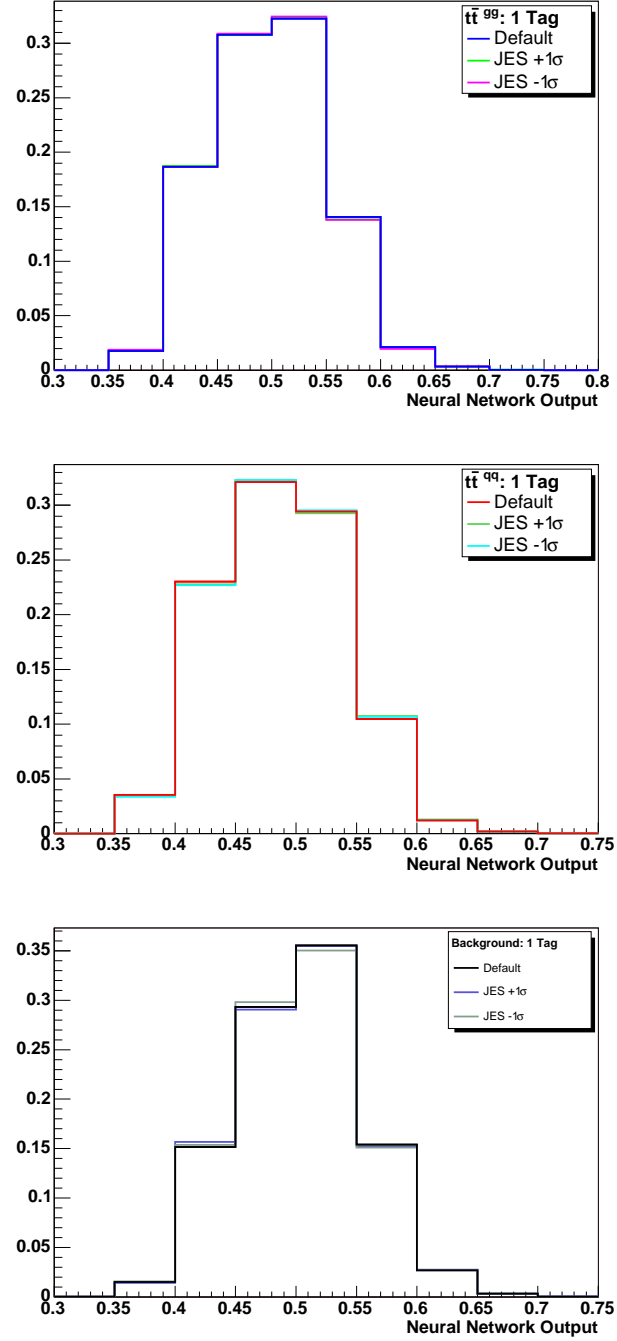


Figure 6.3: Neural Network shapes for Jet Energy Scale systematic ($\pm 1\sigma$) for $t\bar{t}^{gg}$ (top), $t\bar{t}^{qq}$ (middle), and background (bottom)

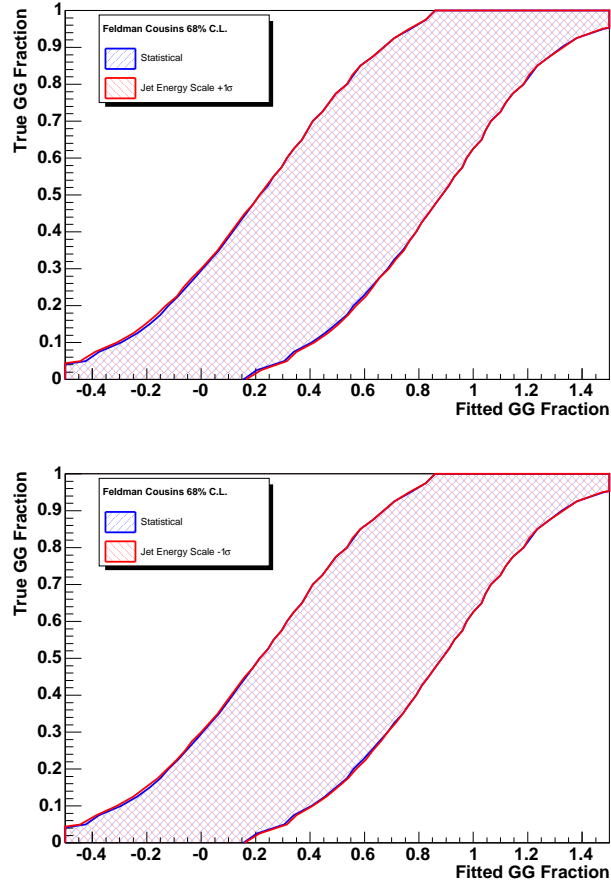


Figure 6.4: Feldman-Cousins 68% C.L. with JES systematic. The blue band shows the statistical uncertainty, with the red band showing the statistical plus systematic uncertainty. The top plot shows $+1\sigma$ JES correction, while the bottom plot shows the -1σ JES correction

Sample	δ_{sys}
$W + 4p$	0.004 ± 0.011
$Wc + 3p$	-0.079 ± 0.012
$Wb\bar{b} + 2p$	-0.001 ± 0.012
$Wc\bar{c} + 2p$	0.002 ± 0.011
$W + 4p, Q^2 = 4m_W^2$	0.067 ± 0.012
$W + 4p, Q^2 = m_W^2/4$	-0.028 ± 0.011
$Wb\bar{b} + 2p, Q^2 = 4m_W^2$	0.066 ± 0.011
$Wb\bar{b} + 2p, Q^2 = m_W^2/4$	0.073 ± 0.011
QCD	-0.154 ± 0.011
Largest difference: (QCD)	0.154 ± 0.011

Table 6.1: Example of the background systematic due to sample composition and Q^2 energy scale for $C_f^{true} = 0.5$. Similar calculations take place for each value of C_f^{true} , and for each value of C_f^{true} the largest difference (in this case QCD) is used as for the value of this systematic.

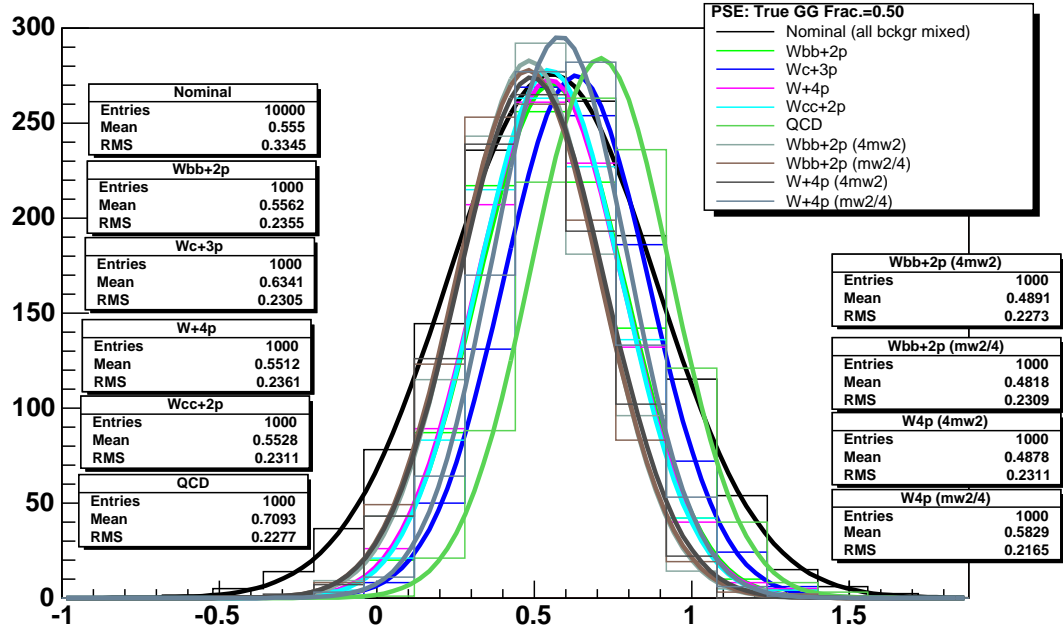


Figure 6.5: Example pseudo-experiments generated used to calculate the background systematic due to sample composition and Q^2 energy scale for $C_f^{true} = 0.5$. Similar pseudo-experiments are thrown for each value of C_f^{true} . δ_{sys} for each set is show in Table 6.1

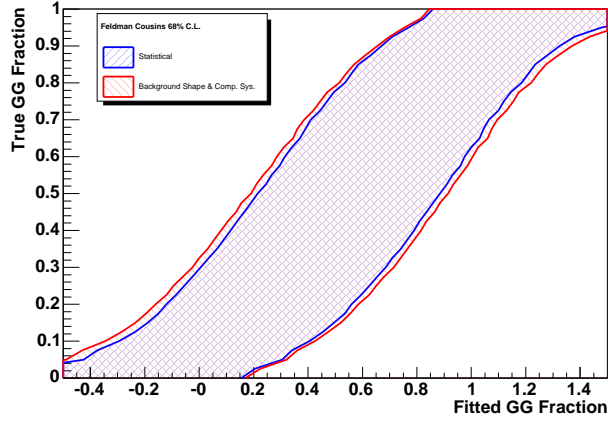


Figure 6.6: Feldman-Cousins 68% C.L. with the background shape and composition systematic uncertainty.

6.1.2 Gluon Radiation

As mentioned in Chapter 1, gluons couple to quarks as well as other gluons. This leads to the possibility of gluon radiation. For example see Figure 6.7. Now our lepton + jets channel has an extra jet that can change the kinematics of the event. The amount of initial state radiation (ISR) and final state radiation (FSR) is not well constrained. The rate of ISR can be studied in Drell-Yan events where Z decays into leptons, Figure 6.8. This process has no FSR so all the extra jets are due solely to ISR. This study has been done here [59]. Using this study, the parameters of the `Pythia` Monte Carlo generator [60] can be adjusted (or “tuned”) to match the results of the data. The variations due to the uncertainty in the above Z study are what we use to define our “more” and “less” ISR systematic.

Unlike ISR there is no way to directly study FSR. However with the help of the `Pythia` authors, analogous parameters that control FSR were adjusted in a similar fashion [61] to define our “more” and “less” FSR systematic.

Initial State Radiation

We compare the mean C_f^{true} when using a $t\bar{t}$ `Pythia` sample with more or less ISR mentioned above. We then generate pseudo-experiments for each value of C_f^{true} as before. Figures 6.10 & 6.9 show that the effect of varying the amount of ISR results

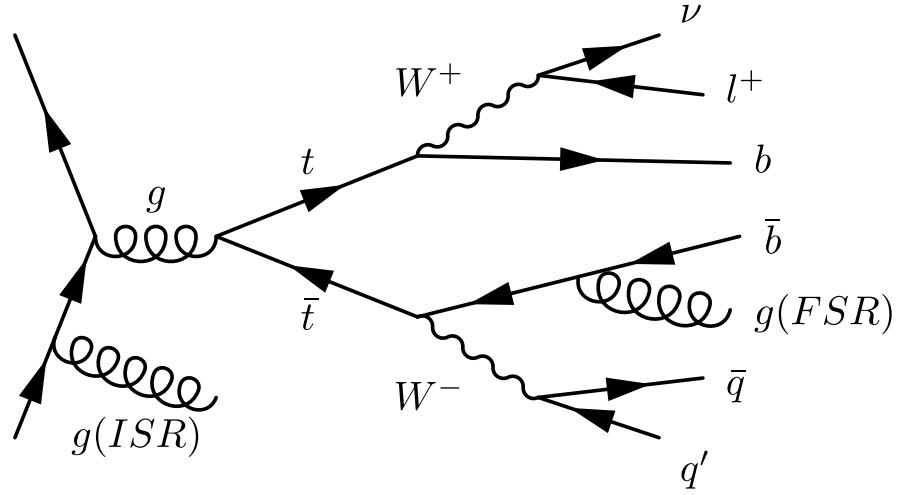


Figure 6.7: Example of a lepton + jets $t\bar{t}$ event with initial state radiation (ISR) and final state radiation (FSR).

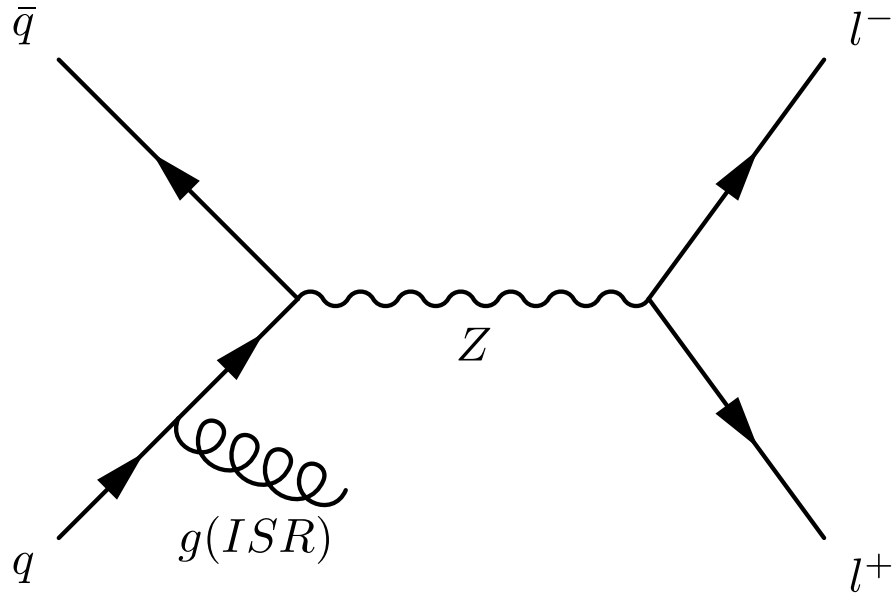


Figure 6.8: Example of a Z boson decaying to leptons with initial state radiation (ISR). Because gluons do not couple to leptons this channel has no final state (gluon) radiation.

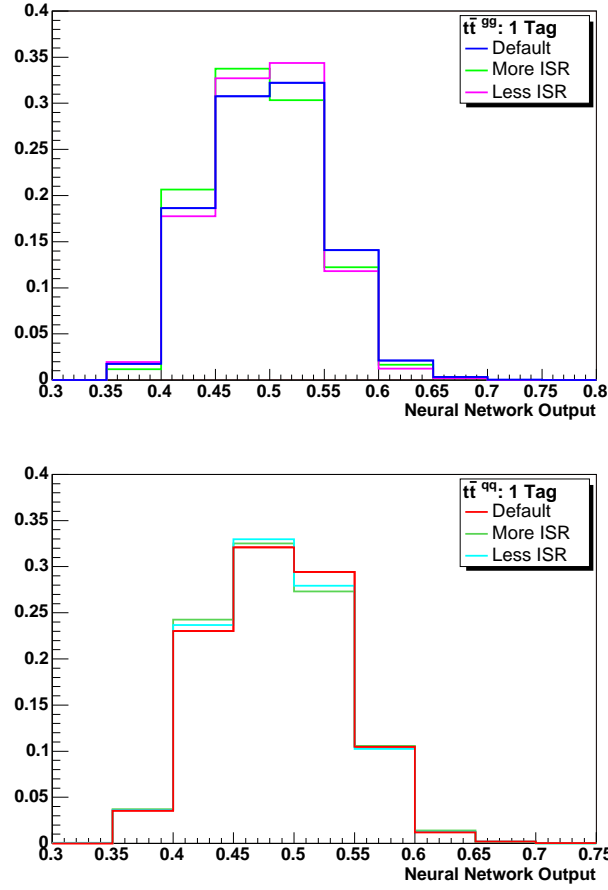


Figure 6.9: Neural Network shapes for the Initial State Radiation (ISR) systematic (more/less ISR) for $t\bar{t}^{gg}$ (top), and $t\bar{t}^{qq}$ (bottom)

in a small systematic uncertainty. We take the largest difference between these two samples as the systematic uncertainty.

Final State Radiation

Similar to what was done for the ISR systematic, we compare the mean C_f^{true} when using a $t\bar{t}$ Pythia sample with more or less FSR, for the signal events in pseudo-experiments. Figures 6.12 & 6.11 show that the effect of varying the amount of FSR results in a small systematic uncertainty. We take the largest difference between these two samples as the systematic uncertainty.

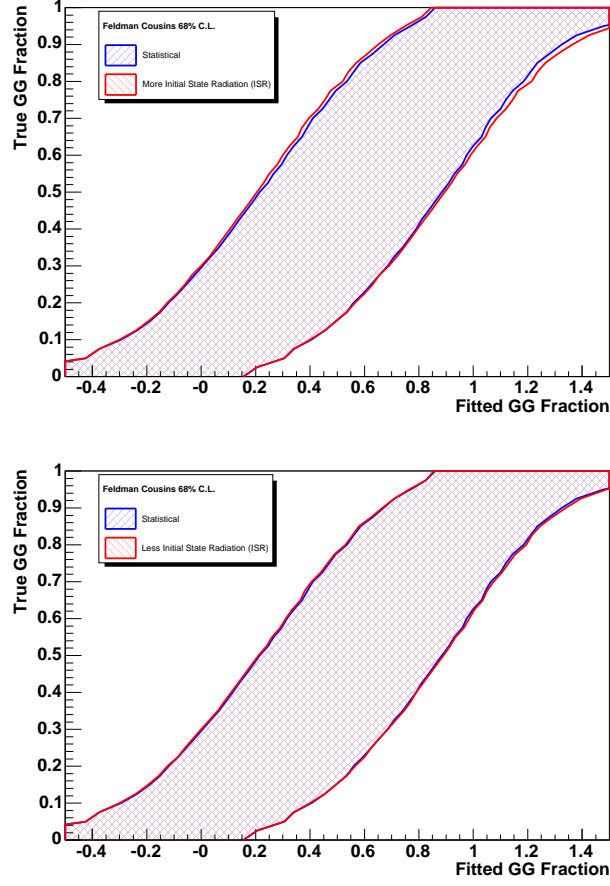


Figure 6.10: Feldman-Cousins 68% C.L. with ISR systematic. The blue band shows the statistical uncertainty, with the red band showing the statistical plus systematic uncertainty. The top plot shows FC made with $t\bar{t}$ event with more ISR, while the bottom plot shows FC made with $t\bar{t}$ event with less ISR.

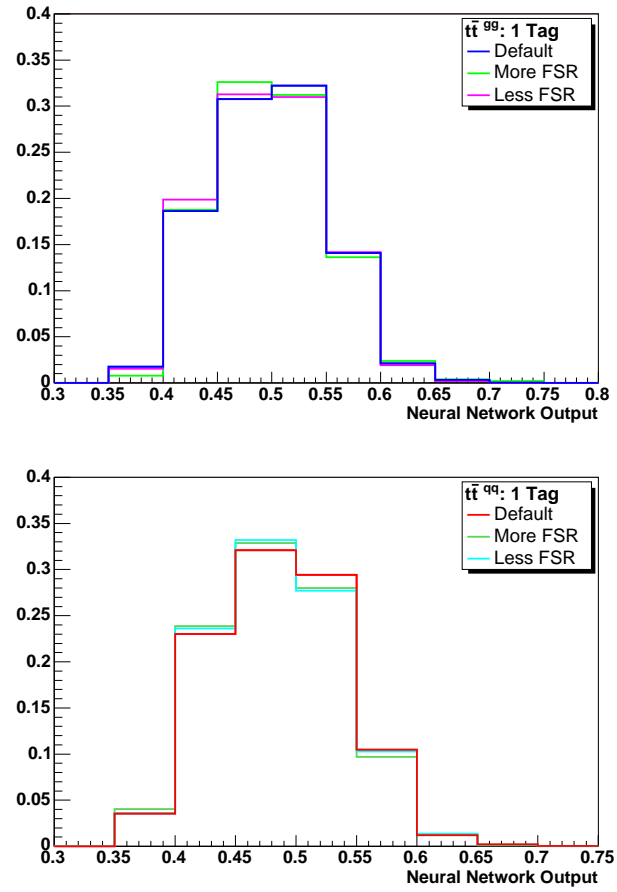


Figure 6.11: Neural Network shapes for the Final State Radiation (FSR) systematic (more/less FSR) for $t\bar{t}^{gg}$ (top) and $t\bar{t}^{qq}$ (bottom)

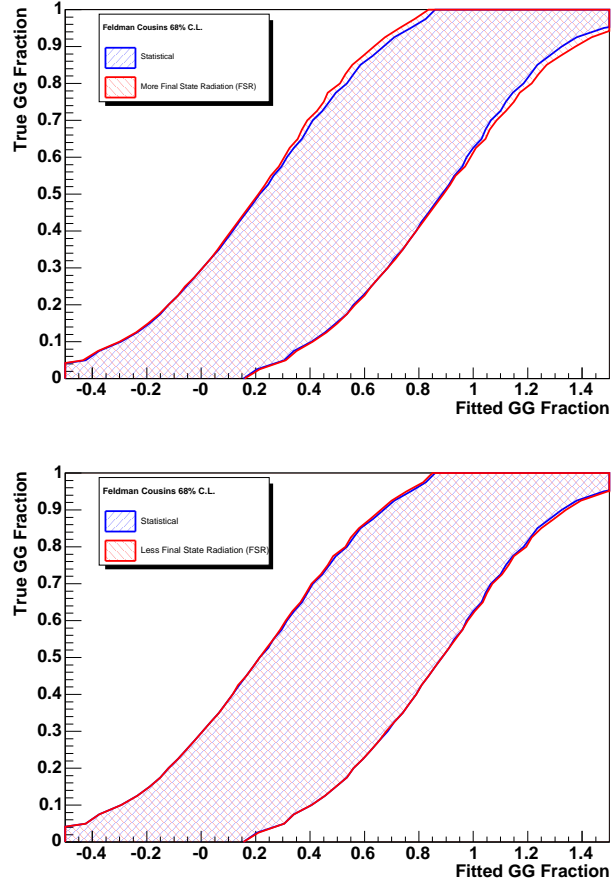


Figure 6.12: Feldman-Cousins 68% C.L. with FSR systematic. The blue band shows the statistical uncertainty, with the red band showing the statistical plus systematic uncertainty. The top plot shows FC made with $t\bar{t}$ event with more FSR, while the bottom plot shows FC made with $t\bar{t}$ event with less FSR.

6.1.3 Parton Distribution Functions

The effect of PDF's is studied using the re-weighting technique [2]. The PDF's we used are:

- CTEQ5L [2] - the default PDF. The relative weight for every event is 1.
- CTEQ6M [2] - NLO PDF plus the 40 varying error PDF's, 20 “up” and 20 “down” eigenvectors.
- MRST72 [62] - Leading order PDF. If a difference relative to the default PDF is found it should be taken as a systematic.
- MRST75 [62] - Same as the previous, but using a different value of α_s , corresponding to $\Lambda_{QCD} = 300 \text{ MeV}$ vs. $\Lambda_{QCD} = 228 \text{ MeV}$ for MRST72. The difference between the two PDF's is taken as a systematic.

Figure 6.13 shows the $t\bar{t}^{gg}$ and $t\bar{t}^{q\bar{q}}$ shapes for the various PDF's described above. We observe that the effect of the PDF's is very small. The one eigenvector that has a small effect is CTEQ6M +38. We look at this extreme case and the resulting FC curve confirms that the PDF uncertainties result in a negligible systematic uncertainty on C_f^{true} .

6.1.4 Next to Leading Order Corrections

To see if we are sensitive to next to leading order (NLO) corrections to the top production mechanism, we generated a sample of Monte Carlo with MC@NLO [63, 64]. This sample has NLO producing diagrams but lacks spin correlations between top and anti-top. We find the analysis is sensitive to NLO effects. Figure 6.14 shows the effect of this systematic on the FC curve. The difference is larger for low values of C_f^{true} , suggesting that NLO effects are more pronounced for $q\bar{q}$ -annihilation than for gluon-fusion $t\bar{t}$ events. The differences are included as a part of the systematic error.

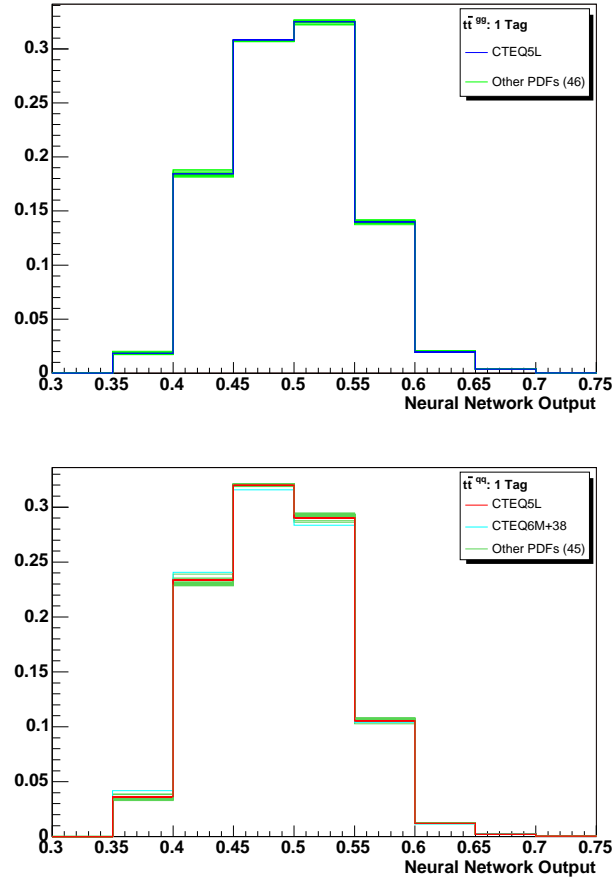


Figure 6.13: Neural Network shapes for the parton distribution function (PDF) systematic for $t\bar{t}^{gg}$ (top) and $t\bar{t}^{qq}$ (bottom). All 46 PDF's are included, they are just very close together.

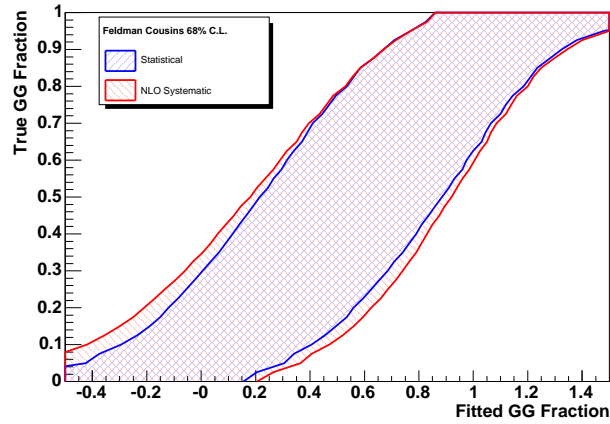


Figure 6.14: Feldman-Cousins 68% C.L. with next to leading order (NLO) systematic. The blue band shows the statistical uncertainty and the red band showing the statistical plus systematic uncertainty.

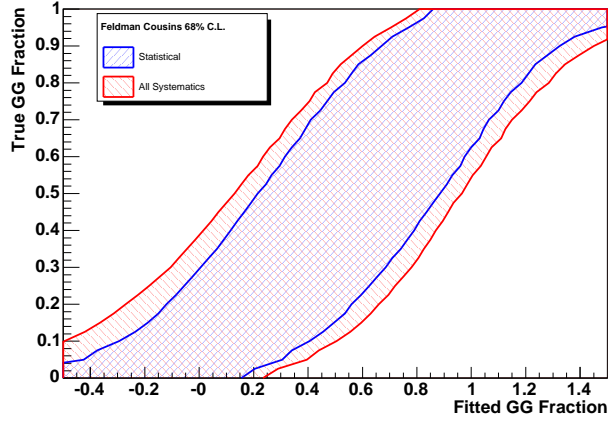


Figure 6.15: Feldman-Cousin plot at 68% C.L. Statistical error shown in blue. Statistical plus full systematic error shown in red.

Systematic	$C_f^{true}=0.0$	$C_f^{true}=0.5$	$C_f^{true}=1.0$
JES	0.118	0.042	0.025
ISR	0.017	0.106	0.153
FSR	0.098	0.060	0.184
Bkg Shape	0.151	0.155	0.151
PDF	0.115	0.034	0.028
NLO	0.308	0.159	0.023

Table 6.2: Overview of Systematics: The contribution (δ_{sys}) for each systematic source for select values of C_f^{true} .

6.1.5 Summary of Systematic Uncertainties

We use the largest difference obtained due to each source of systematic uncertainty and the total systematic uncertainty is taken to be their quadrature sum as described above. Figure 6.15 shows the resulting FC bands with full statistical and systematic uncertainties. Table 6.2 shows the contribution of each systematic source for selected values of C_f^{true} .

Chapter 7

Results

7.1 Results

This is a blind analysis, so the procedure and sources of systematic error are investigated before fitting the actual data. This procedure prevents bias. Now looking at the data, when we compute the likelihood for the 232 data events (Chapter 3) we obtained the result shown in Figure 7.1. The minimum of the negative log likelihood is obtained at:

$$C_f^{fit} = -0.075.$$

At 68% confidence level this corresponds, from Figure 7.2, to a purely statistical result of $C_f^{true} < 0.23$, and to a result of $C_f^{true} < 0.33$ when systematic uncertainties are taken into account. The fitted NN distributions are shown in Figure 7.4.

Figure 7.3 shows the limits, including systematic uncertainties, for bands of 68% and 95% confidence level. At the 95% confidence level we find $C_f^{true} < 0.61$.

As a cross check we show the fitted fractions for all the input variables of the NN, in Appendix C. The agreement is very good for each variable.

7.2 Conclusions

We present a measurement of the relative fraction of $t\bar{t}$ events produced via gluon-fusion to the total number of $t\bar{t}$ events using a template method based on Neural Networks probabilities. Using a total integrated luminosity of 955 pb^{-1} we find $C_f^{true} < 0.33$ at 68% confidence level. This is consistent with what was predicted in theory. The result is also consistent with the other CDF analysis described in Section 1.5. That result finds the fraction of gluon-fusion produced event is $0.07 \pm 0.14(stat) \pm 0.07(syst)$. As pointed out previously that result is somewhat indirect and subject to interpretation.

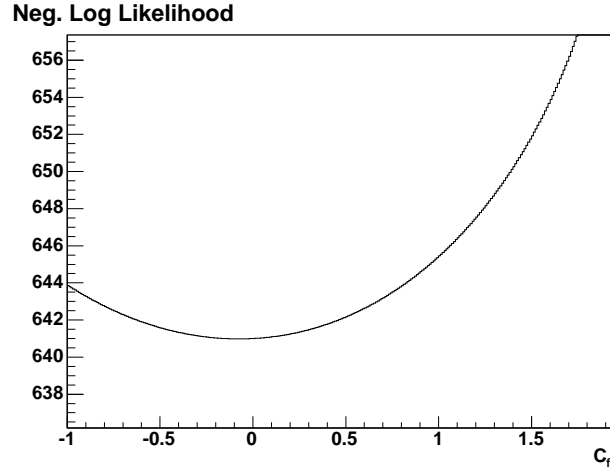


Figure 7.1: Negative log likelihood for the data, using the likelihood function described in Section 4.4.3.

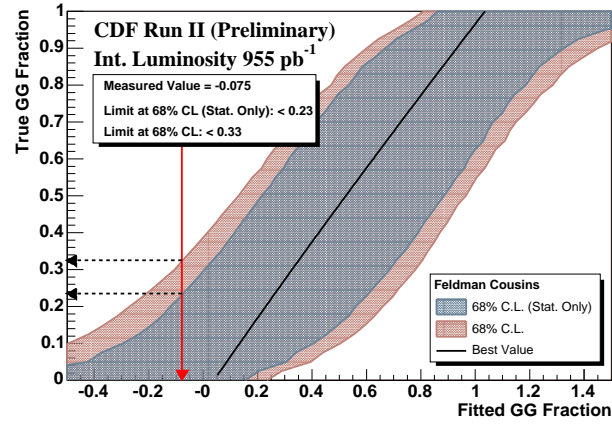


Figure 7.2: FC with all systematic errors compared to FC with only statistical error for a confidence level of 68%.

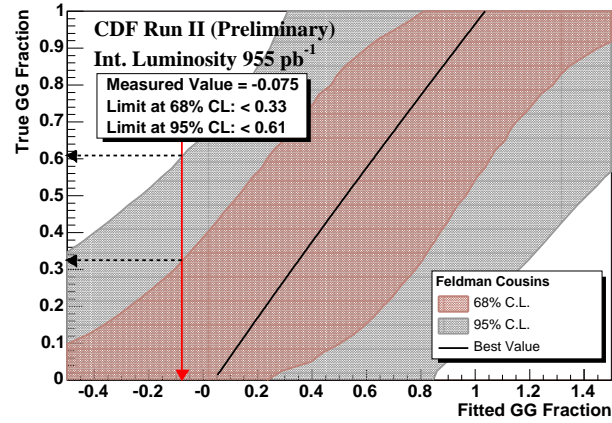


Figure 7.3: Final systematic error from all sources using the Feldman-Cousins method.

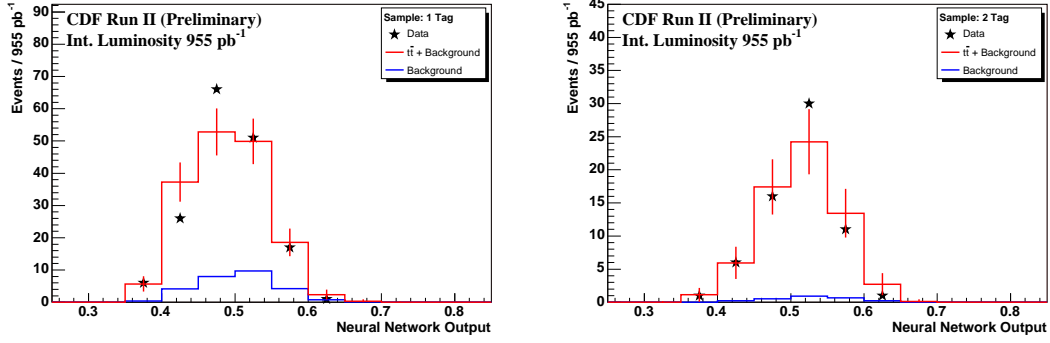


Figure 7.4: Neural network templates fit to the Data (Left 1 tag, Right 2 tag).

As discussed in Section 1.4.1, the rate of gluon-fusion events at the LHC is expected to be approximately 50 times greater than at the Tevatron. However, because the parton distribution functions depend on the interaction energy, Q^2 , we can only extrapolate our current data to these higher values of Q^2 . Because the Tevatron is at the energy frontier, we can provide data at the higher values of Q^2 that have yet to be included in the PDF's. Though given the limited top quark statistics at this time, the precision of our measurement is only enough to show consistency. However this analysis conclusively demonstrates that we can successfully discriminate the production process of $t\bar{t}$.

Appendix A

Overview of Neural Networks

This is a brief overview of Neural Networks (NN). For more information see here [56] and here [65].

All particle physics is based on our ability to classify events into different types. This is usually done by selecting one or more variables x_i that are measurable properties and that exhibit some separation between the two categories, in our case $t\bar{t}^{gg}$ and $t\bar{t}^{qq}$. In general the x_i are correlated, so simply cutting on each x_i ignores information that could improve the selection. We want a method that combines all of the information contained in the x_i into a smaller set of variables y_k that we can use to define a signal region. Neural networks are designed to do this distillation.

Neural networks can be constructed using a wide variety of architectures and learning algorithms, the type we use in this analysis is a “feed-forward network trained using back-propagation”.

Figure A.1 shows a typical feed-forward network architecture. A feed-forward network is evaluated layer by layer, so that the input variables x_i are propagated through the network to the output layer. The input nodes normalize the variables so that the values of x_i are of a similar scale. The value of a node h_j in the first hidden layer is then given by the function $A(z)$:

$$h_j = A(\omega_{0j} + \sum_i \omega_{ij}x_i) \quad (\text{A.1})$$

where ω_{ij} is the weight assigned to each link between the input and hidden layers, ω_{0j} is the threshold for each hidden node h_j , and $A(z)$ is the node activation function, given by a sigmoid function:

$$A(z) = \frac{1}{1 + e^{-z}} \quad (\text{A.2})$$

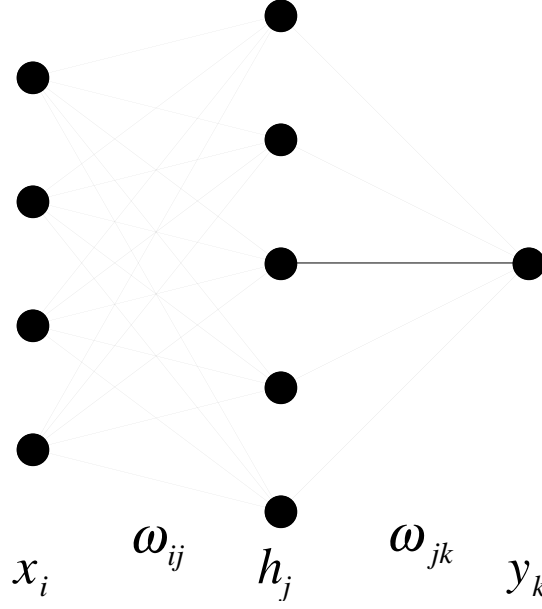


Figure A.1: Generic diagram of a typical feed-forward neural network. Input on the left and output on the right.

If there are more hidden layers they are evaluated in turn, replacing the input node values x_i with the appropriate h_j values from the previous layer. The output layer values y_k are given by:

$$y_k = \omega_{0k} + \sum_j \omega_{jk} h_j \quad (\text{A.3})$$

where ω_{jk} is the weight for a link between the last hidden and output layer, and ω_{0k} is an output node threshold. The ω 's and ω_0 's, collectively denoted as a vector $\vec{\omega}$, are free parameters of the network, which are determined by training against test samples.

The training samples are collections of items for which both the input patterns x_i and the desired network outputs t_k are specified. For example we set t_k to 1 for $t\bar{t}^{gg}$ and 0 for $t\bar{t}^{qq}$. These samples are drawn from our Monte Carlo simulation, which allows us to know of the true type of each event. The training procedure involves minimization of an error measure, a mean square error:

$$E = \frac{1}{2N_p} \sum_p \sum_k (y_k^{(p)} - t_k^{(p)})^2 \quad (\text{A.4})$$

where N_p is the number of patterns (items) in the training set, and the (p) denotes the observed and target network outputs for a particular input pattern $x_i^{(p)}$. Training is

therefore analogous to performing a χ^2 fit for the parameters $\vec{\omega}$.

Many specialized techniques have been developed to minimize $E(\vec{\omega})$. The method used in this analysis was developed by Broyden, Fletcher, Goldfarb, and Shanno (BFGS) [66, 67, 68, 69]. Once $E(\vec{\omega})$ is minimized the NN can be used as a *blackbox* algorithm to distinguish signal from background.

For this analysis, we use the `TMultilayerPerceptron` [56] class of the `ROOT` analysis package [57]. The structure of the NN can be found in Section 4.4.1 and a description of the Monte Carlo used for training can be found in Section 4.2.

Appendix B

Top Mass Dependence

The limits quoted in the result Section 7.1 were obtained assuming a top mass of 175 GeV. The FC bands of Figure 7.2 for example were obtained under that assumption. FC bands obtained under different top mass assumptions are shown in Figure B.1 and Figure B.2 for masses of 170 and 180 GeV respectively.

For a given data result of C_f^{fit} , the limits will change depending on what FC curves are used to read the limits from. If the data provides low values of C_f^{fit} then we see that Figure B.1 will give a stronger constraint than say, Figure 7.2 or Figure B.2. On the other hand, if the values of C_f^{fit} were high, figure 7.2 will give stronger constraints for values of C_f^{fit} around one.

In our particular case $C_f^{fit} = -0.075$, and masses of 170 and 180 give constraints of $C_f^{true} < 0.11$ and $C_f^{true} < 0.18$ respectively, which are stronger than our quoted value of $C_f^{true} < 0.23$ (systematic not included in any of these three numbers). This is not surprising since part of our machinery uses the kinematic fitter with a top mass constrained at 175 GeV/ c^2 , and other values of the top mass yield FC curves that move in the same direction.

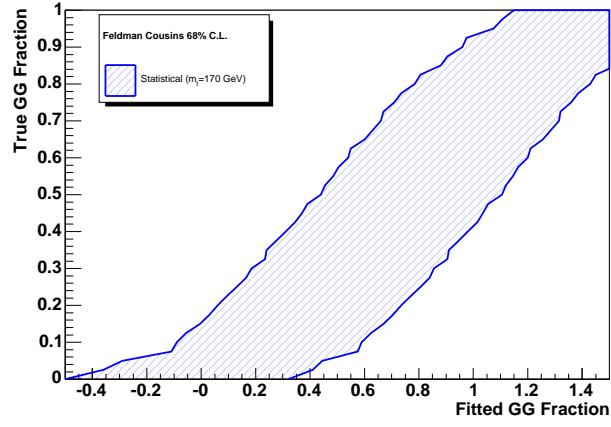


Figure B.1: FC for $m_t = 170$ GeV with statistical error only.

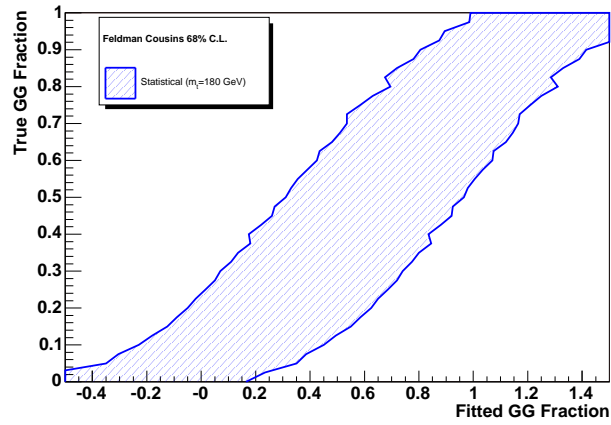


Figure B.2: FC for $m_t = 180$ GeV with statistical error only.

Appendix C

Neural Network Variables in Data

All the variable that go into the neural network can be seen below with the appropriate fitted fractions.

- Neural Network: Figure C.1
- β : the top quark velocity relative to c . Figure C.2
- $\cos \theta^*$: the angle between the top quark and the right incoming parton. Figure C.3
- $\cos \theta_{Wlep}$: angle between leptonically decaying W in the off-diagonal basis. Figure C.4
- $\cos \theta_{lep}$: angle between lepton in the off-diagonal basis. Figure C.5
- $\cos \theta_\nu$: angle between neutrino in the off-diagonal basis. Figure C.6
- $\cos \theta_{Whad}$: angle between hadronically decaying W in the off-diagonal basis. Figure C.7
- $\cos \theta_{up}$: angle between up quark in the off-diagonal basis. Figure C.8
- $\cos \theta_{down}$: angle between down quark in the off-diagonal basis. Figure C.9

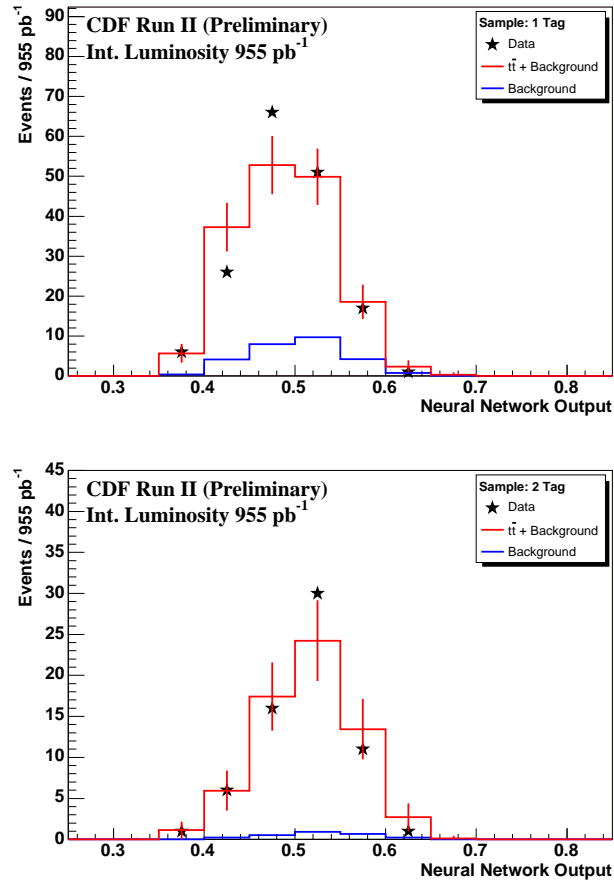


Figure C.1: Neural network templates fit to the Data (top 1 tag, bottom 2 tag).

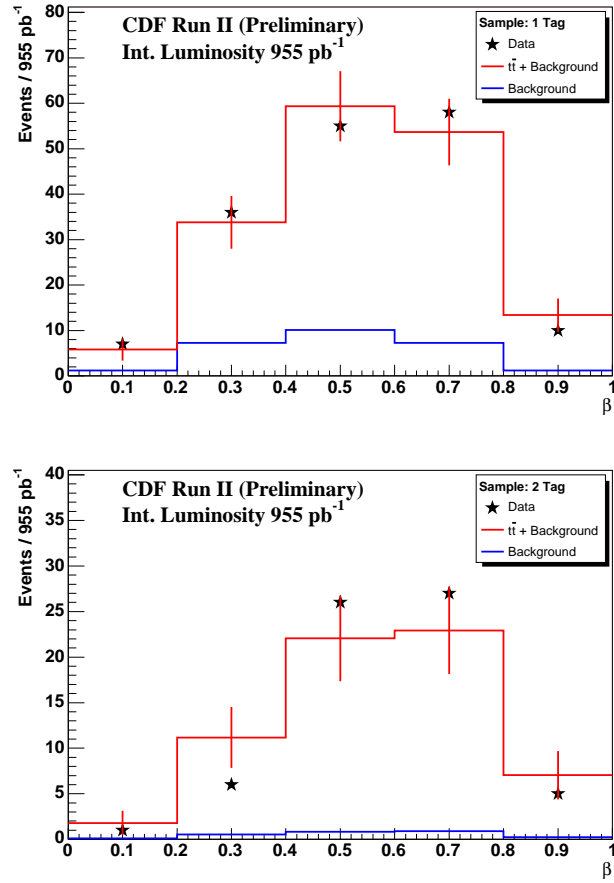


Figure C.2: β fractions set to the neural network fit to the Data (top 1 tag, bottom 2 tag).

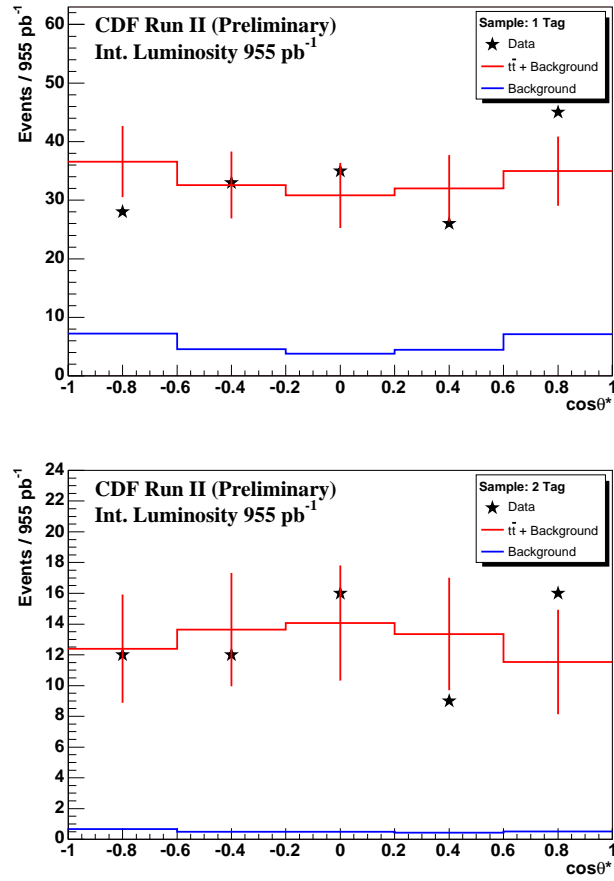


Figure C.3: $\cos \theta^*$ fractions set to the neural network fit to the Data (top 1 tag, bottom 2 tag).

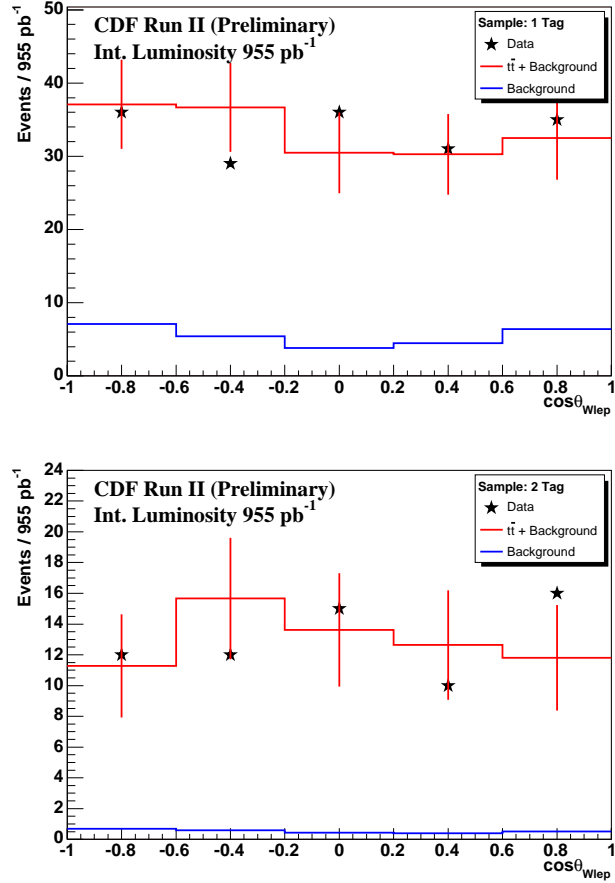


Figure C.4: $\cos\theta_{Wlep}$ fractions set to the neural network fit to the Data (top 1 tag, bottom 2 tag).

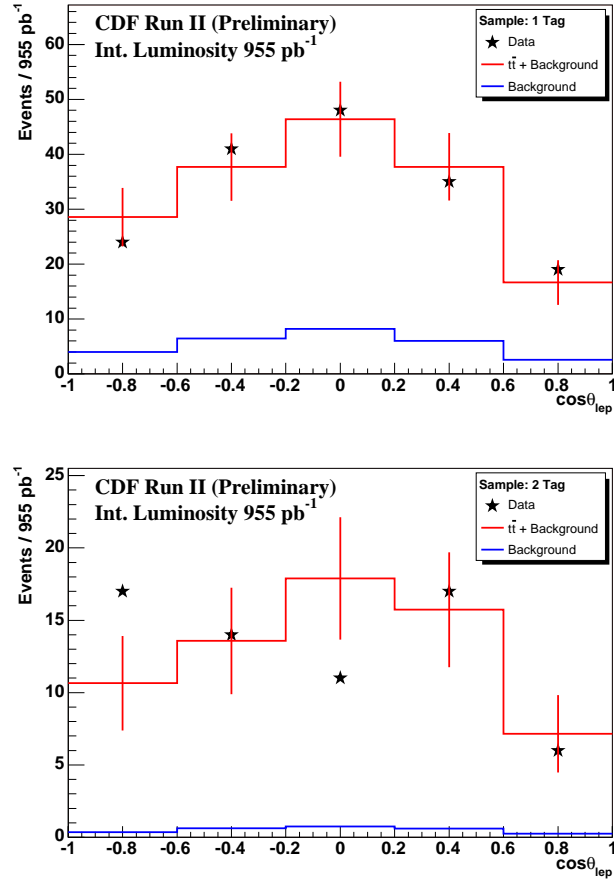


Figure C.5: $\cos\theta_{lep}$ fractions set to the neural network fit to the Data (top 1 tag, bottom 2 tag).

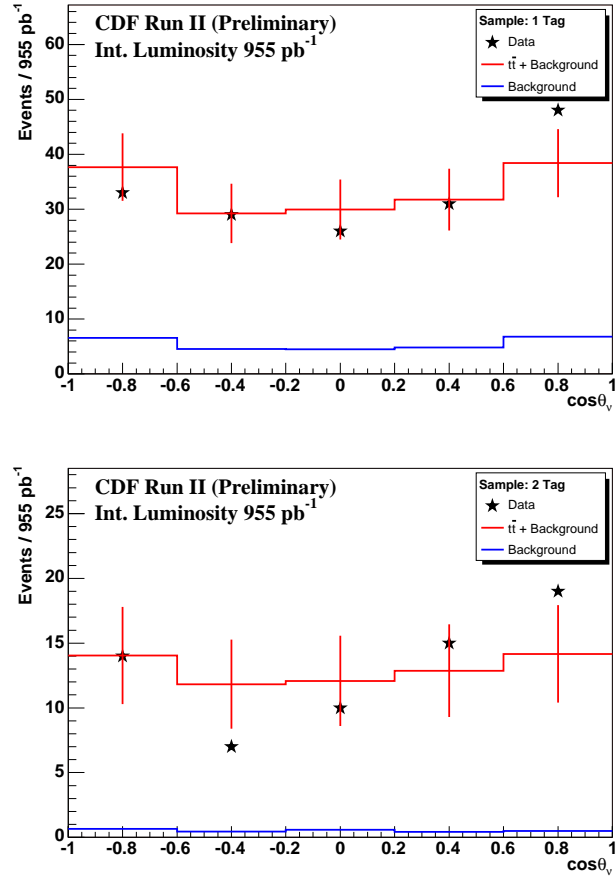


Figure C.6: $\cos\theta_\nu$ fractions set to the neural network fit to the Data (top 1 tag, bottom 2 tag).

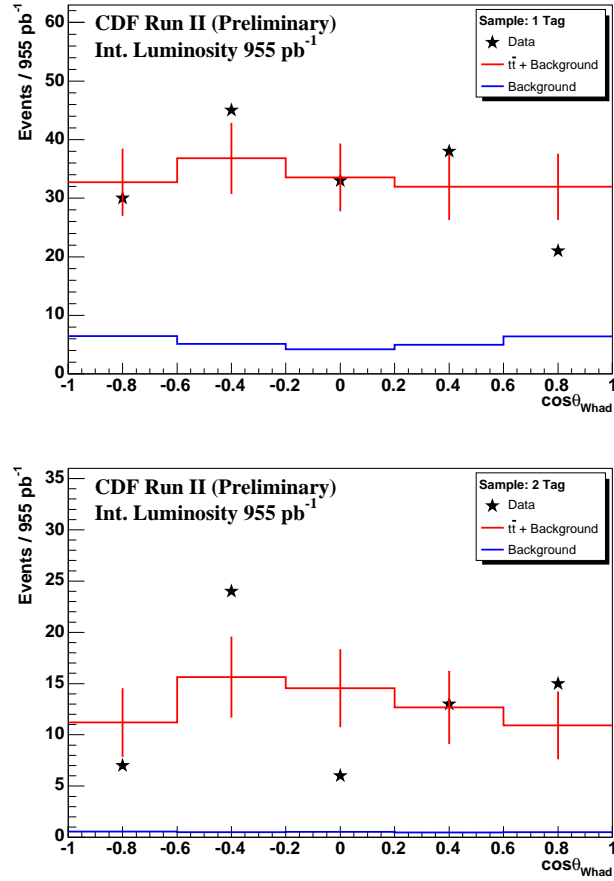


Figure C.7: $\cos\theta_{Whad}$ fractions set to the neural network fit to the Data (top 1 tag, bottom 2 tag).

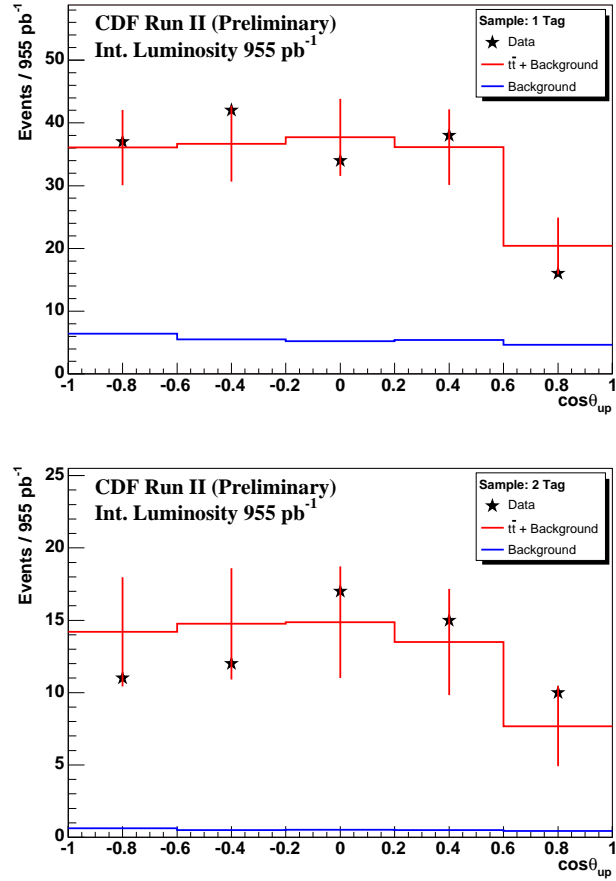


Figure C.8: $\cos\theta_{up}$ fractions set to the neural network fit to the Data (top 1 tag, bottom 2 tag).

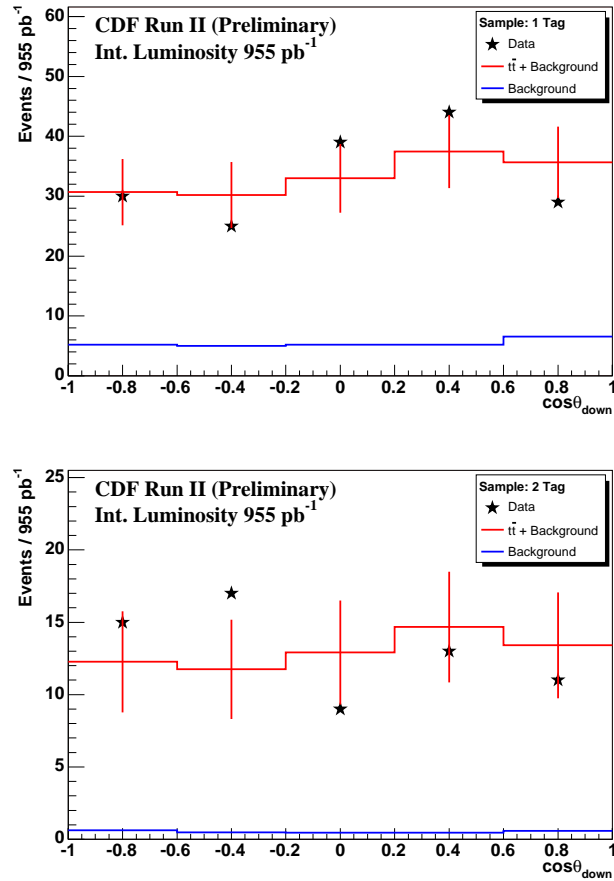


Figure C.9: $\cos\theta_{down}$ fractions set to the neural network fit to the Data (top 1 tag, bottom 2 tag).

References

- [1] **CDF** Collaboration, “Search for electroweak single-top-quark production using neural networks with 955 pb^{-1} of CDF II data.,” **CDF/8677**.
- [2] J. Pumplin *et al.*, “New generation of parton distributions with uncertainties from global qcd analysis,” *JHEP* **07** (2002) 012, **hep-ph/0201195**.
- [3] J. H. Kuhn, “Theory of top quark production and decay,” **hep-ph/9707321**.
- [4] **UA1** Collaboration, G. Arnison *et al.*, “Experimental observation of isolated large transverse energy electrons with associated missing energy at $\sqrt{s} = 540\text{ GeV}$,” *Phys. Lett.* **B122** (1983) 103–116.
- [5] **UA1** Collaboration, G. Arnison *et al.*, “Experimental observation of lepton pairs of invariant mass around $95\text{ GeV}/c^2$ at the CERN SPS collider,” *Phys. Lett.* **B126** (1983) 398–410.
- [6] F. Abe *et al.*, “Observation of top quark production in $p\bar{p}$ collisions with the Collider Detector at Fermilab,” *Phys. Rev. Lett.* **74** (Apr, 1995) 2626–2631.
- [7] S. Abachi *et al.*, “Observation of the top quark,” *Phys. Rev. Lett.* **74** (Apr, 1995) 2632–2637.
- [8] D. J. Gross and F. Wilczek, “Asymptotically free gauge theories,” *Phys. Rev. D* **8** (Nov, 1973) 3633–3652.
- [9] H. D. Politzer, “Asymptotic freedom: An approach to strong interactions,” *Phys. Rept.* **14** (1974) 129–180.
- [10] S. L. Glashow, “Partial symmetries of weak interactions,” *Nucl. Phys.* **22** (1961) 579–588.
- [11] A. Salam and J. C. Ward, “Electromagnetic and weak interactions,” *Phys. Lett.* **13** (1964) 168–171.
- [12] S. Weinberg, “A model of leptons,” *Phys. Rev. Lett.* **19** (1967) 1264–1266.
- [13] P. W. Higgs, “Broken symmetries, massless particles and gauge fields,” *Phys. Lett.* **12** (1964) 132–133.
- [14] P. W. Higgs, “Broken symmetries and the masses of gauge bosons,” *Phys. Rev. Lett.* **13** (1964) 508–509.
- [15] **CDF** Collaboration, T. Aaltonen *et al.*, “First measurement of the W boson mass in Run II of the Tevatron,” **arXiv:0707.0085 [hep-ex]**.

- [16] **CDF Collaboration**, “A combination of CDF and D0 results on the mass of the top quark,” `hep-ex/0703034`.
- [17] **LEP Working Group for Higgs boson searches Collaboration**, R. Barate *et al.*, “Search for the standard model Higgs boson at LEP,” *Phys. Lett.* **B565** (2003) 61–75, `hep-ex/0306033`.
- [18] **D0 and CDF Collaboration**, G. Bernardi *et al.*, “Combined D0 and CDF upper limits on standard model Higgs boson production,” `hep-ex/0612044`.
- [19] M. Kobayashi and T. Maskawa, “CP violation in the renormalizable theory of weak interaction,” *Prog. Theor. Phys.* **49** (1973) 652–657.
- [20] M. Jezabek and J. H. Kuhn, “QCD corrections to semileptonic decays of heavy quarks,” *Nucl. Phys.* **B314** (1989) 1.
- [21] M. Glück, J. F. Owens, and E. Reya, “Gluon contribution to hadronic j/ψ production,” *Phys. Rev. D* **17** (May, 1978) 2324–2331.
- [22] B. L. Combridge, “Associated production of heavy flavor states in pp and $\bar{p}p$ interactions: Some QCD estimates,” *Nucl. Phys.* **B151** (1979) 429.
- [23] J. D. Bjorken, “Asymptotic sum rules at infinite momentum,” *Phys. Rev.* **179** (Mar, 1969) 1547–1553.
- [24] H. Abramowicz *et al.*, “Neutrino and anti-neutrinos charged current inclusive scattering in iron in the energy range $20 \text{ GeV} < \text{neutrino energy} < 300 \text{ GeV}$,” *Z. Phys.* **C17** (1983) 283.
- [25] M. Cacciari, S. Frixione, M. L. Mangano, P. Nason, and G. Ridolfi, “The t anti- t cross-section at 1.8 TeV and 1.96 TeV: A study of the systematics due to parton densities and scale dependence,” *JHEP* **04** (2004) 068, `hep-ph/0303085`.
- [26] N. Kidonakis and R. Vogt, “Next-to-next-to-leading order soft-gluon corrections in top quark hadroproduction,” *Phys. Rev. D* **68** (Dec, 2003) 114014.
- [27] **CDF Collaboration** Collaboration, “First measurement of $\frac{\sigma(gg \rightarrow t\bar{t})}{\sigma(p\bar{p} \rightarrow t\bar{t})}$,” CDF/8724.
- [28] Fermilab Beams Division, “Fermilab Cockcroft-Walton.”
http://www.fnal.gov/pub/news04/update_archive/update_9-10.html.
- [29] Fermilab Beams Division, “Fermilab Linac.”
http://www.fnal.gov/pub/news04/update_archive/update_10-1.html.
- [30] Fermilab Beams Division, “Fermilab Booster.”
http://www.fnal.gov/pub/news04/update_archive/update_10-15.html.
- [31] Fermilab Beams Division, “Main Injector Design Report.”
http://www-fmi.fnal.gov/fmiinternal/MI_Technical_Design/index.html.
- [32] Fermilab Beams Division, “The Antiproton Source Rookie Book.”
http://www-bdnew.fnal.gov/pbar/documents/PBAR_Rookie_Book.PDF.

- [33] Fermilab Beams Division, “Recycler Design Report.”
<http://lss.fnal.gov/archive/1997/tm/TM-1991.html>.
- [34] **Electron Cooling** Collaboration, S. Nagaitsev *et al.*, “Antiproton cooling in the fermilab recycler ring,” *AIP Conf. Proc.* **821** (2006) 39–47.
- [35] Fermilab Beams Division, “Run II Handbook.”
http://www-bdnew.fnal.gov/pbar/run2b/Documents/RunII_handbook.pdf.
- [36] **On behalf of the CDF** Collaboration, C. S. Hill, “Operational experience and performance of the CDF II silicon detector,” *Nucl. Instrum. Meth.* **A530** (2004) 1–6.
- [37] **CDF** Collaboration, A. Sill, “CDF Run II silicon tracking projects,” *Nucl. Instrum. Meth.* **A447** (2000) 1–8.
- [38] **CDF** Collaboration, A. A. Affolder *et al.*, “Intermediate silicon layers detector for the CDF experiment,” *Nucl. Instrum. Meth.* **A453** (2000) 84–88.
- [39] **CDF** Collaboration, A. A. Affolder *et al.*, “CDF central outer tracker,” *Nucl. Instrum. Meth.* **A526** (2004) 249–299.
- [40] **CDF II** Collaboration, R. Blair *et al.*, “The CDF II detector: Technical design report,” .FERMILAB-PUB-96-390-E.
- [41] S. Kuhlmann *et al.*, “The CDF calorimeter upgrade for Run IIB,” *Nucl. Instrum. Meth.* **A518** (2004) 39–41, [physics/0310155](#).
- [42] **CDF** Collaboration, S. Lami, “The CDF MiniPlug calorimeters,” *Nucl. Instrum. Meth.* **A496** (2003) 333–346, [hep-ex/0207017](#).
- [43] **CDF** Collaboration, D. Acosta *et al.*, “Measurement of the J/ψ meson and b –hadron production cross sections in $p\bar{p}$ collisions at $\sqrt{s} = 1960$ GeV,” *Phys. Rev.* **D71** (2005) 032001, [hep-ex/0412071](#).
- [44] R. Downing *et al.*, “Track extrapolation and distribution for the CDF II trigger system,” *Nucl. Instrum. Meth.* **A570** (2007) 36–50, [physics/0606247](#).
- [45] **CDF** Collaboration, D. Acosta *et al.*, “Measurement of the $t\bar{t}$ production cross section in $p\bar{p}$ collisions at $\sqrt{s} = 1.96$ TeV using lepton + jets events with secondary vertex b –tagging,” *Phys. Rev.* **D71** (2005) 052003, [hep-ex/0410041](#).
- [46] **CDF** Collaboration, F. Abe *et al.*, “The topology of three jet events in $p\bar{p}$ collisions at $\sqrt{s} = 1.8$ TeV,” *Phys. Rev.* **D45** (1992) 1448–1458.
- [47] A. Bhatti *et al.*, “Determination of the jet energy scale at the collider detector at fermilab,” *Nucl. Instrum. Meth.* **A566** (2006) 375–412, [hep-ex/0510047](#).
- [48] N. Lockyer *et al.*, “Measurement of the lifetime of bottom hadrons,” *Phys. Rev. Lett.* **51** (1983) 1316.
- [49] S. Budd *et al.*, “Measurement of the t - t bar production cross section in SECVTX-tagged lepton + jets events,” CDF/8037.

- [50] G. J. Feldman and R. D. Cousins, “A unified approach to the classical statistical analysis of small signals,” *Phys. Rev.* **D57** (1998) 3873–3889, [physics/9711021](#).
- [51] G. Corcella *et al.*, “HERWIG 6: An event generator for hadron emission reactions with interfering gluons (including supersymmetric processes),” *JHEP* **01** (2001) 010, [hep-ph/0011363](#).
- [52] M. L. Mangano, M. Moretti, F. Piccinini, R. Pittau, and A. D. Polosa, “ALPGEN: a generator for hard multiparton processes in hadronic collisions,” *JHEP* **07** (2003) 001, [hep-ph/0206293](#).
- [53] **CDF** Collaboration, A. Abulencia *et al.*, “Top quark mass measurement using the template method in the lepton + jets channel at CDF II,” *Phys. Rev.* **D73** (2006) 032003, [hep-ex/0510048](#).
- [54] G. Mahlon and S. J. Parke, “Maximizing spin correlations in top quark pair production at the tevatron,” *Phys. Lett.* **B411** (1997) 173–179, [hep-ph/9706304](#).
- [55] S. J. Parke and Y. Shadmi, “Spin correlations in top quark pair production at e^+e^- colliders,” *Phys. Lett.* **B387** (1996) 199–206, [hep-ph/9606419](#).
- [56] Delaere, C., “TMultiLayerPerceptron class of ROOT.”
<http://root.cern.ch/root/html310/TMultiLayerPerceptron.html>.
- [57] Brun, R. and others, “ROOT: An object-oriented data analysis framework.”
<http://root.cern.ch/>.
- [58] N. Goldschmidt, “A measurement of the helicity of W bosons at CDF,” [CDF/7915](#).
- [59] Y. Kim and U. Yang, “Initial state gluon radiation studies on Drell-Yan data for top-pair production in hadron colliders,” [CDF/6804](#).
- [60] T. Sjostrand *et al.*, “High energy physics event generation with PYTHIA 6.1,” *Comput. Phys. Commun.* **135** (2001) 238–259, [hep-ph/0010017](#).
- [61] S. Mrenna. Private Communication.
- [62] A. D. Martin, R. G. Roberts, W. J. Stirling, and R. S. Thorne, “Parton distributions and the lhc: W and z production,” *Eur. Phys. J.* **C14** (2000) 133–145, [hep-ph/9907231](#).
- [63] S. Frixione and B. R. Webber, “Matching nlo qcd computations and parton shower simulations,” *JHEP* **06** (2002) 029, [hep-ph/0204244](#).
- [64] S. Frixione, P. Nason, and B. R. Webber, “Matching NLO QCD and parton showers in heavy flavour production,” *JHEP* **08** (2003) 007, [hep-ph/0305252](#).
- [65] Schwindling, J. and Mansoulie, B., “MLPfit.”
<http://schwind.web.cern.ch/schwind/MLPfit.html>.
- [66] C. G. Broyden *Journal of the Institute of Mathematics and Its Applications* **6** (1970) 76–90.

- [67] R. Fletcher *Computer Journal* **13** (1970) 317.
- [68] D. Goldfarb *Mathematics of Computation* **24** (1970) 23.
- [69] D. F. Shanno *Mathematics of Computation* **24** (1970) 647.

Curriculum Vita

Jared Yamaoka

- 1993-1997** B.S. in Physics and Mathematics
Vassar College
Poughkeepsie, New York
- 1998-2000** Teaching Fellow
Harvard University
Boston, Massachusetts
- 2000-2001** Model Maker
Zung Studios
New York, New York
- 2001-2007** Ph.D. in Physics
Rutgers, the State University of New Jersey
New Brunswick, New Jersey
- 2001-2003** Teaching Assistant, Department of Physics & Astronomy
Rutgers, the State University of New Jersey
New Brunswick, New Jersey
- 2003-2007** Research Assistant, Department of Physics & Astronomy
Rutgers, the State University of New Jersey
New Brunswick, New Jersey